

1-1-1985

Structure-property studies in the deformation of semi-crystalline polymers/

Hoe H. Chuah

University of Massachusetts Amherst

Follow this and additional works at: https://scholarworks.umass.edu/dissertations_1

Recommended Citation

Chuah, Hoe H., "Structure-property studies in the deformation of semi-crystalline polymers/" (1985). *Doctoral Dissertations 1896 - February 2014*. 693.

https://scholarworks.umass.edu/dissertations_1/693

This Open Access Dissertation is brought to you for free and open access by ScholarWorks@UMass Amherst. It has been accepted for inclusion in Doctoral Dissertations 1896 - February 2014 by an authorized administrator of ScholarWorks@UMass Amherst. For more information, please contact scholarworks@library.umass.edu.



312066006987031

STRUCTURE-PROPERTY STUDIES IN THE
DEFORMATION OF SEMI-CRYSTALLINE POLYMERS

A Dissertation Presented

By

HOE HIN CHUAH

Submitted to the Graduate School of the
University of Massachusetts in partial fulfillment
of the requirements for the degree of

DOCTOR OF PHILOSOPHY

May 1985

Polymer Science and Engineering

Hoe Hin Chuah

©

All Rights Reserved

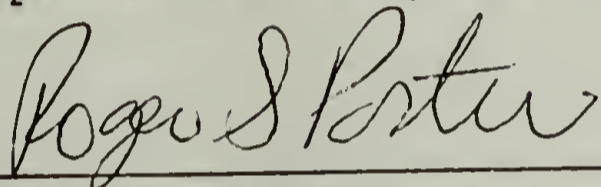
STRUCTURE-PROPERTY STUDIES IN THE
DEFORMATION OF SEMI-CRYSTALLINE POLYMERS

A Dissertation Presented

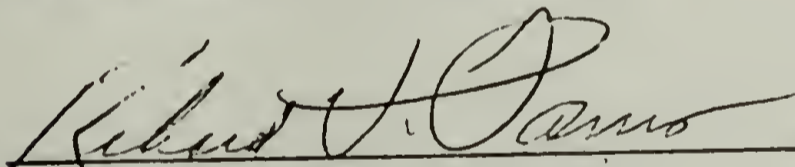
By

HOE HIN CHUAH

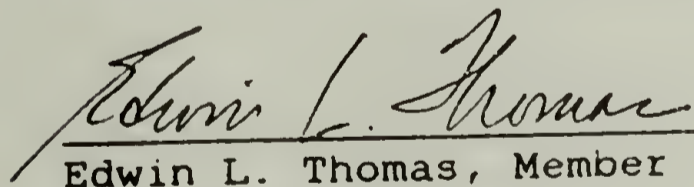
Approved as to style and content by:



Roger S. Porter
Chairperson of Committee



Richard J. Farris, Member



Edwin L. Thomas, Member



William J. MacKnight
Department Head
Polymer Science and
Engineering Department

To Soon Cheng, Joon Yee and Joon Hao:
For all the love and support you've given me.

TABLE OF CONTENTS

ACKNOWLEDGEMENT	viii
ABSTRACT	x
LIST OF TABLES	xii
LIST OF FIGURES	xiii

Chapter

I. DISSERTATION OVERVIEW	1
II. SOLID-STATE EXTRUSION OF CHAIN-EXTENDED POLYETHYLENE	5
2.1 Introduction	5
2.1.1 Chain-Extended Polyethylene	7
2.1.2 High Pressure Crystallization	9
2.1.3 Morphology	13
2.1.4 Mechanical Properties and Drawing	15
2.2 Experimental	16
2.2.1 Crystallization and Extrusion	16
2.2.2 Thermal Analysis and Density Measurements	19
2.2.3 Tensile Modulus	19
2.2.4 Thermal Shrinkage	20
2.2.5 Crystal Orientation	21
2.2.6 Lattice Distortion and Crystallite Size	23
2.2.7 Transmission Electron Microscopy	25
2.3 Results and Discussion	26
2.3.1 Morphology of Undrawn Billets	26
2.3.2 Thermal Analysis	37
2.3.3 Orientation and Molecular Draw Ratio	49
2.3.4 Correlation Between Modulus and Molecular Draw Ratio	52
2.3.5 Crystallite Size and Distortion	59
2.3.6 Deformation Mechanism	65
2.4 Conclusion	69

III. MELTING AND RECRYSTALLIZATION DURING DEFORMATION OF SEMI-CRYSTALLINE POLYMERS	71
3.1 Introduction	71
3.2 Experimental	75
3.3 Results	76
3.4 Discussion	94
3.5 Conclusion	98
IV. CRYSTAL STRUCTURES OF NYLON 6	99
4.1 Background	99
4.2 Mesomorphic Structure from Melt Spinning	103
4.3 γ -Structure from Iodine Treatment	106
4.4 Conclusion	108
V. SOLID-STATE CO-EXTRUSION OF NYLON 6 GEL	112
5.1 Background	112
5.2 Experimental	117
5.3 Results and Discussion	121
5.3.1 Nylon 6 Gelation	121
5.3.2 Characterization of Undrawn Gel Film	125
5.3.3 Properties of Drawn Gel Film	126
5.3.4 Deformation Mechanism	135
5.3.5 Annealing Behavior	156
5.4 Conclusion	161
VI. A NEW DRAWING TECHNIQUE FOR NYLON 6 BY REVERSIBLE PLASTICIZATION WITH IODINE	163
6.1 Introduction	163
6.2 Drawing with Plasticization	165
6.3 Experimental	167
6.4 Results and Discussion	169
6.4.1 Mechanism of $\alpha \rightarrow \gamma$ Crystal Transformation	169
6.4.2 Stoichiometry of Nylon 6-I Complex	172
6.4.3 Drawing and Mechanical Properties	184
6.4.4 X-Ray Diffraction Studies	193
6.4.5 Application to Other Nylons	205
6.5 Conclusion	207

VII. FUTURE WORK	208
REFERENCES	210

ACKNOWLEDGEMENT

I would like to thank my advisor, Professor Roger Porter, for his guidance in my research. His concern on the welfare of my family is beyond his duty as an academic advisor, yet a very important part of a student's life. He has been a great teacher and will always be my mentor.

Professor Richard Farris and Edwin Thomas also deserve special gratitude for their advice and discussions, and serving as committee members. I first met Professor Tetsuo Kanamoto of Tokyo Science University when he visited our laboratory in 1982. His interest in my work continued through the numerous communications. He has kindly served as a member of my dissertation committee. His friendship is deeply appreciated.

Professor John Wood of Chemistry Department kindly loaned the Weissenberg camera and helped in the interpretation of X-ray crystallographic work. Will McCarthy contributed his instrumental expertise in setting up the camera and through trial and error, made it work even without the long lost manual.

Dr. J.S. Lin of Oak Ridge National Laboratory assisted in the small-angle X-ray work on the question of a melting and recrystallization during deformation of a semi-crystalline polymers. His help and discussion led to our collaboration in this work.

Research activities in Professor Porter's group is

diverse and dynamic. Working and discussing with group members are indeed an eye-opening and stimulating experience. Eric George, Jim Jonza, Paul Lucas, Matt Muir, Jerry Palmer, Kevin Schell and Dr. Jean-Marc Lefebvre had critically read through my dissertation, made suggestions for improvement in both the dissertation and oral defense. I am grateful for their help and interest.

Colleagues from other research groups also contributed their skills in showing me how to use their instruments. De-Cai Yang kindly assisted in the electron microscopy work.

My wife, Soon Cheng, had painfully checked through typographical errors. Finally, I would like to thank the Malaysian-American Educational Exchange Commission and the Fulbright Commission for providing the fellowship.

ABSTRACT

Structure-Property Studies in the Deformation of Semi-Crystalline Polymers

(May 1985)

Hoe Hin Chuah, B. App. Sci. (First Class Honors),
Universiti Sains Malaysia.

M.S., Ph. D., University of Massachusetts.

Directed by: Professor Roger S. Porter

Drawing behavior of a high pressure crystallized chain-extended polyethylene in solid-state extrusion was studied. Because of the reduced trapped entanglements at the fold surfaces and interlamellar links in this morphology, there was insufficient continuity to provide stress transfer for effective orientation. Draw efficiency increases to a maximum of 0.71 when the polyethylene was crystallized at higher undercoolings. Tensile moduli were found to be a unique linear function of molecular draw ratio, measured by thermal shrinkage, independent of the initial morphology, draw temperatures and techniques. Electron microscopy of the fracture surface replicas at low draw showed the coexistence of undeformed, tilted, partially drawn lamellae and the generated fibrillar structure. The observations were consistent with Peterlin's model of plastic deformation.

The question of melting and recrystallization during

deformation was studied by small-angle X-ray scattering of the drawn chain-extended polyethylene. The results showed that melting and recrystallization did not occur for this morphology.

A partially dried Nylon 6 gel in benzyl alcohol was solid-state co-extruded at 150°C up to draw ratio 5.7. Double orientation was observed in this uniaxial drawing with the crystal chain axis oriented parallel and perpendicular to the draw direction. A deformation mechanism was proposed from the studies of birefringence, wide- and small-angle X-ray scatterings.

A new drawing technique for Nylon 6 by reversible plasticization with iodine was proposed. A complex was obtained by imbibing a Nylon 6 film in a KI_3 solution. It was drawn up to 790% elongation at 55°C and iodine was removed by titration with sodium thiosulfate to generate back a drawn Nylon 6 of controlled crystal form. The complex has a stoichiometry of $(Nylon\ 6)(I_3^-)_{0.24}(I_2)_{0.35}$. X-ray studies showed that interchain hydrogen bonds in both the crystal and amorphous regions were interrupted. The drawn complex has a new monoclinic crystal structure with iodine intercalated between the hydrogen bond sheets.

LIST OF TABLES

2.1. Crystallization Conditions and Characterization of Initial Billet Morphologies for the Chain-Extended Polyethylene	18
2.2. Change of Crystallite Sizes on Extrusion Drawing for a CEPE Billet Crystallized at 221°C	62
3.1. Long Period of CEPE and CFPE Billets Extruded at 100°C	79
4.1. Summary of Crystal Structures of Nylon 6 Reported in Literature	104
5.1. Change in Percent Crystallinity as Measured by DSC as a Function of Draw Ratio	134
5.2. Crystallite Sizes Along a-axis for (200) Equatorial and Meridional Reflections with Increasing Draw Ratio	146
5.3. Long Period From SAXS of Gel Film with Increasing Draw Ratio. X-Ray Beam is Normal to Film Plane	151
5.4. Change of Angle, ψ , between Long Axis of Fibrillar Crystals and the Draw Direction	151
6.1. Tensile Moduli of Nylon 6 Reported to-date Obtained by the Indicated Methods	164
6.2. Dimensional Changes in Nylon 6 film on Absorption in KI ₃ Solution	182
6.3. Weight Loss of Nylon 6-I Complex on Heating in a Thermal Gravimetric Analyzer	182
6.4. Properties of Drawn γ -Nylon 6 after Removal of Iodine using Sodium Thiosulfate Solution at Room Temperature.	192
6.5. Comparison of Observed and Calculated d-Spacings for a Nylon 6-I Complex Drawn 4X.	201
6.6. Crystal-Crystal Transformation of Other Aliphatic Nylons by Treatment with KI ₃ Solution.	206

LIST OF FIGURES

2.1.	Polyethylene pressure-temperature phase diagram constructed from melting points of a high pressure DTA, molecular weight 5×10^4 [49] . . .	22
2.2(a) to (d).	Histograms of lamellar thickness distribution of CEPE crystallized at 221, 216, 207 and 198°C respectively	28
2.3.	Transmission electron micrograph of fracture surface replicas of undrawn billets (a) T_c 221°C and (b) T_c 198°C.	33
2.4 to 2.7.	Melting endotherms of billets 1 to 4 and their extrudates in increasing draw ratio . . .	38
2.8.	Change of crystallinity as a function of extrusion draw ratio as measured by DSC for the four billets	46
2.9.	Change of crystal orientation function f on drawing for the three crystallographic axes a , b and c for drawn billets 1 ($T_c = 221^\circ\text{C}$) ($\blacktriangle, \bullet, \blacksquare$) and 4 ($T_c = 207^\circ\text{C}$) ($\triangle, \circ, \square$); f_c of billets 2 (∇) and 3 (\blacktriangledown) drawn to EDR 16.4 are inserted for comparison	47
2.10.	Molecular draw ratio (MDR) vs. extrusion draw ratio (EDR) showing the effect of initial morphology on efficiency of drawing (MDR/EDR) . . .	51
2.11.	Tensile moduli of CEPE at increasing extrusion draw ratio.	56
2.12.	Tensile moduli of CEPE as a function of molecular draw ratio. \blacksquare and \blacklozenge are chain-folded PE data from reference [61]	58
2.13.	Change of crystallite size D along the (110), (200) and (020) planes as a function of extrusion draw ratio for billet 1	63
2.14.	Change of distortion parameter, g_{II} , as a function of extrusion draw ratio for billet 1 . . .	64
2.15.	Transmission electron micrograph of fracture surface replica of billet 1 drawn 4.9X showing coexistence of undeformed, tilted, and partially drawn lamellae and generated fibrillar structure. Arrow indicates drawing	

direction	66
3.1. SAXS of undrawn CEPE crystallized at (a) 221°C and (b) 198°C	80
3.2. Meridional SAXS scans of CEPE billet 2 extruded at 100°C to draw ratios (a) 4.1 and (b) 16.4	83
3.3. SAXS scans of (a) undrawn chain-folded PE and (b) at draw ratio 12.2, extruded at 100°C	86
3.4. Long period of CEPE billet 2 extruded at increasing temperature to constant draw ratio of 12.9.	89
3.5. SAXS iso-intensity scattering patterns of CEPE billet 2 extruded to constant draw ratio of 12.9 at (a) 70, (b) 100 and (c) 125°C.	90
3.6. DSC scans of undrawn CEPE billet extruded at increasing draw temperature	92
4.1. Nylon 6 chains arranged in (a) parallel and (b) antiparallel. Arrow indicates hydrogen bond	101
4.2. Crystal structure of (a) α - and (b) γ -Nylon 6.	111
5.1. Schematics of the four states of aggregation for gel formation, (a) spherical particles linked linearly, (b) framework of rod-like particles, (c) micelles or crystallites of polymer and (d) crosslinked polymer network.	115
5.2. X-ray beam directions with respect to the coordinates of the gel film, normal (N), transverse (T) and parallel to the extrusion, also called the machine (M) direction.	120
5.3. DSC scan of a 5 wt% Nylon 6 gel.	124
5.4. DSC scans of undrawn and drawn Nylon 6 gel films	128
5.5. WAXD and SAXS photographs of undrawn, dried gel with X-ray beam (a) normal and (b) parallel to film plane.	130
5.6. Tensile modulus as a function of draw ratio for solvent-cast Nylon 6 film; Nylon 6 gel film before and after annealing at 190°C	132

5.7.	Birefringence as a function of draw ratio for Nylon 6 gel and solvent-cast Nylon 6 films . . .	133
5.8.	Pole figure of (200) reflection of Nylon 6 gel drawn 3.7X.	138
5.9.	WAXD photographs of Nylon 6 gel film with increasing draw ratio, X-ray beam normal to film plane.	139
5.10(a).	Reciprocal lattice of Nylon 6 fibrillar α -crystal at low draw <1.9X, showing the relative position of the (200), (002) and (202) reflections as would be observed in WAXD.	144
5.10(b).	Reciprocal lattice of Nylon 6 fibrillar α -crystal at high draw >3.7X, showing the relative position of the (200), (002) and (202) reflections as would be observed in WAXD.	145
5.11.	SAXS photographs of gel film with increasing draw ratio, X-ray beam normal to film plane. .	152
5.12.	Schematic representation of orientation of the fibrillar crystals during deformation.	
	(a) Undrawn state with random interlacement of fibrillar crystals.	
	(b) At low draw ratio <1.9X, long axis (a-axis) of the fibrillar crystals weakly oriented towards draw direction.	
	(c) At high draw ratio >3.7X, long axis of the fibrillar crystals oriented in draw direction.	
	(d) Enlargement of the aggregates of fibrillar crystals showing the long period	154
5.13.	Birefringence as a function of tilt angle α for unannealed and annealed drawn gel. Draw ratio (a)2.1, (b)2.9 and (c)3.7.	157
6.1.	UV-visible spectra of a Nylon 6-I complex film partially washed with water	175
6.2.	% Weight gain of Nylon 6 after immersion in I_2 aqueous solution as a function of time . .	176
6.3.	Thermal gravimetric analysis of Nylon 6-I complex with increasing amount of absorbed chemical species after immersion in	

	KI ₃ solution, (a) 28.7, (b) 51.8, (c) 57.5 and (d) 62.6%	177
6.4.	UV-visible spectra of trapped evolved gas in CCl ₄ on pyrolysis of Nylon 6-I complex at 250°C	183
6.5.	Stress-strain curve of a wet Nylon 6-I complex film, tested immediately after immersing in a 1N aqueous KI ₃ solution for 48 hours	187
6.6.	Loss factor tan δ for undrawn Nylon 6-I complexes at frequencies 11,35 and 110 Hz.	188
6.7.	DSC scans on heating and cooling the Nylon 6-I complex at 20°C/min.	189
6.8.	Arrhenius plot of Log f (frequency) vs. 1/T for undrawn Nylon 6-I complex	190
6.9.	Stress-strain curves for γ-Nylon 6 (solid lines) and Nylon 6-I complex (broken lines) at temperatures below and above the α-relaxation of the complex	191
6.10.	WAXD scans of an undrawn Nylon 6-I complex and at increasing draw ratio at room temperature	194
6.11.	(a) Rotation photograph of a Nylon 6-I complex drawn 4X and (b) schematic showing details of observed reflections	199
6.12.	Space filling model of one quarter of the proposed structure for Nylon 6-I complex in the a-c plane, showing iodine intercalated between Nylon 6 chains	202

C H A P T E R I

DISSERTATION OVERVIEW

This dissertation studies the drawing of two highly important and among the most studied commercial polymers: high density polyethylene and Nylon 6. From the view of chain conformation, both polymers are similar in the spatial arrangement of their molecular chains. The polyethylene (PE) chain is made up of long sequences of methylene units and Nylon 6 chain has sequences of five methylene units alternated with amide groups, they are also arranged in fully extended ziz-zag conformation. Due to the inherently strong C-C bond and their extended conformations, both polymers have high theoretical moduli, 300 GPa for PE [1] and 264 GPa for Nylon 6 [2].

Over the last decade, there have been rapid advances in drawing PE into ultra-high modulus fibers. A remarkable 222 GPa modulus has been reported [3], which is undoubtedly an achievement of scientific interest. It was disclosed, though not yet commercialized, adaptation of the gel drawing process [4] by industry had produced PE fibers with modulus higher than that of either steel or rigid-rod Kevlar fibers when the moduli are compared on

per unit volume basis [5]. The development in ultradrawing had transformed PE from a mere 1 GPa modulus material into one with modulus approaching its theoretical limit. The improvement in Nylon 6 drawing is, however, far behind. Although Nylon 6 has been in existence for over 50 years, the highest tensile modulus previously reported is only 14 GPa [6].

PE has a rather low melting point of 142°C whereas Nylon 6 has an equilibrium melting point of as high as 275°C [7] due to its ability to form interchain hydrogen bonds between the amide groups. Therefore, if Nylon 6 could be ultradrawn it has the potential for a much wider temperature range applications. The presence of hydrogen bonds, although responsible for the higher melting point, also hinders Nylon 6 drawability. Thus ultra-drawing of Nylon 6 remains a difficult challenge. To develop new ways of drawing and perfecting the morphology of Nylon 6 form part of the research program of this dissertation.

Solid-state extrusion is a technique used to ultradraw polymers. It is similar to the extrusion used in metal forming process [8]. However, it was the original study of stress-induced crystallization of PE in an Instron rheometer by Southern and Porter [9] that showed its potential as a route to achieve high orientation and ultra-high modulus polymers. This technique has been extensively studied and further

developed in this laboratory to draw a wide variety of semi-crystalline and amorphous polymers [10]. This dissertation uses this as a principal technique to draw PE and Nylon 6.

Chapter 2 studies the less explored drawing of a chain-extended PE and with well characterized initial morphology. Properties of the extrudates are characterized to elucidate the effect of initial morphology on drawing. Molecular draw ratio, measured by thermal shrinkage, shows unique linear relationship with tensile modulus and is proposed as a parameter to be used when comparing moduli of drawn PE by the different drawing methods. Deformation zone of these extremely thick lamellae in the fracture surface replicas is examined by electron microscopy to study the deformation mechanism. The controversial issue of partial melting and recrystallization during deformation of semi-crystalline polymers is reexamined in Chapter 3. A small-angle X-ray scattering study of the chain-extended PE drawn, both as a function of draw ratio at constant temperature and of different temperature at constant draw ratio, provide new insight for this problem.

Chapter 4 reviews the crystal structures of Nylon 6. Over a dozen structures have been previously reported and the issue is confusing. This chapter compares the crystallographic data and comments on validity.

Perspective is thus provided for the understanding of structural changes in Nylon 6 drawing in the next two chapters.

In Chapter 5, a Nylon 6 gel film, which has a mixture of fibrillar and lamellar crystal morphologies, is studied by solid-state co-extrusion. A deformation mechanism is proposed for the development of the observed double orientation using a combination of experimental methods: wide- and small-angle X-ray scatterings, and birefringence.

A new drawing technique for Nylon 6 is described in Chapter 6. The objective is to disrupt the interchain hydrogen bonds to achieve ultradrawing by using iodine as a reversible plasticizer. Properties of the intermediate Nylon 6-I complex have been studied by spectroscopy, thermal analysis and mechanical methods. From X-ray study, a structure of the complex is proposed. This chapter also discusses the role of iodine and the triiodide ion in the $\alpha \rightarrow \gamma$ crystal transformation. The potential application of this new drawing technique to others in the series of aliphatic Nylons is also discussed.

Chapter 7 suggests possible future research based on the studies described above.

C H A P T E R I I

SOLID-STATE EXTRUSION OF CHAIN-EXTENDED POLYETHYLENE

2.1 Introduction

The drawing of PE is a subject of continuing interest. Over the last decade, rapid advances in orienting flexible chain polymers to achieve high modulus and high strength have resulted in the development of several new drawing techniques. Broadly, these can be classified into drawing from solid polymers and from polymer solutions or melts. Tensile drawing of solid polymers to improve the mechanical properties had a long history [11], but the strength and modulus obtained had never reached those achieved by the newer techniques such as the solid-state extrusion, with or without the use of pressure transmitting fluid [10, 12-14], solid-state co-extrusion [15], zone drawing and annealing [16] and multi-stage drawing of PE single crystal mat [17]. Important developments in drawing from polymer solutions and melts stem from fibrillar crystal growing and hot drawing [18], gel fiber drawing [19-21], melt drawing and

crystallization under elongational flow [22, 23].

Each of these new techniques draws PE into fibers or films with vastly improved tensile modulus and strength. The highest modulus reported to date is 222 GPa from the drawing of PE single crystal mat [3]. This newly reported modulus, with crystallinity only 85%, prompted reconsideration of the usually accepted 300 GPa theoretical modulus to a more probable value of 400 GPa [24].

The reasons that PE has high theoretical modulus are due to the intrinsic strength of the covalent C-C bonds since the methylene chains are arranged in extended planar zig-zag conformation. Drawing to achieve high modulus requires efficient alignment of the chains and to crystallize them into extended conformation in the draw direction from their random state in the solution or melt. In the case of drawing of solid semi-crystalline polymers, the folded chains of the lamellae are unravelled and the random chains in the amorphous region are stretched. These extended chains can form crystalline bridges giving crystal continuity, or become the taut tie molecules as proposed in the structural models of oriented PE [25, 26].

Most of the orientation studies were done on chain-folded high density PE with starting lamellar thickness of <100 nm and with molecular weight ranging from 10^4 to 10^7 . There have been few reports on the

drawing of PE with chain-extended morphology. One may ask is chain-extended PE (CEPE) a better starting morphology to generate the extended chains of the oriented microfibrils, or can it be more efficiently drawn than the chain-folded PE? There are two reasons why there are so few studies on the drawing of CEPE. First, this morphology can only be obtained from high pressure crystallization which requires special facility. Second, CEPE is brittle, tensile drawing in free space fails at low draw, $<6X$ [27]. However, the solid-state extrusion technique developed in this laboratory had effectively drawn brittle polymers such as polystyrene and compacted PE powder [28, 29] which do not draw well by other methods. With the compression from the plunger and the lateral constraints imposed on the CEPE billet by the capillary wall during extrusion, a high draw ratio of 23 was obtained at $100^{\circ}C$ without fracture. This chapter studies CEPE drawing behavior and the properties of the extrudates.

2.1.1 Chain-Extended Polyethylene

When a polymer melt is crystallized, the random chains can crystallize into either chain-folded or extended chain conformation depending on the crystallization condition. Chain folding during crystallization is kinetically controlled in such a way

that the lamellar crystal formed is one that maximizes the crystallization rate and not necessarily of the lowest free energy state [30]. However, chain-extended lamellae, with the size of the crystal in the chain direction essentially equal to the extended chain length, approach the equilibrium morphology of PE and reportedly for other semi-crystalline polymers as well [31].

It was reported as early as 1958, when melts of polytetrafluoroethylene [32] and selenium [33] are crystallized at very slow rate, chain-extended lamellae of several μm thick are obtained. However, slow crystallization of PE melt at 130°C for 20 to 40 days produced lamellae with enhanced thickness but only of the order of 100 nm [34]. Only when a PE melt was crystallized under pressure of $>3\text{kbar}$, could chain-extended PE of several μm thickness be obtained [35, 36]. High pressure is necessary to crystallize PE melt into this morphology. Subsequent studies of other polymers, such as polychlorotrifluoroethylene [37] and Nylon 6 [38] also reportedly gave chain-extended lamellae.

A term "anarbaric (meaning up-pressure) crystallization" was coined by Bassett [39] to describe the distinct phenomenon associated with crystallization of PE at high pressure. It was suggested that this term differentiates from chain-extended morphology obtained by other processes: from slow crystallization at atmospheric

pressure [32], from simultaneous polymerization-crystallization [40] and from the extended chains of the core of a shish-kebab [41] produced by flow-induced crystallization.

2.1.2 High Pressure Crystallization

Since the first report of thick CEPE, the high pressure crystallization and structure-property relationship of this morphology have been extensively studied mainly by the research groups of Wunderlich [42], Bassett [43], Kanetsuna [44] and Takemura [45]. Over the years, several excellent reviews [42, 43, 46] have appeared. It is not the intention of this section to review this morphology but to highlight the points essential for the understanding of CEPE drawing behavior.

When PE is melt crystallized at pressure greater than 350 MPa and at high temperature, chain-extended lamellae are obtained [47]. High temperature crystallization is a result of the increase in melting point with increasing pressure. The volume and enthalpy changes obey the Clausius-Clapeyron equation [35] and the melting point increases at about $20^{\circ}\text{C}/100\text{ MPa}$. An empirical equation for the effect of pressure on melting point, T_m , was given by Wunderlich [42] from the fitting of melting point data in high pressure crystallization of PE:

$$T_m = 415.7 + 28.1P - 1.66P^2 \quad (2.1)$$

where P is pressure in kbar and T_m in K.

T_m given by this equation agrees reasonably well with that predicted by the Clausius-Clapeyron equation only in the range of 3.5 to 5 kbar.

Depending on the crystallization conditions, crystal thickness can vary from a few hundred nm to few μm . Generally, some chain folding is still observed in the chain-extended lamellae with the exception of low molecular weight PE which can be crystallized into fully extended chains. A definition for chain-extended lamellae has been proposed as those having thickness of more than 200 nm [47]. This thickness corresponds to a PE molecular weight of $\sim 20,000$ and to conditions where crystal surfaces and chain ends become negligible in affecting the melting behavior. The melting point is depressed by $< 1^\circ\text{C}$. Crystallization at an intermediate pressure range of 200 - 300 MPa gives a mixture of chain-extended and chain-folded morphologies while at pressure < 200 MPa, only chain-folded lamellae are obtained [48].

Although high pressure crystallization of PE has been studied extensively for many years, the crystallization mechanism is still uncertain. Several explanations (reviewed by Bassett [46]) put forward had been rejected. Now it is accepted that crystallization of PE to chain-extended lamellae involves going through a high

pressure hexagonal phase [49]. The presence of this phase was first observed as an endotherm in high pressure differential thermal analysis (DTA) by three research groups [49-51]. It was Bassett and Turner [52] who correctly identified it as a hexagonal phase by analogy of the rotator phase (a hexagonal phase) of n-paraffins. The presence of this phase was later confirmed from X-ray diffraction [53]. A phase diagram (Fig. 2.1) constructed from the observed melting points in high pressure DTA, shows the temperature-pressure range in which hexagonal phase exists, and is used as a guide in selecting the crystallization conditions in the present work.

From the phase diagram, crystallization at a combination of pressure and temperature above the triple point where the hexagonal phase exists will give chain-extended lamellae, conversely, outside this phase will give chain-folded lamellae. However, in practice it was found that the hexagonal phase can occur in a metastable state together with the orthorhombic phase at temperatures below the triple point. Therefore a mixture of chain-extended as well as chain-folded lamellae can form when the melt is crystallized at undercooling below the triple point which has been shown to vary as much as 18°C [39]. Furthermore, it also depends on molecular weight and its distribution.

The crystallization conditions used in this work

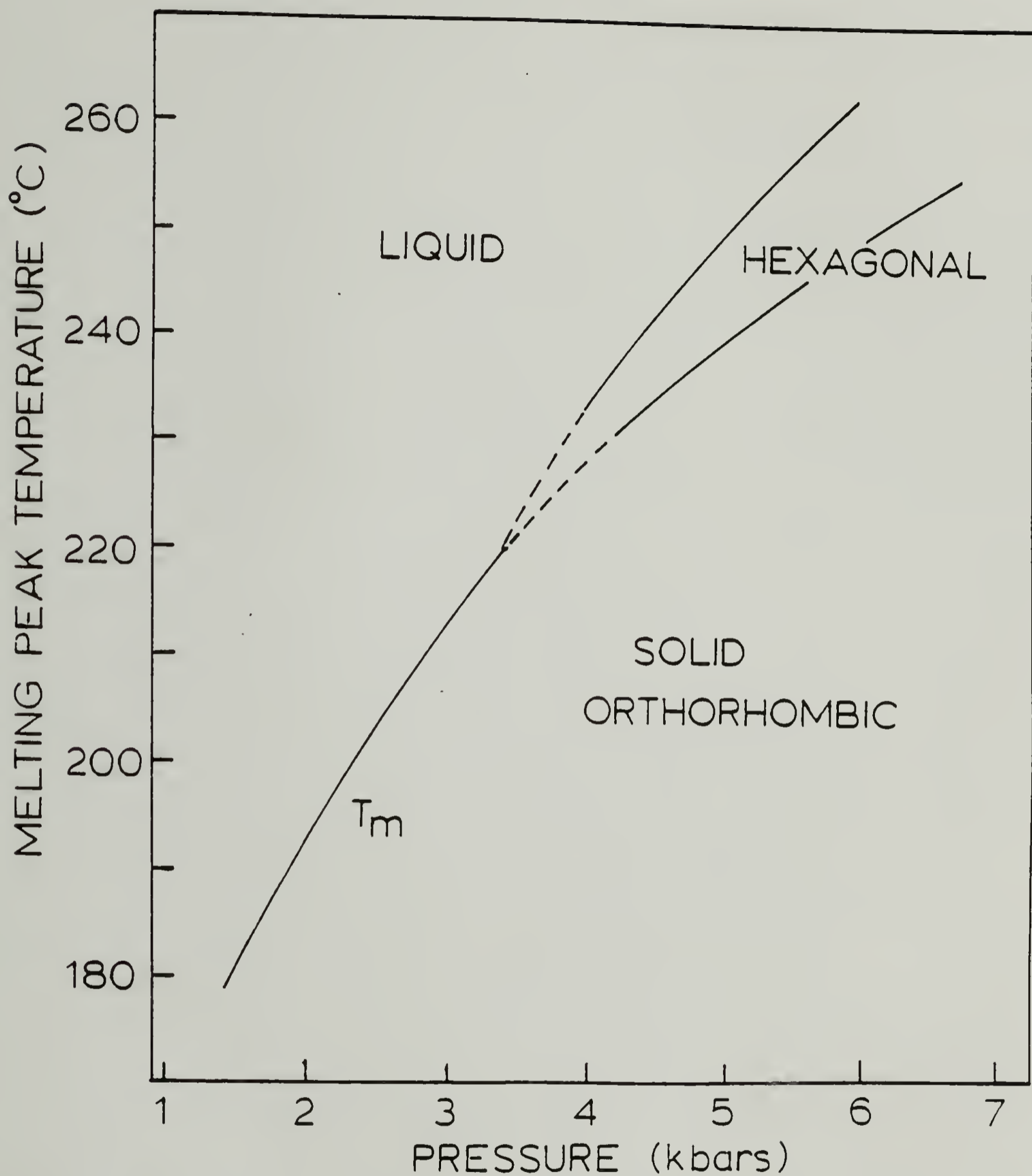


Figure 2.1. Polyethylene pressure-temperature phase diagram constructed from melting points of a high pressure DTA, molecular weight 5×10^4 [49].

maintain a constant pressure while the temperature is varied so that crystallization fell within the hexagonal phase regime and below the triple point to give initial morphology with varying lamellar thickness distribution.

2.1.3 Morphology

CEPE is highly crystalline with crystallinity usually above 0.9, and can approach 1.0 when crystallized at very low undercooling and for a long period of time. Thermal behavior by differential scanning calorimetry (DSC) shows several melting endotherms when samples are heated slowly. The highest endotherm with peak melting point $\sim 141^{\circ}\text{C}$ is predominant in peak area ($\sim 90\%$ of total area) and constitutes the main bulk of the chain-extended lamellae. The lower melting endotherms occurring between 125 to 130°C are from low molecular weight PE which was rejected during crystallization and was able to crystallize into either chain-folded [54] or chain-extended lamellae during the cooling process [55]. The presence of this low molecular weight fraction has a profound effect on its mechanical properties and drawability and will be discussed in Section 2.1.4.

The thickness of the chain-extended lamellae increases with increasing molecular weight, crystallization time and most markedly with crystallization temperature. The distribution of the

lamellar sizes are usually much broader than those obtained in either solution grown single crystals or in melt-crystallized chain-folded crystals [42]. By comparing the lamellar thickness distribution and its molecular chain length, it was shown that the chains are still folded except for the low molecular weight fraction where the chains can be fully extended [56]. Although lamellar thickness increases with molecular weight, the crystallinity decreases because of increasing entanglement of the chains in the melt during crystallization.

High pressure crystallization can also give spherulites however, the large extended platelike crystal is not ideally suited for a perfect spherulite development [42]. The lamellae splay apart from the center of the spherulite or from some branch points with the spherulite center usually not well developed. Because of the large lamellar size and their brittle nature, their morphology can be easily studied in detail from its fracture surface by electron microscopy of replicas which shows the typically thick lamellae with striations perpendicular or inclined at an angle to the lamellar surface. These striations run parallel to the molecular chain direction and are surface effect.

The fracture surfaces revealed are the most easily cleaved (hk0) planes parallel to the molecular chains. For low molecular weight PE crystallized with high chain

extension and with minimum number of folds, the fracture surface is usually clean. With increasing molecular weight, and consequently increased entanglements, chains are pulled out in the form of fibrous bundles giving a fracture surface overlaid with fibers.

2.1.4 Mechanical Properties and Drawing

CEPE is brittle due to the segregation of low molecular weight fractions, $<10^4$, during crystallization. These populations usually have chains highly extended with no more than three folds per molecule [39] and are inherently brittle. They are embedded in the bulk giving flaws [43] in which fracture can easily occur and propagate. Drawing then becomes difficult due to the brittleness. However, if these are removed by fractionation, the ductility of CEPE is improved and reportedly draws to $<6X$ at 80°C [27].

There are few drawing studies of CEPE. Mead and Porter [57] had crystallized high density PE at 490 MPa and at temperatures between 134 and 220°C . The resulting billets were solid-state extruded at 120°C to a high draw ratio of 30. Although the initial morphology was not fully examined, DSC showed that some of the billets gave high melting points, presumably due to chain-extended crystals. Lupton and Register [58] solid-state extruded ultra-high molecular weight ($\sim 2 \times 10^6$) CEPE into a mold.

The article obtained was rigid and tough.

This chapter reports in detail the drawing behavior by solid-state extrusion of CEPE, with well-characterized initial morphologies. The effect of the initial morphology on drawing, properties of extrudates and the deformation mechanism are studied.

2.2 Experimental

2.2.1 Crystallization and Extrusion

An Instron capillary rheometer, model 3210 MCR, with 3/8 inch diameter barrel was used as a temperature-pressure vessel by blocking the exit for crystallization. High density PE pellets with narrow molecular weight distribution (Du Pont Alathon 7050, M_w 59,000 and M_n 19,000) were compacted in the rheometer under cyclic loading of 200 MPa at 120°C for 30 min. to minimise voids trapped between the pellets. 10g of the pellets were used giving the final billet about 14 cm long. With this length, variation of crystallization temperature, T_c , along the rheometer barrel is $\pm 1^\circ\text{C}$. The pellets were melted and brought to the desired T_c after releasing the pressure. Crystallization was initiated by raising the pressure from atmospheric to 460 MPa in about 80s. The increase of pressure caused compressive heating,

raising the temperature of the system initially by 2°C. No correction was made as T_c was rapidly reestablished. Crystallization conditions were maintained for 3 hours followed by cooling with an air jet while the pressure was held constant. Initial cooling rate was $\sim 4^\circ\text{C}/\text{min}$. At the constant pressure of 460 MPa, the four T_c chosen were 221, 216, 207 and 198°C , corresponding to a range of undercooling to give billets of different densities and crystallinities (Table 2.1)

The resultant CEPE billets, with one end shaved into conical shape to fit the extrusion die, were solid-state extruded at $100 \pm 1^\circ\text{C}$ in the rheometer using a conical brass die with an entrance angle of 20° at a constant plunger speed of 0.05 cm/min. A 200g weight was attached to the end of the extrudate to keep it straight. Details of this extrusion technique have been described elsewhere [59]. The initial 20 cm of the extrudates obtained before reaching steady-state extrusion was discarded to avoid imperfection and variation of physical properties. The extrusion draw ratio, EDR, was measured from the reduction of cross-sectional area before and after extrusion.

$$\text{EDR} = (R_o/R_i)^2 \quad (2.2)$$

where R_o = radius of undrawn billet

R_i = radius of extrudate

Table 2.1
 Crystallization Conditions and Characterization of Initial
 Billet Morphologies for the Chain-Extended Polyethylene

Billet	Temperature (°C)	Pressure (MPa)	Density (kg/m ³)	ΔH_f (Cal/g)	Crystallinity from Density	Lamellar Thickness Distribution	
						\bar{L}_n (nm)	\bar{L}_w (nm)
1	221	460	990	68.5	0.94	480	570
2	216	460	989	67.5	0.93	350	500
3	207	460	982	63.3	0.89	270	330
4	198	460	981	61.3	0.89	280	320

2.2.2 Thermal Analysis and Density Measurements

The melting behavior was studied using a Perkin-Elmer DSC-II differential scanning calorimeter at a heating rate of 2.5°C/min. Low heating rate was used to avoid superheating. A constant sample weight of ~4 mg was used throughout. Indium and tin were used for calibration.

Densities were measured in a 1 liter density gradient column using a mixture of ethanol and 1% glycerol solution in water at 23°C. Graduation of the column was in 10 ml giving the density accuracy of $\pm 0.0002 \text{ kg/m}^3$.

2.2.3 Tensile Modulus

Tensile modulus, E , was measured at room temperature using an Instron tensile tester (model TTM). Due to the brittleness of the drawn CEPE, the pressure applied at the grips in tensile pulling led to fracture. A three-point bending test was thus used instead at strain rate $\sim 1.5 \times 10^{-3} \text{ min}^{-1}$. At small strain, the modulus thus obtained is equivalent to that by tensile pulling. As the samples were highly anisotropic, to avoid the end effects of localized stresses at loading points, samples with aspect ratio > 100 were used [60]. The modulus is given as:

$$E = \frac{4 L^3 P}{3 \pi d^4 y} \quad (2.3)$$

where d = diameter of extrudate

L = length of sample between end points

P = load

y = displacement of extrudate center

2.2.4 Thermal Shrinkage

Molecular draw ratio (MDR) was measured by thermal shrinkage experiment [61], conducted by shaving the extrudates to a thickness <0.5mm and 1 cm long, followed by immersion in a silicone oil bath at 180°C for 2 min. Silicone oil instead of glycerol was used because the latter was found to swell the samples [62]. Two min. immersion time was chosen from trial in which shrinkage due to elastic recovery reached a plateau without the sample ends changing in shape. On prolong immersion, further shrinkage can continue to a point where the sample become circular due to the thermodynamic forces converting the melt to an equilibrium shape of lowest surface energy [63]. The length before and after shrinkage were measured using a travelling microscope to $\pm 0.005\text{mm}$.

MDR is defined as:

$$\text{MDR} = \frac{\Delta L}{L_0} + 1 \quad (2.4)$$

where ΔL = change in length before and after shrinkage,

L_0 = original length before extrusion.

2.2.5 Crystal Orientation

A Siemens D-500 X-ray diffractometer equipped with a scintillation counter, operating at 27 mA and 45 kV using a Ni-filtered Cu K_α radiation was used to measure the crystal orientation.

For uniaxial drawing, crystal orientation of the unit cell axes with respect to the draw direction can be expressed by the Hermann-Stein orientation function :

$$f_i = \frac{3\langle \cos^2 \phi \rangle_i - 1}{2} \quad (2.5)$$

where ϕ is the angle between the diffraction plane normal and the uniaxially drawn axis, $i = a, b,$ and c are the crystallographic axes of the PE orthorhombic unit cell. Although the orientation function is a convenient index to characterize orientation, it must be noted that f_i is an average value giving the second moment of the orientation distribution of the $a, b,$ and c axes and therefore is not unique. Different orientation distribution can exist giving the same value of $\langle \cos^2 \phi \rangle_i$ and f_i [64].

For a perfect orientation, f_i is 1, 0 for random and -0.5 for perpendicular orientation. Experimental determination involves the measurement of $\langle \cos^2 \phi \rangle$ from the azimuthal scanning of the diffracted intensity $I(\phi)$ of the extrudate,

$$\langle \cos^2 \phi \rangle_i = \frac{\int_0^{\pi/2} I(\phi) \cos^2 \phi \sin \phi \, d\phi}{\int_0^{\pi/2} I(\phi) \sin \phi \, d\phi} \quad (2.6)$$

Direct measurements of $\langle \cos^2 \phi \rangle$ can only be made if there are strong diffraction intensities from (h00), (0k0) and (00l) planes respectively. However, for PE, intensity of (002) diffraction is usually too weak for accurate measurement except in highly oriented samples. An indirect method developed by Wilchinsky [65] involving the azimuthal scanning of (110) and (200) diffractions was used, in which

$$\langle \cos^2 \phi \rangle_a = \langle \cos^2 \phi \rangle_{200} \quad (2.7)$$

$$\langle \cos^2 \phi \rangle_b = 1.445 \langle \cos^2 \phi \rangle_{110} - 0.445 \langle \cos^2 \phi \rangle_{200} \quad (2.8)$$

From the orthogonal relationship, $\langle \cos^2 \phi \rangle_c$ is given by

$$\langle \cos^2 \phi \rangle_a + \langle \cos^2 \phi \rangle_b + \langle \cos^2 \phi \rangle_c = 1 \quad (2.9)$$

Desper et al. [66] had shown that f_c determined by Wilchinsky's method agreed very well with the direct measurement of (002) diffraction for solid-state extruded PE of high draw ratio.

A 0.5 mm to 1 mm thick sample was scanned from azimuthal angle $\phi = 0$ to 90° at a scan rate of $0.5^\circ 2\theta$ /min in a normal beam transmission mode at a fixed 2θ

angles of 21.5° and 24.0° of the (110) and (200) diffractions respectively. The intensity was corrected for background and absorption, $\langle \cos^2 \phi \rangle$ was evaluated from equation 2.6.

2.2.6 Lattice Distortion and Crystallite Size

For a large, perfect crystal, the X-ray diffraction intensity is a sharp spike. With increasing lattice distortion, and/or smaller crystallite size, the diffraction profile broadens. Therefore, diffraction broadening can be a measure of the crystal lattice distortion and crystallite size.

Scherrer's equation [67] is often used to determine the mean crystallite size by assuming the polymer crystals are relatively perfect and broadening is therefore due to size alone:

$$D_{hkl} = \frac{K\lambda}{\beta \cos\theta} \quad (2.10)$$

\bar{D}_{hkl} is the mean dimension of the crystallites perpendicular to the (hkl) planes, β is the integral breadth or breadth at half-maximum intensity in radians, K is a constant having a value of 0.9 to 1.

Hosemann [68] introduced a distortion parameter g_{II} which measures the relative variation between neighboring (hkl) planes,

$$g_{II} = \frac{(\Delta^2 d_{hkl})^{0.5}}{d_{hkl}} \quad (2.11)$$

where d_{hkl} is the interplanar distance.

When lattice distortion cannot be neglected, then the overall diffraction broadening, $(\delta s)_o$ is made up of broadening due to crystal size, $(\delta s)_c$, and distortion, $(\delta s)_{II}$ which incorporates the distortion parameter.

$$\begin{aligned} (\delta s)_o^2 &= (\delta s)_c^2 + (\delta s)_{II}^2 \\ &= 1/\bar{D}_{hkl}^2 + (\pi g_{II})^4 m^4 / d_{hkl}^2 \end{aligned} \quad (2.12)$$

where m is the order of reflection.

This equation permits the separation of the crystallite size from lattice distortion effect if there are at least two well-resolved orders of reflection for the (hkl) planes. Plotting of $(\delta s)_o^2$ against m^4 gives a straight line with intercept, $1/\bar{D}_{hkl}^2$, and slope, $(\pi g_{II})^4 / d_{hkl}^2$. Therefore, \bar{D}_{hkl} and g_{II} can be determined separately.

In the experimental measurement of diffraction broadening, the Siemens D-500 diffractometer was carefully aligned with high precision and with very fine collimation of the X-ray beam to minimise instrumental broadening. The anti-scatterer slits were 0.3 and 0.1° , the divergence and the receiving slits of the diffracted beam were 0.1 and 0.018° respectively. Hexamethylene tetramine crystals were used as standard to determine the

instrumental broadening, found to be 0.08° .

The samples were arranged in a normal beam transmission mode and step scanned at 0.02° 2θ interval. Scan time was set such that the total counts at maxima was $\sim 20,000$ and then normalized to improve signal to noise ratio. The diffraction profile was corrected for K_α doublet using Rachinger's method [69] to give breadth at half maximum intensity, β . By assuming the broadening profile to be Gaussian in shape [70], correction of the experimental profile, B , from instrumental broadening, b , can be approximated as:

$$\beta^2 = B^2 - b^2 \quad (2.13)$$

however, if Cauchy profiles are assumed [71]:

$$\beta = B - b \quad (2.14)$$

It had been shown that Gaussian approximation agrees in general with the more elaborate deconvolution method used by Stoke [71]] to within 10%.

For (110) reflection, there is a second order (220) reflection strong enough to be recorded to allow separate determination of lattice distortion, g_{II} and crystallite size according to equation 2.12.

2.2.7 Transmission Electron Microscopy

A JOEL 100kV transmission electron microscope was used to examine the fracture surfaces. The undrawn billets and the extrudates were fractured in the center along the axial direction under liquid N_2 . Replicas were made for microscope examination using a method of Geil [71], modified by Minter [72]. The fracture surfaces were shadowed with C-Pt at 30° and coated with C at 90° angles. The replicas were stripped with polyacrylic acid which was subsequently dissolved in water to release them for examination. Four replicas were made for each undrawn billet and micrographs were taken at random positions to measure the lamellae thickness distribution. A statistical method of Rees and Bassett [54] was used to compute the number average thickness.

2.3 Results and Discussion

2.3.1 Morphology of Undrawn Billets

Table 2.1 lists the crystallization conditions and the characterization of the four initial billets. They are listed in order of decreasing T_c , 221, 216, 207 and 198°C . Crystallinity, measured from density, is high. 0.94 when T_c is 221°C and decreases to 0.89 with decreasing T_c . The heat of fusion data, however, gave consistently higher crystallinities.

The examination of fracture surfaces with the

electron microscope had a dual purpose. It revealed the characteristic feature of the chain-extended morphology by exposing the fractured (hk0) surfaces, showing the striated, long strips of thick lamellae. Thus this confirmed that the lamellae of the initial billets were indeed chain-extended. From the large number of micrographs taken, quantitative measurements of the lamellar thickness distribution were made.

Fig. 2.2(a) to (d) shows the histograms of the lamellar thickness distribution of the four billets. The distribution is skewed towards lower lamellar thickness with maxima occurring ~ 200 nm. The fraction gradually decreases with increasing thickness up to 1,400 nm for billets 1 and 2. However, for billets 3 and 4, there are no lamellar fractions with thicknesses >800 nm. The number average thickness, \bar{L}_n , computed from the histograms are shown in the last column of Table 2.1. Billet 1 has the highest \bar{L}_n of 480 nm, and \bar{L}_n decreases to 280 nm for billet 4.

The use of micrographs of fracture surfaces to compute lamellar thickness presents some problems. Not only is it laborious, but good statistical sampling is also necessary. The fracture surfaces also inherently expose mainly the (hk0) planes containing the chain axis which could be tilted or inclined at an angle to the lamellar surface. For more accurate measurements,

Figure 2.2(a) to (d). Histograms of lamellar thickness distribution of CEPE crystallized at 221, 216, 207 and 198°C respectively.

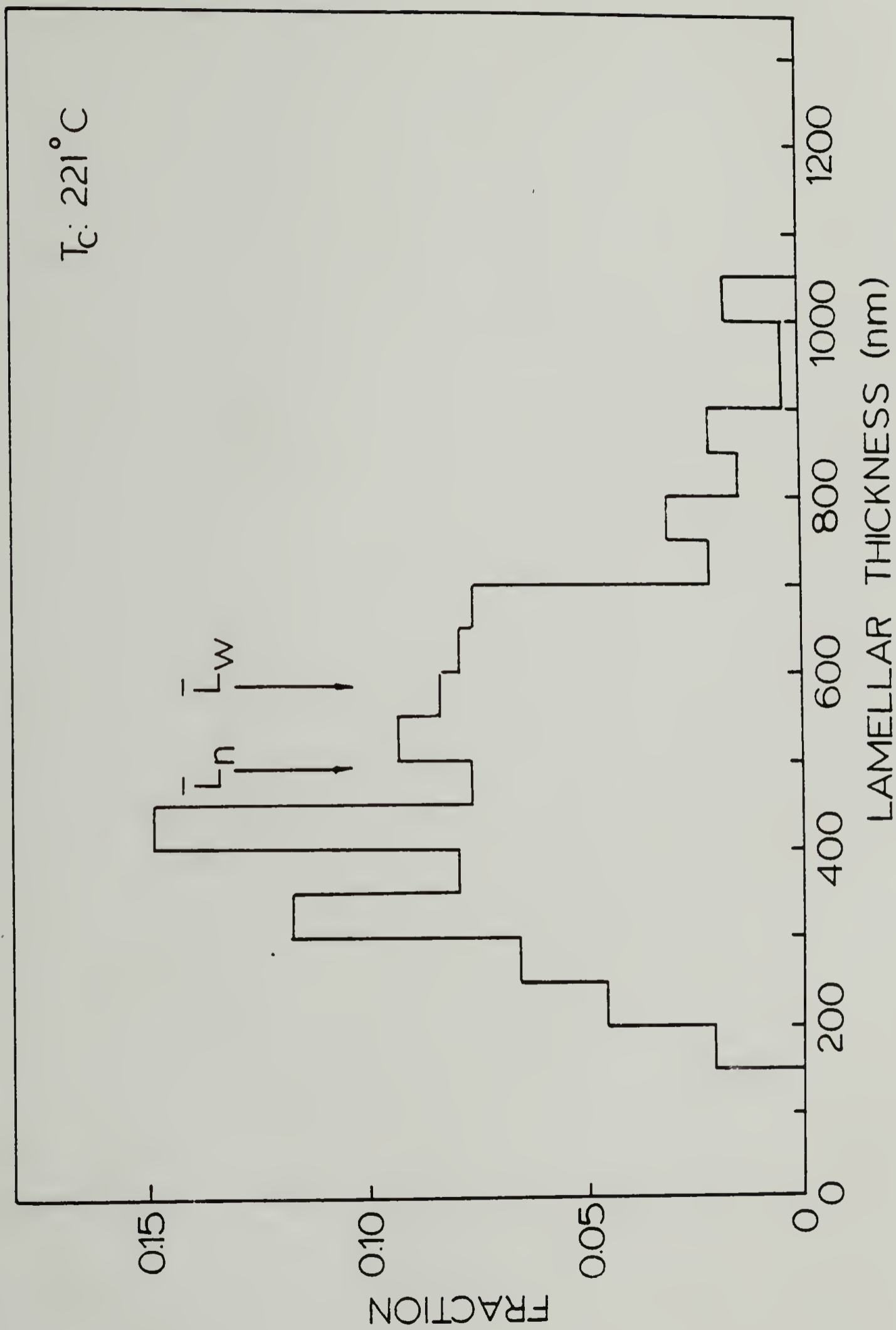


Figure 2.2(a)

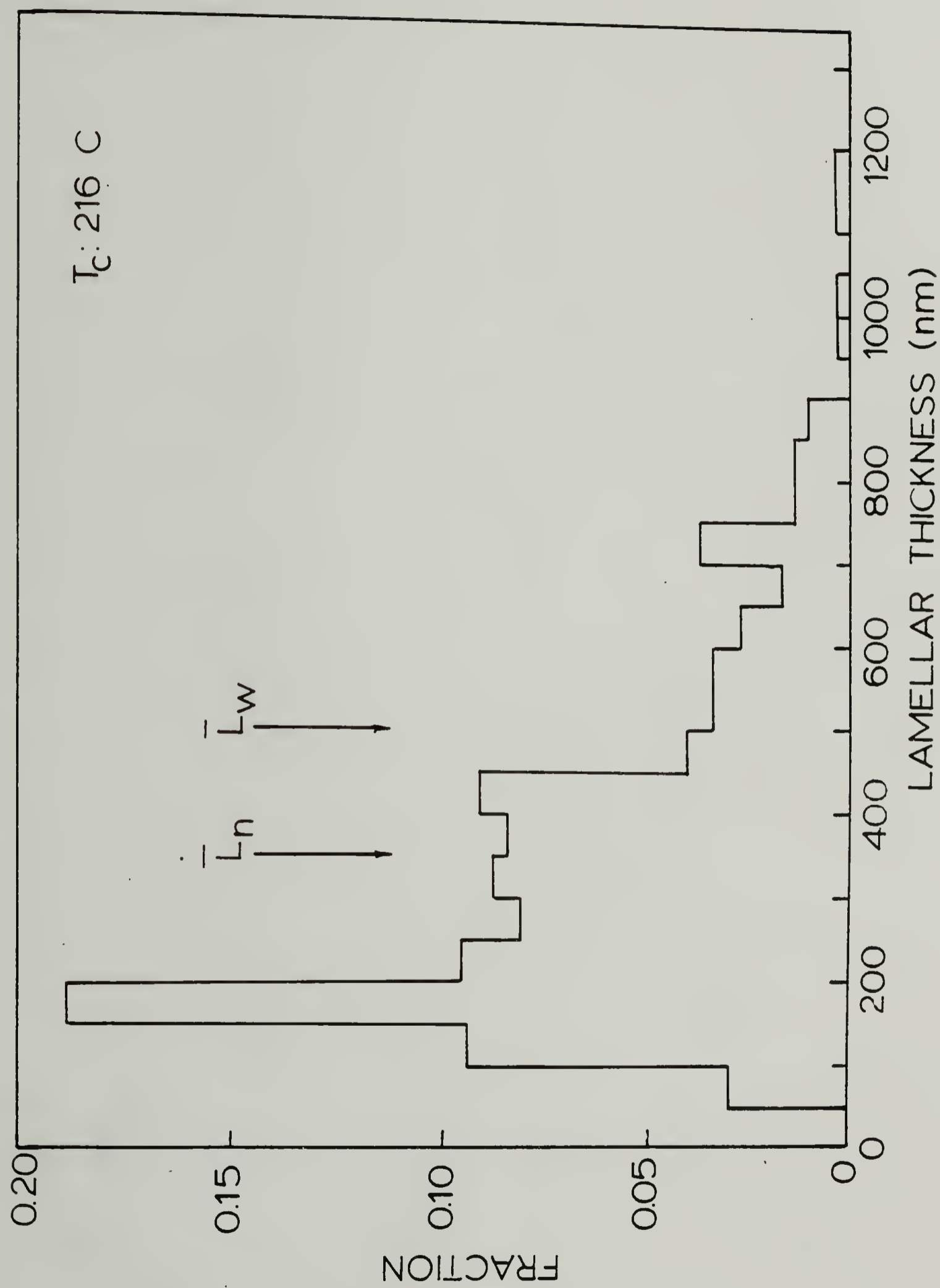


Figure 2.2 (b).

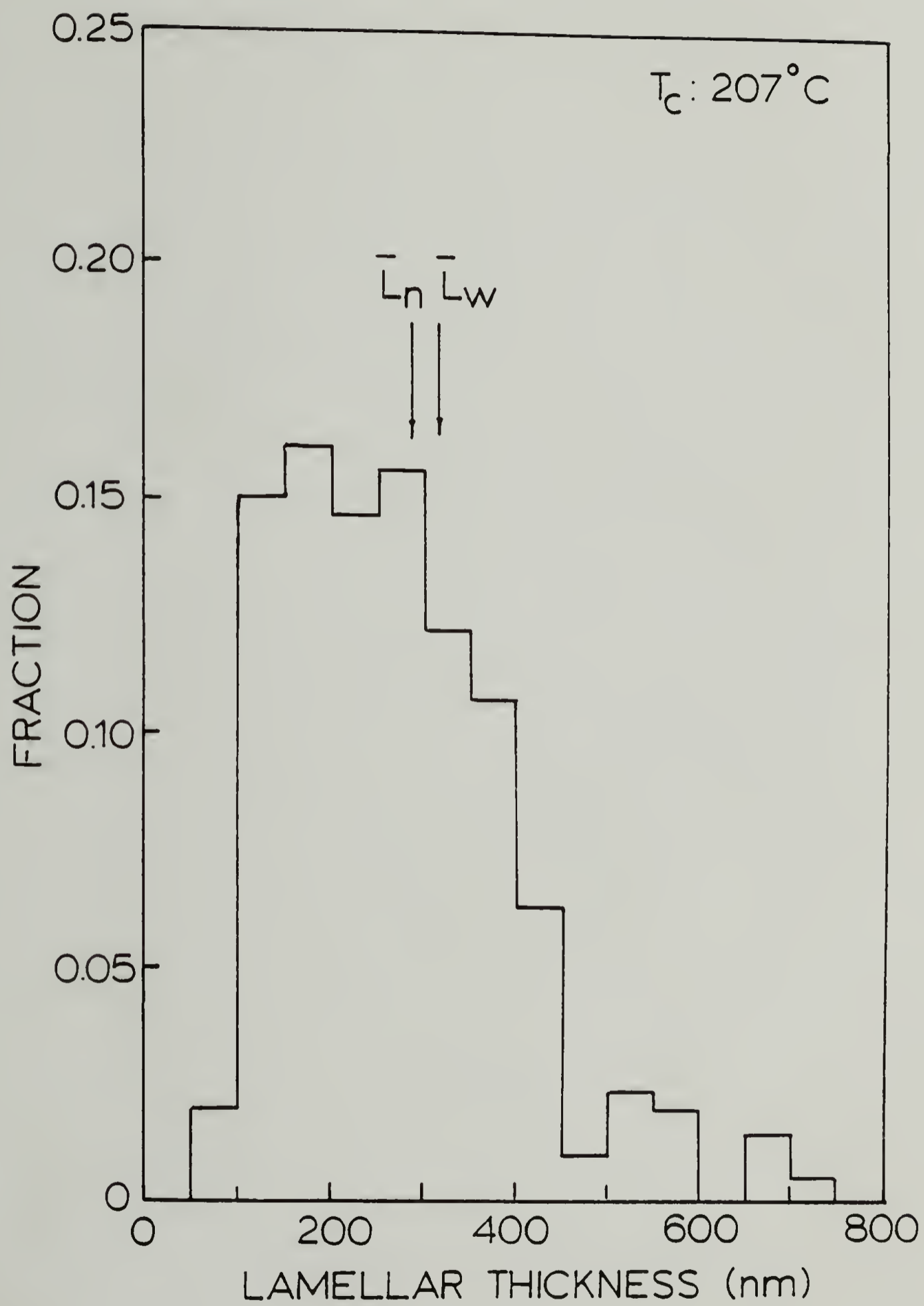


Figure 2.2(c)

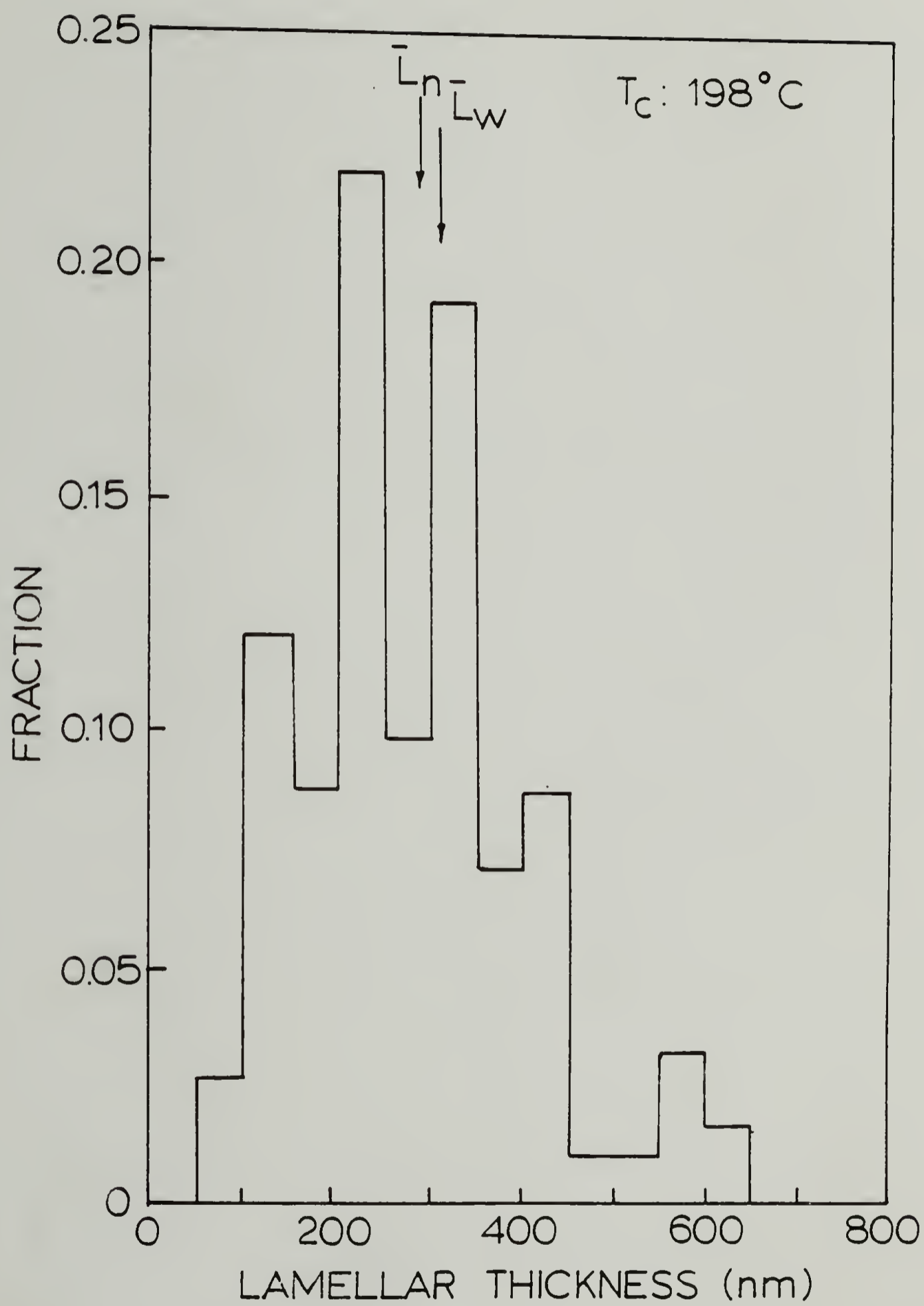
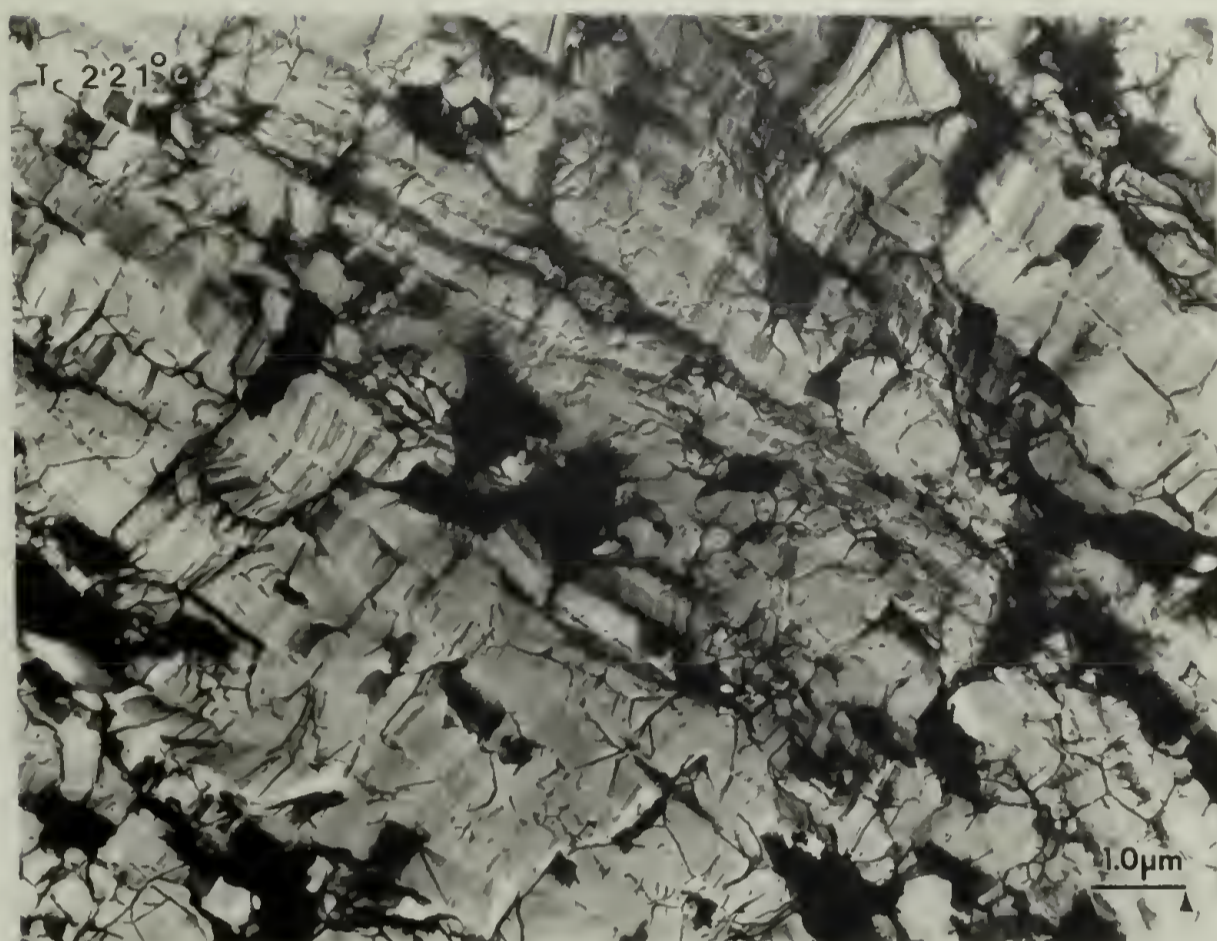
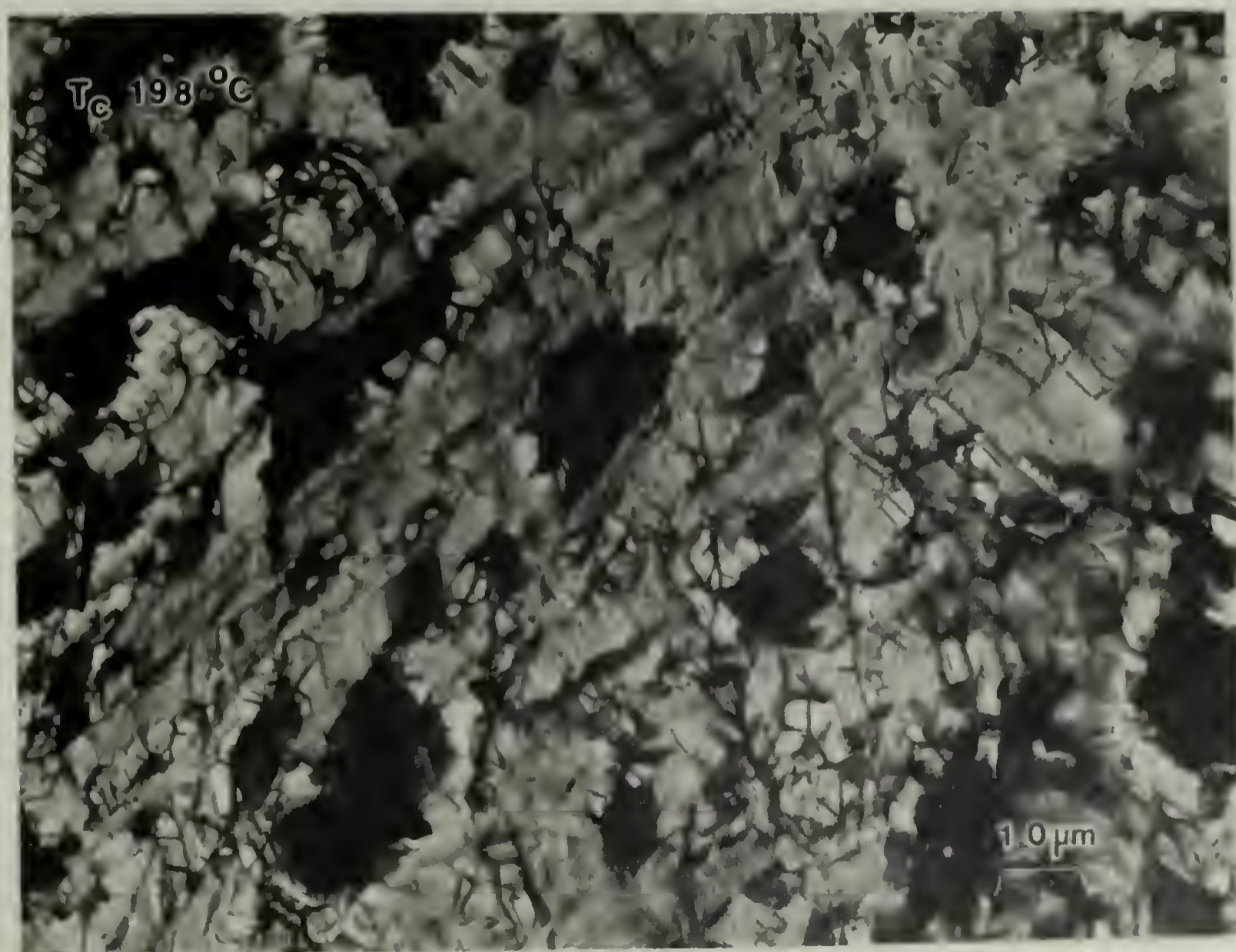


Figure 2.2(d)

Figure 2.3. Transmission electron micrograph of fracture surface replicas of undrawn billets (a) T_c 221°C and (b) T_c 198°C.



(a)



(b)

polystyrene spheres of known diameter must be deposited on the fracture surface for thickness calibration at local regions [73]. It was shown that if the fracture surface is tilted by 30° , the error involved by assuming it is flat is $\sim 13\%$ [74]. A further problem is that the fracture surfaces tend to under record lamellae of low thickness especially the chain-folded fractions which do not fracture well [75]. A more satisfactory method for lamellar thickness distribution characterization is the nitration/gel permeation chromatography (GPC) technique. The crystal surfaces are degraded by the fuming nitric acid and the molecular chain lengths are determined by GPC to give their distribution. This method gives the distribution in much more detail [76]. Despite the shortcomings of lamellar thickness distribution measured from fracture surfaces, when done carefully, it is reliable and reproducible, and reportedly correlates well with the nitration/GPC method [77]. In the present study, it does show the trend of decreasing L_n with decreasing T_c .

Fig. 2.3(a) shows the micrograph of a fracture surface of billet 1, crystallized at 221°C . The fracture surface is clean showing well ordered, large strips of thick lamellae. Fig. 2.3(b) is the micrograph of the fracture surface of billet 4 with the lowest T_c of 198°C . The surface is relatively clean with small amount of

fibrous overlay. The lamellae, however, appeared fragmented and more disordered with lower crystallinity (Table 2.1). The above observation agreed with the conclusion of Rees and Bassett [54]. A parallel trend of forming more disordered lamellae and lower crystallinity is also observed when a PE of higher molecular weight is crystallized [78]. The fractured surface in this case showed large amounts of fibrous overlay which were pulled out from the lamellae during the fracture process. The extent of fibrous overlay can be qualitatively related to the concentration of tie molecules between lamellae. The micrographs of our billets showed relatively clean fracture, suggesting few interlamellar tie molecules. This conclusion is also reached from the consideration of molecular chain lengths and the number of chain folds in lamellae. The full chain lengths corresponding to the M_w and M_n of Alathon 7050 are 540 and 170 nm respectively which are of the same magnitude as the measured number average lamellar thickness. At the highest T_c of 221°C, on the average this arithmetic means there is only a single fold per chain, increasing toward two with decreasing T_c . A large portion of the chains must be fully extended and thicker lamellae could have more than one fully extended chain to make up the thickness.

Interlamellar connection is related to the number of folds possible [39]. A long chain can either fold back or

be incorporated into the neighboring lamella forming tie molecule. The small number of folds per chain suggests that these thick lamellae exist as near individual entities with few interlamellar connections. As T_c was decreased, the amorphous content increased, as loci where chain entanglements may likely exist within the fold loops between lamellae. These trapped entanglements and the increased interlamellar links have a profound effect on the drawing behavior of CEPE, as discussed in Section 2.3.3.

2.3.2 Thermal Analysis

DSC scans of the extrudates are shown in Fig. 2.4 to 2.7. CEPE is known to superheat at high heating rates, resulting in higher apparent melting points. The small sample size used and the low heating rate of $2.5^\circ\text{C}/\text{min}$. minimize this effect. Three to four overlapping endotherms are observed for the undrawn billets. In billets 1 and 2, Fig. 2.4 and 2.5, the highest peak melting point occurs at 141°C corresponding to the melting of large chain-extended lamellae. Significantly smaller endotherms are noted at lower temperatures of 129° and 134°C and these have been attributed to chain-folded fractions [54] or low molecular weight fractions segregated during crystallization and subsequently crystallized into chain-extended lamellae during cooling [55].

Figure 2.4 to 2.7. Melting endotherms of billets 1 to 4 and their extrudates in increasing draw ratio.

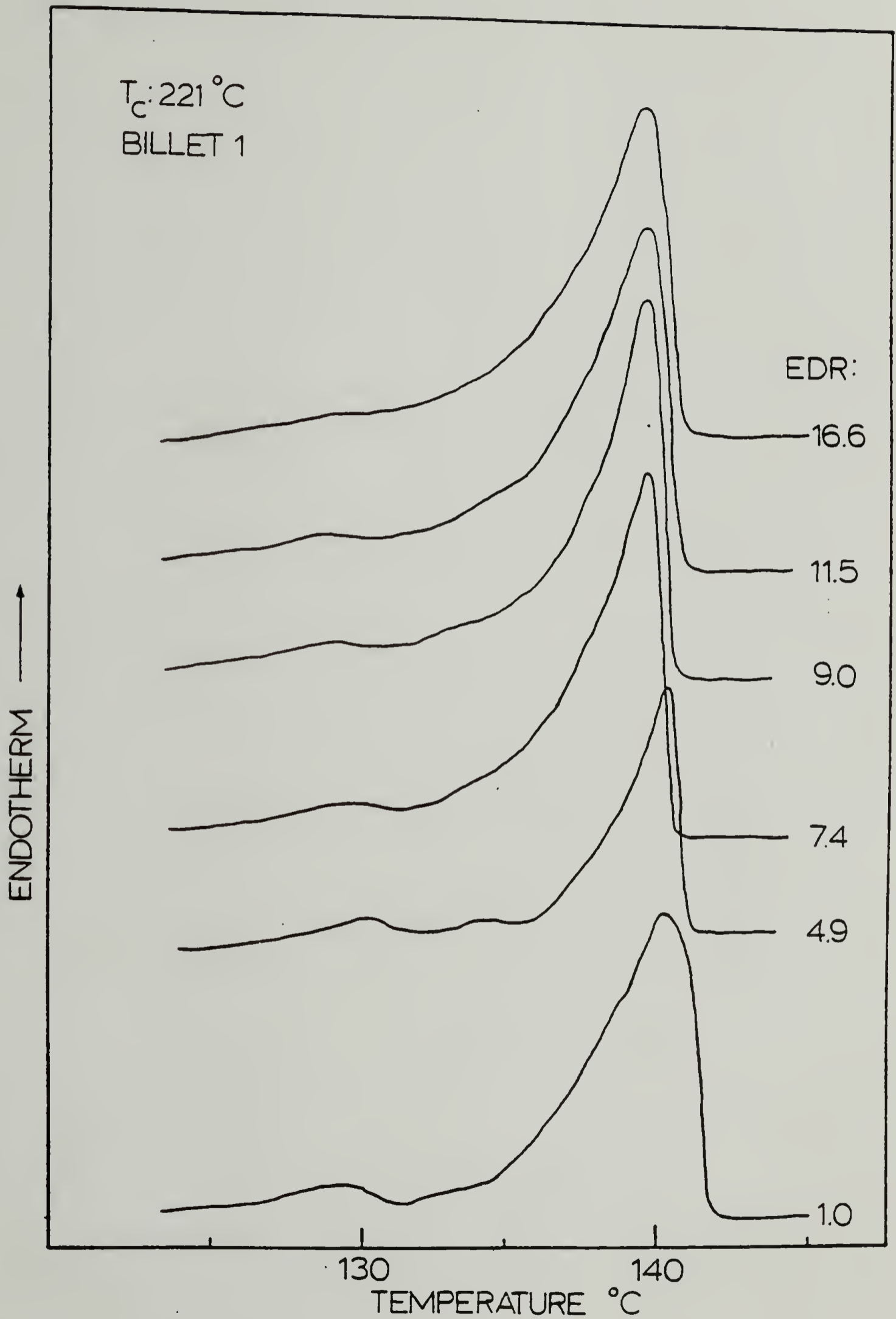


Figure 2.4

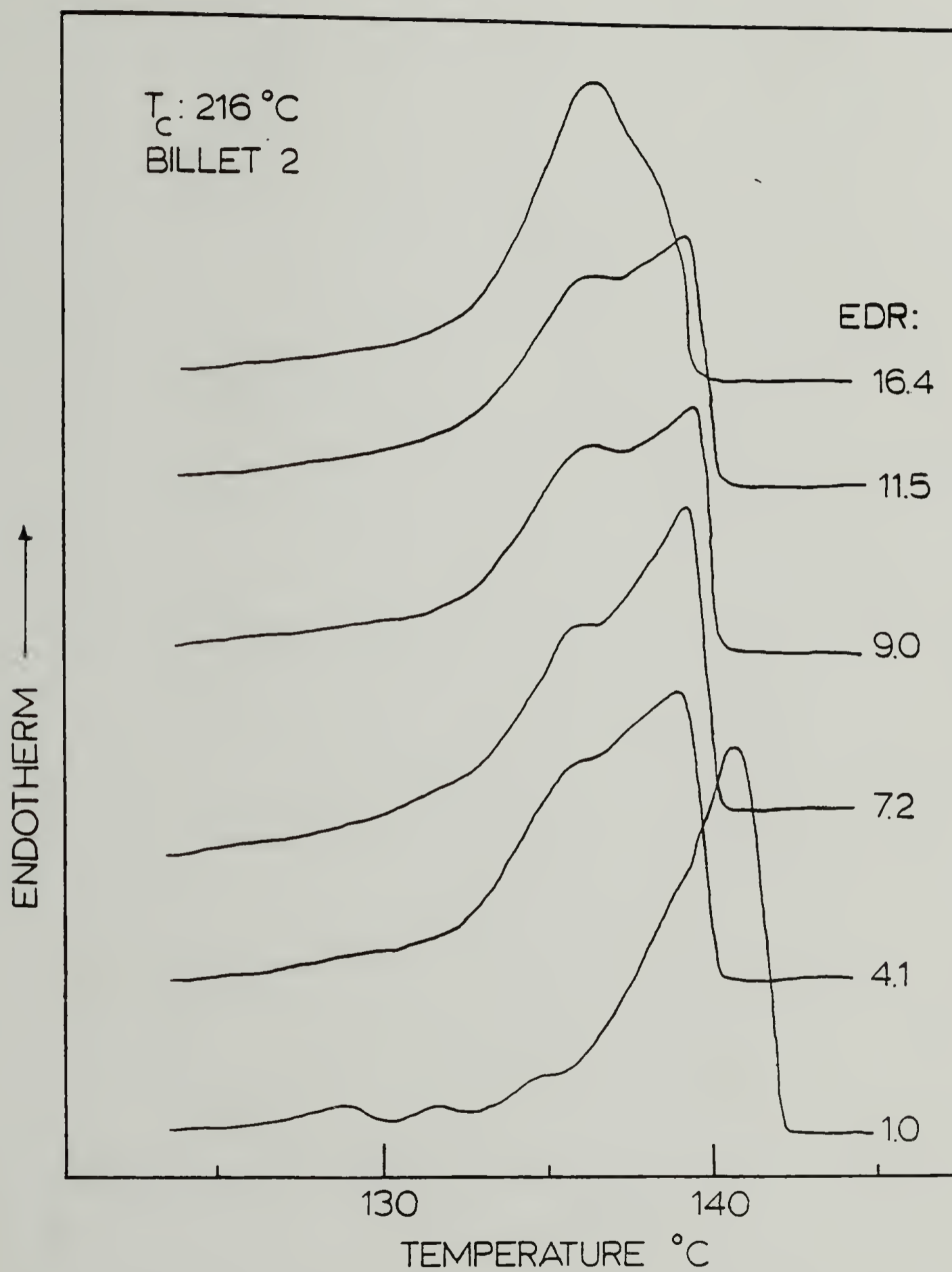


Figure 2.5

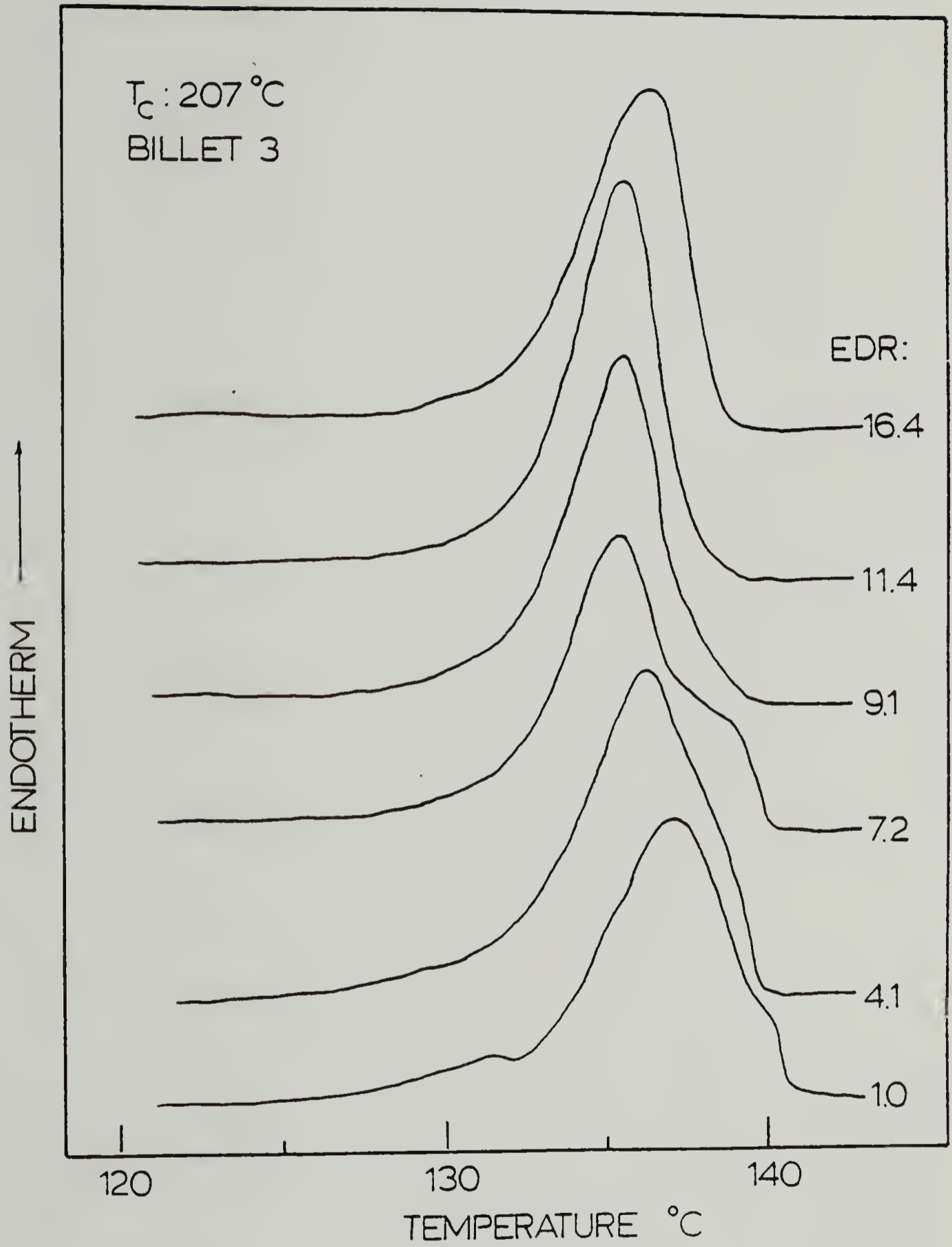


Figure 2.6'

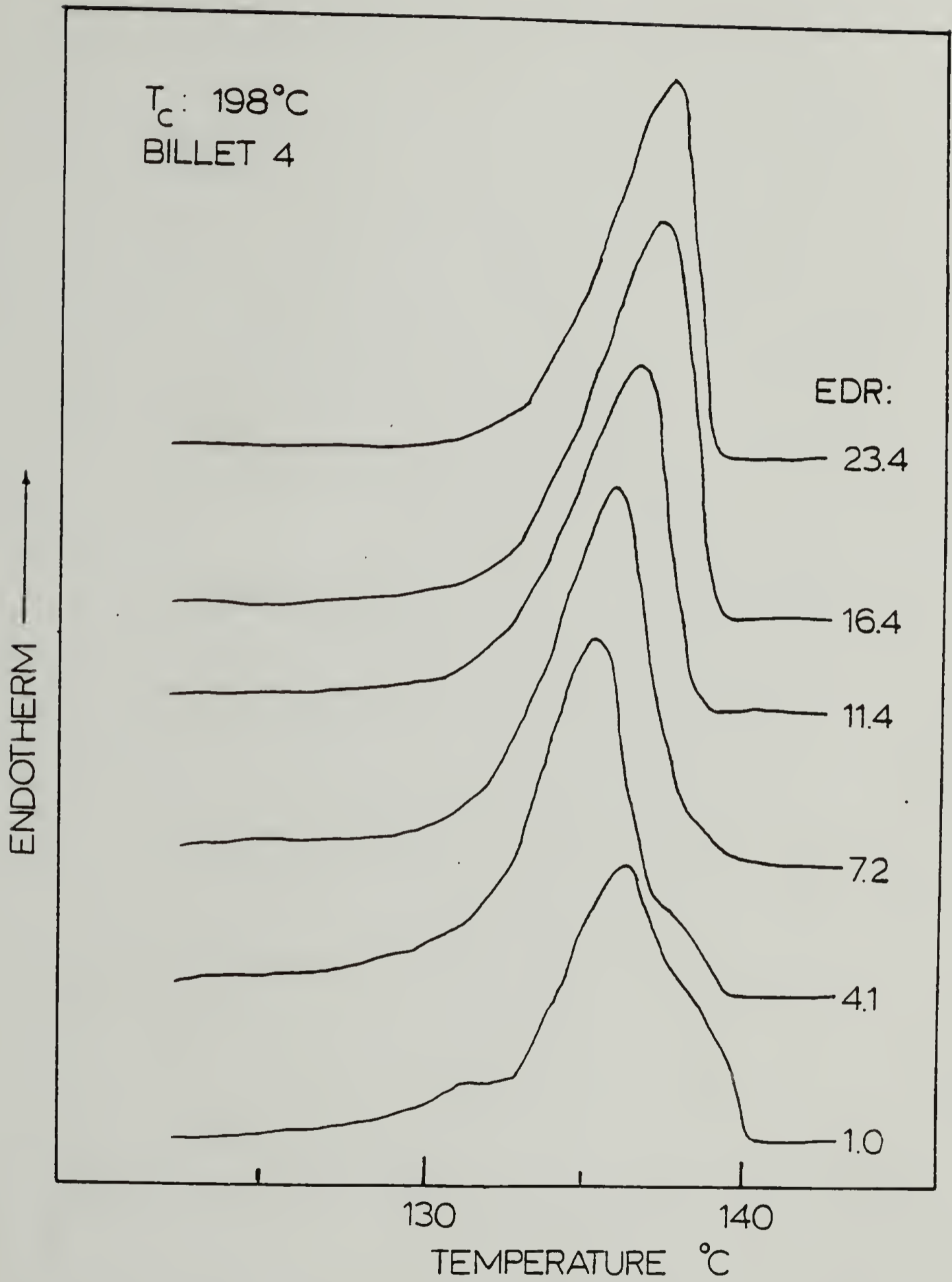


Figure 2.7

Billets 3 and 4 which are crystallized at lower temperatures show three endotherms, Fig. 2.6 and 2.7 . The main melting peak centers at 137°C with a higher temperature shoulder at 140°C and a small endotherm at 131°C . The melting point of 137°C is too high to be due to chain-folded crystals. On examining the lamellar thickness distribution of billet 3, Fig. 2.2(c) shows a bimodal distribution with 3% of the lamellae having a thickness of $\sim 1\ \mu\text{m}$, the majority are between 130 \sim 400 nm thick. The endotherm at 137°C is thus likely due to these thinner chain-extended crystals while the high temperature shoulder is due to the small fraction of the very thick lamellae. A bimodal thickness distribution was also reported by Maeda and Kanetsuna [76] using the more sensitive nitric acid and GPC method. They detected two separate fractions, the "ordinary" fraction has thickness $1/3 - 1/2$ that of the "highly" chain-extended crystals.

Fig. 2.4 shows the change of melting behavior in extrusion drawing of billet 1. The highest peak melting point remains virtually unchanged, decreasing by less than 1°C with increasing draw up to EDR 16.6. The lower temperature endothermic maxima decreases in magnitude and merges to become a single smooth endotherm at high draw. The slight decrease in melting point indicates that lamellar disruption during drawing is not extensive, and a substantial amount of lamellae have been observed in

electron micrographs of fracture surface replicas to exist undeformed up to EDR 7.4 (Fig. 2.15). At higher draw, isolated lamellae could still be found embedded in the fibrillar structure.

The extrudates drawn from billet 2 showed a different thermal behavior (Fig. 2.5). At EDR 4.1, the highest melting peak decreases by 2°C to 139.5°C and this temperature remains almost constant on further drawing. The low temperature endotherm is replaced by a peak at 136°C , its magnitude increases with draw, while the high temperature peak reduces to a shoulder. Here the destruction of chain-extended lamellae is associated with a decrease in the high melting peak and the formation of the fibrillar structure indicated by the simultaneous appearance of the 136°C endotherm. The associated decrease in crystallinity on draw is $\sim 7\%$ (Fig. 2.8).

Drawing of billets 3 and 4 with progressively more disorder and smaller initial lamellae (Fig. 2.6 and 7) shows a rapid reduction in both the high and low temperature endotherms leaving a single peak at EDR > 9.1 and > 7.2 respectively. The peak temperature of the endotherm at 138°C for the thinner chain-extended lamellae decreases initially and increases again reaching 137°C as draw reaches an EDR of 16.4. Billet 4 shows better drawability and can be readily drawn to an EDR 23.4 without noticeable fracture.

In the drawing of conventional chain-folded PE, a single endotherm is usually observed and the peak melting point increases reaching a plateau of 139°C , contrary to the decrease of melting point we have observed on drawing of CEPE. This opposite trend of decreasing melting point is to be expected as chain-extended morphology approaches the thermodynamic equilibrium state and the equilibrium melting point. Any disruption of the lamellae will likely result only in its decrease. It is noted in Fig. 2.4 to 2.7, there is a tendency of forming a single endotherm and for the melting point to approach 137°C at high draw even though the initial morphologies varied. Although a high temperature shoulder is observed in EDR 16.4 of billet 2, its magnitude decreases and a single endotherm should be observed if higher draw can be achieved. The approach to single endotherm and plateau melting point must therefore indicate an approach to a common morphology at high draw. This result is an indication of complete transformation of lamellae to fibrillar structure at an EDR of 7 to >16 for the four different initial morphology CEPE. Transformation is not complete for billet 1 before fracture occurs.

The DSC measurements were made on samples that are free to shrink on melting. Unrestrained samples relax and reorganize prior to melting, causing narrowing of the peak [79]. The entropic shrinkage has an exothermic component

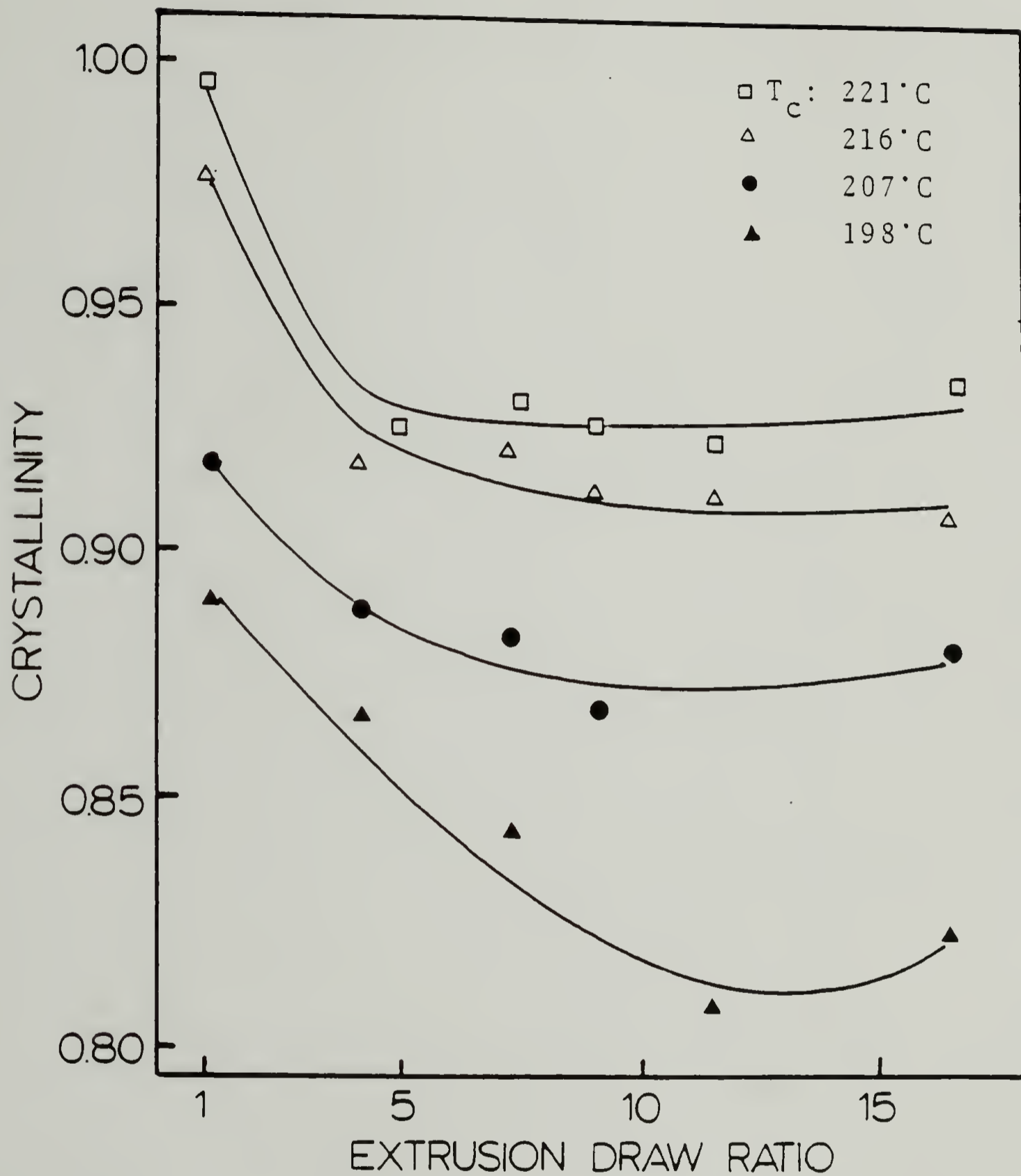
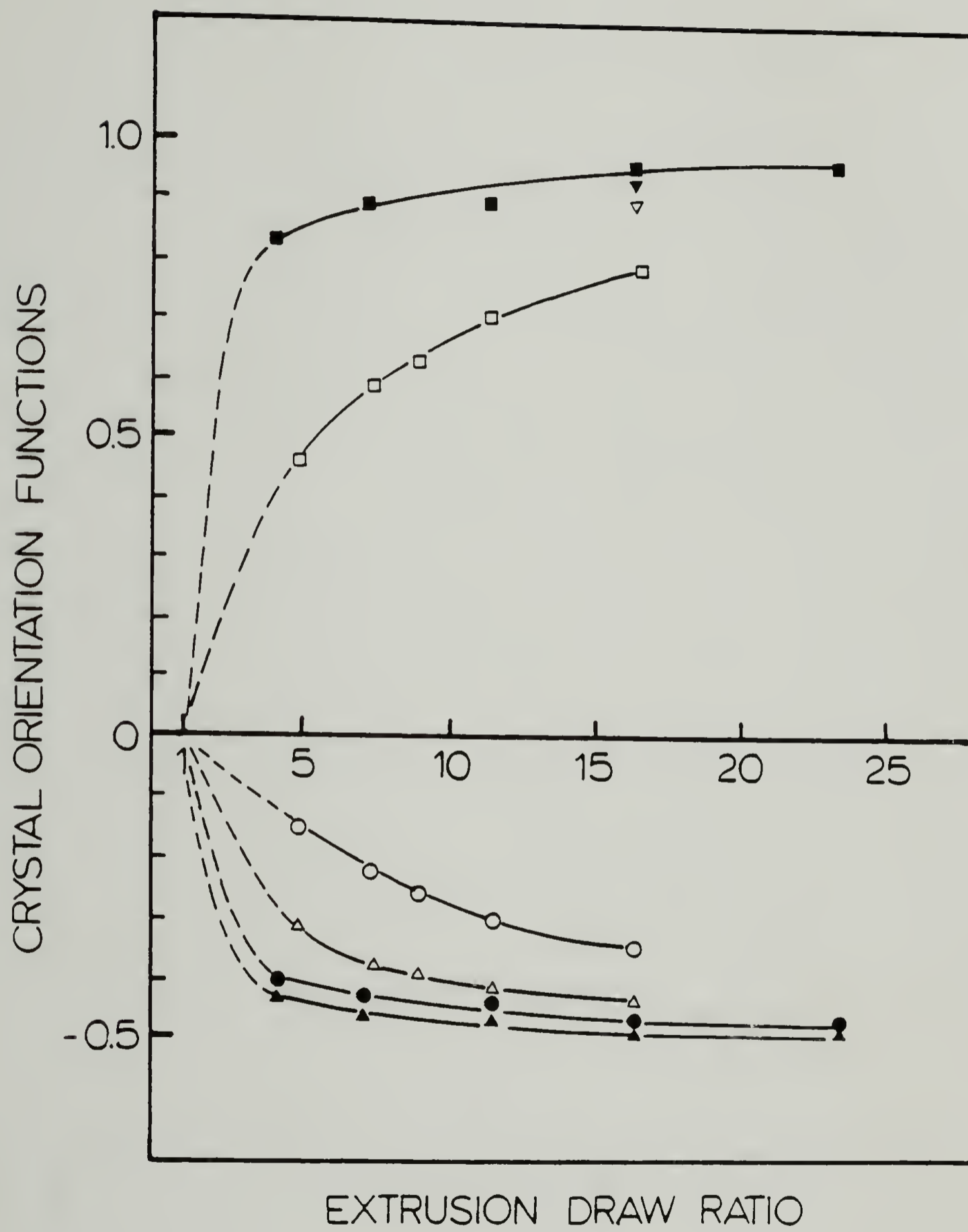


Figure 2.8. Change of crystallinity as a function of extrusion draw ratio as measured by DSC for the four billets.

Figure 2.9. Change of crystal orientation function f on drawing for the three crystallographic axes a , b and c for drawn billets 1 ($T_c = 221^\circ\text{C}$) (\blacktriangle , \bullet , \blacksquare) and 4 ($T_c = 207^\circ\text{C}$) (\triangle , \circ , \square); f_c of billets 2 (∇) and 3 (\blacktriangledown) drawn to EDR 16.4 are inserted for comparison.



and can account for the measured heat of fusion reduced by <3% in unrestrained samples. Therefore the crystallinities from drawn samples shown in Fig. 2.8 are in actuality a few % higher.

2.3.3 Orientation and Molecular Draw Ratio

Orientation of the extrudates is evaluated by WAXD and expressed by the crystal orientation function, f_i . Fig. 2.9 shows the change of f_i for the three crystallographic axes a, b and c with EDR for drawn billets 1 and 4. f_c increases slowly with draw for billet 1 but very rapidly for billet 4, in a way comparable to the development of orientation in the drawing of chain-folded PE [80]. Similar behavior is observed in the development of the a- and b-axis orientation. The a-axis orients faster than the b-axis at low draw, both reaching a limiting value of ~ -0.5 at EDR >10 . This difference is clearly shown in the drawing of billet 1, and persists even at EDR 16.4.

The effect of the initial morphology on orientation is shown by comparing f_c of the four billets at the same draw of 16.4 (Fig. 2.9). f_c increases as the crystallization temperature of the initial billet is decreased.

MDR from thermal shrinkage is an alternate way of showing the effect of initial morphology on drawing. At a high heating rate of $\sim 800^\circ\text{C}/\text{min}$, the molecular extension

produced by drawing can be elastically recovered. The measurement of the recovery when compared to the initial length gives the MDR. This method was reported to correlate with results obtained by small-angle neutron scattering in drawn polystyrene [81]. In defining draw efficiency as the ratio between MDR and EDR, Fig. 2.10 shows that this ratio increases as the crystallization temperature of initial billet is decreased, reaching a maximum of 0.71 in solid-state extrusion.

The above results show that highly chain-extended PE orients ineffectively on draw. The drawability and draw efficiency appear to be aided by increasing chain entanglements in the amorphous region in this case. The effect of entanglements on drawing has received much attention. Their reduction enhances chain mobility and can result in very highly drawn PE such as in the gel fiber drawing [82], in which the entanglement density is reduced by solvent dilution. However, the reduction is not without limit. Severe reduction results in an insufficient transient network that is required to effectively transfer stresses during deformation [83]. In melt crystallized PE, the entanglement density is high. Fischer [84] studied the drawing of melt crystallized PE and found that higher draws could be obtained if samples had been crystallized at a higher pressure of 2.85 kbar. The increase in drawability was attributed to the

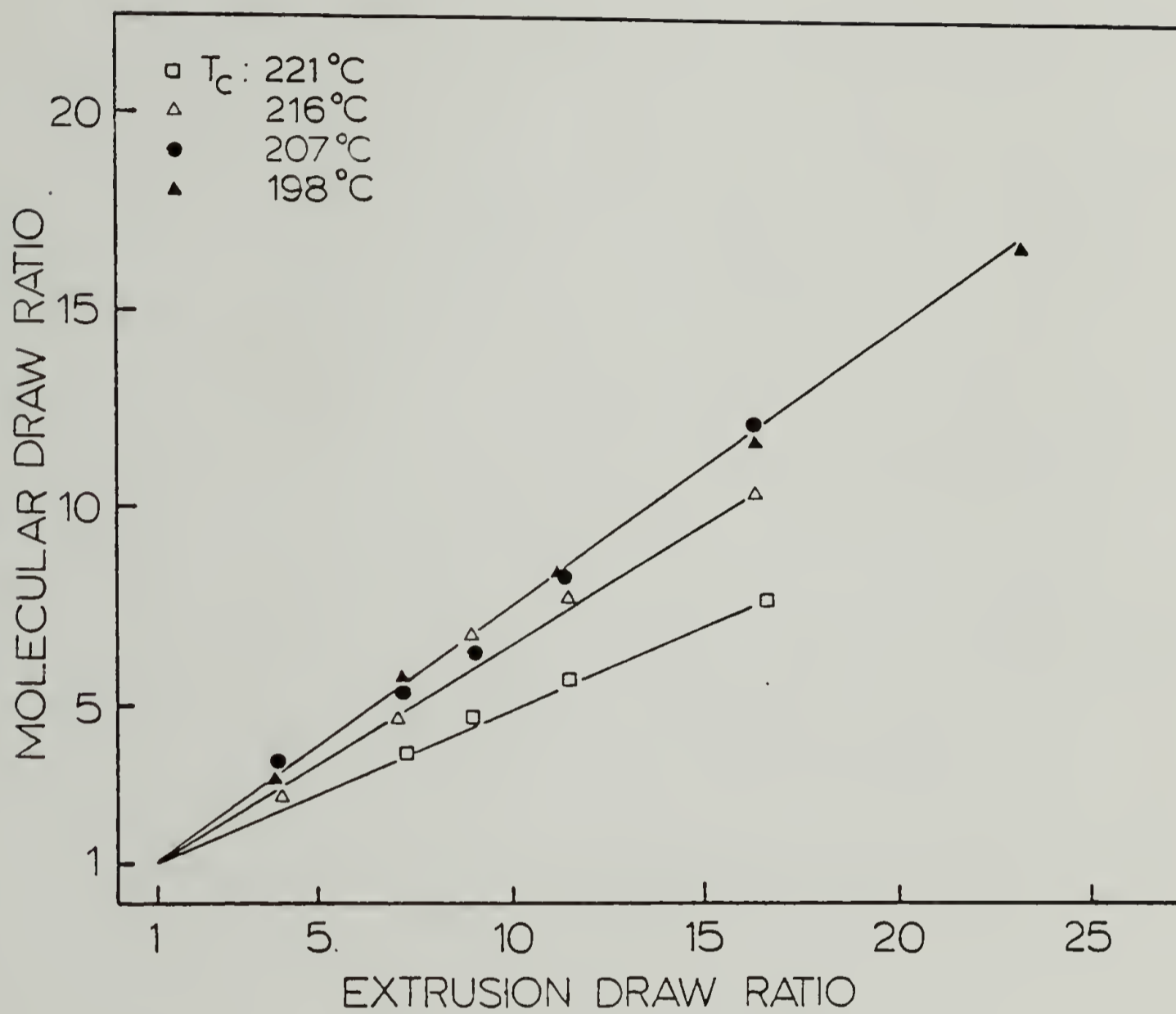


Figure 2.10. Molecular draw ratio (MDR) vs. extrusion draw ratio (EDR) showing the effect of initial morphology on efficiency of drawing (MDR/EDR).

reduction in entanglements as a more chain-extended crystal structure is approached.

In the present study, the approach is from the opposite end. Highly crystalline CEPE has a lamellar thickness comparable to its molecular chain length, and therefore has fewer interlamellar links and trapped entanglements. In the extreme, this approaches the situation of a single crystal mat. For the billet crystallized at the highest temperature of 221°C, the drastically reduced entanglements in the amorphous phase caused the lamellae to slip past each other as whole entities during drawing, resulting in poor orientation. The ductility, despite few entanglements, must be due to the compression and constraint imposed by the solid-state extrusion process: compacting the lamellae, transfer of stresses for shearing and forcing chains to unravel on passing through the conical die during extrusion. For decreasing T_c and a consequent increase of amorphous content and entanglements, as in billets 3 and 4, drawability and draw efficiency increase. An increase of amorphous content by 5% and lowering the number average lamellar thickness by half, markedly alters drawing behavior, almost doubling the drawing efficiency.

2.3.4 Correlation Between Modulus and Molecular Draw Ratio

Tensile modulus is the property of primary interest

in ultra-drawn polymers. It is thus desirable if it can be correlated with a measurable quantity, such as the orientation function which reflects how well the chains are aligned in the draw direction. The crystal orientation function, f_c , generally increases sharply on initial draw, reaching a plateau value of almost 1.0 at high draw [80]. It is no longer meaningful to measure f_c due to the insensitive measured numerical increase in this plateau region. Therefore plots of modulus vs f_c are non-linear. However, the amorphous orientation function, f_a , can increase more gradually with draw. The use of f_a to correlate with modulus has therefore been successful for amorphous poly(ethylene terephthalate) drawn up to 5X [85]. Here the compliance ($1/E$) is a linear function of $(1-X_v)f_a$, where X_v is the volume fraction of crystallinity.

Several investigators [86-88] had found a linear relationship between modulus, E , and draw ratio, λ , for PE. Cappacio and Ward [86] found linearity irrespective of molecular weight and initial thermal history, however, extrapolation of such plots to the original undrawn state ($\lambda = 1$) gives a negative modulus. This is due to the fact that the experimental λ does not scale the actual molecular draw; it is therefore not a fundamental parameter for correlation.

Grubb [89] had proposed a relationship between E and

λ in the form of

$$1/E = B + C\lambda^{-2} \quad (2.15)$$

where B and C are constants, based on a modified Takayanagi model by incorporating an entanglement fraction. This reportedly gave a linear fit for drawn solid PE and dried PE gel. The same equation was independently deduced by Fischer et al. [90] from empirical fitting of their experimental data.

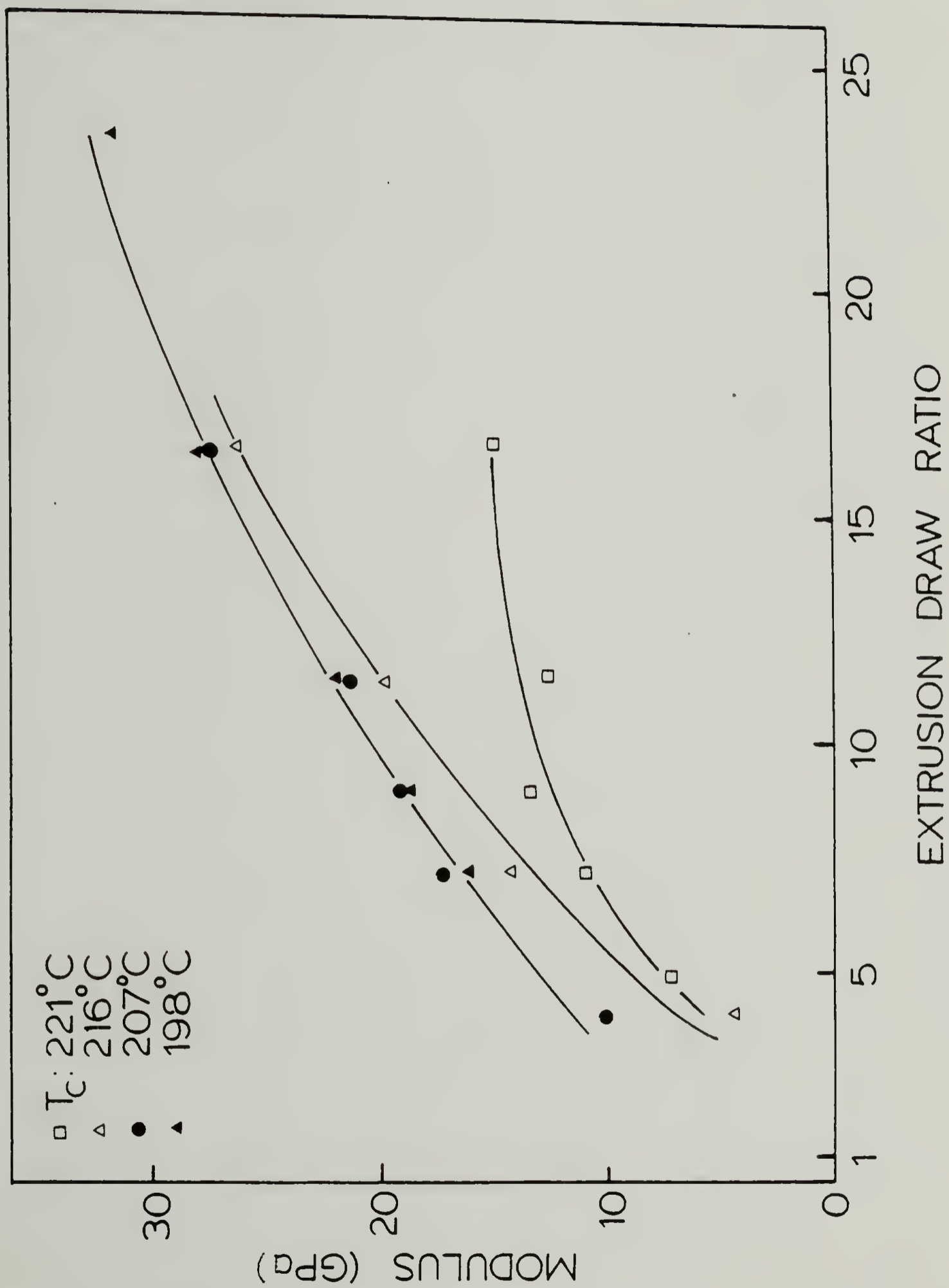
Alternatively, we propose here the use of molecular draw ratio (MDR) as a fundamental parameter for correlation with modulus. Fig. 2.11 shows the plot of modulus of the extrudates vs EDR. Modulus increases with draw but remains low, 33 GPa for the highest EDR, 23.4, achieved here. On comparing the modulus at equivalent EDR for the four drawn billets, billet 1 showed the lowest modulus, followed by billet 2. However, extrudates from billets 3 and 4 showed nearly the same increase of modulus with draw. Fig. 2.11 thus showed an apparent dependence of the extrudate modulus on the initial morphology of the billets. This is because highly chain-extended PE draws ineffectively with slow development of orientation. Both billets 1 and 2 have a low draw efficiency of 0.44 and 0.64 respectively, while billets 3 and 4 have a draw efficiency of ~ 0.71 which is the limit presently achievable in solid-state extrusion. Thus equivalent EDR

gave different MDR for each extrudate and therefore the apparent dependence of morphology.

Fig. 2.12 is a plot of E vs MDR. In this form, the apparent effect of initial morphology is erased. This plot includes data from a previous extrusion-draw study [61] of high molecular weight PE (Marlex 6003, M_w 250,000) and on Alathon 7050 drawn by other techniques: viz. by split billet, by push-pull extrusion and at constant draw temperatures between 80 and 120°C. Fig. 2.12 shows a linear relationship with a correlation coefficient of $r = 0.97$ by least-square fit, and the probability function [91], $P_c(r, N) < 0.001$. This indicates that E linearly correlates with MDR with high probability. Moreover, extrapolation to the undrawn state (MDR=1) gives an E of 1.7 GPa, which is the magnitude for the undrawn PE.

Grubb's equation was also plotted with $1/E$ against $(EDR)^{-2}$ or $(MDR)^{-2}$. This give a less satisfactory fit with $r = 0.64$ and 0.66 respectively. The use of MDR for EDR did not improve linearity. This equation gives excessive weight to low modulus and draw, yet replotting with modulus data of $MDR > 5$ did not significantly improve the correlation. It is, therefore, concluded from the above that modulus is a linear function of MDR for PE. This correlation is independent of draw temperature, initial morphology irrespective of chain-folded or chain-extended, variation in draw technique and molecular

Figure 2.11. Tensile moduli of CEPE at increasing extrusion draw ratio.



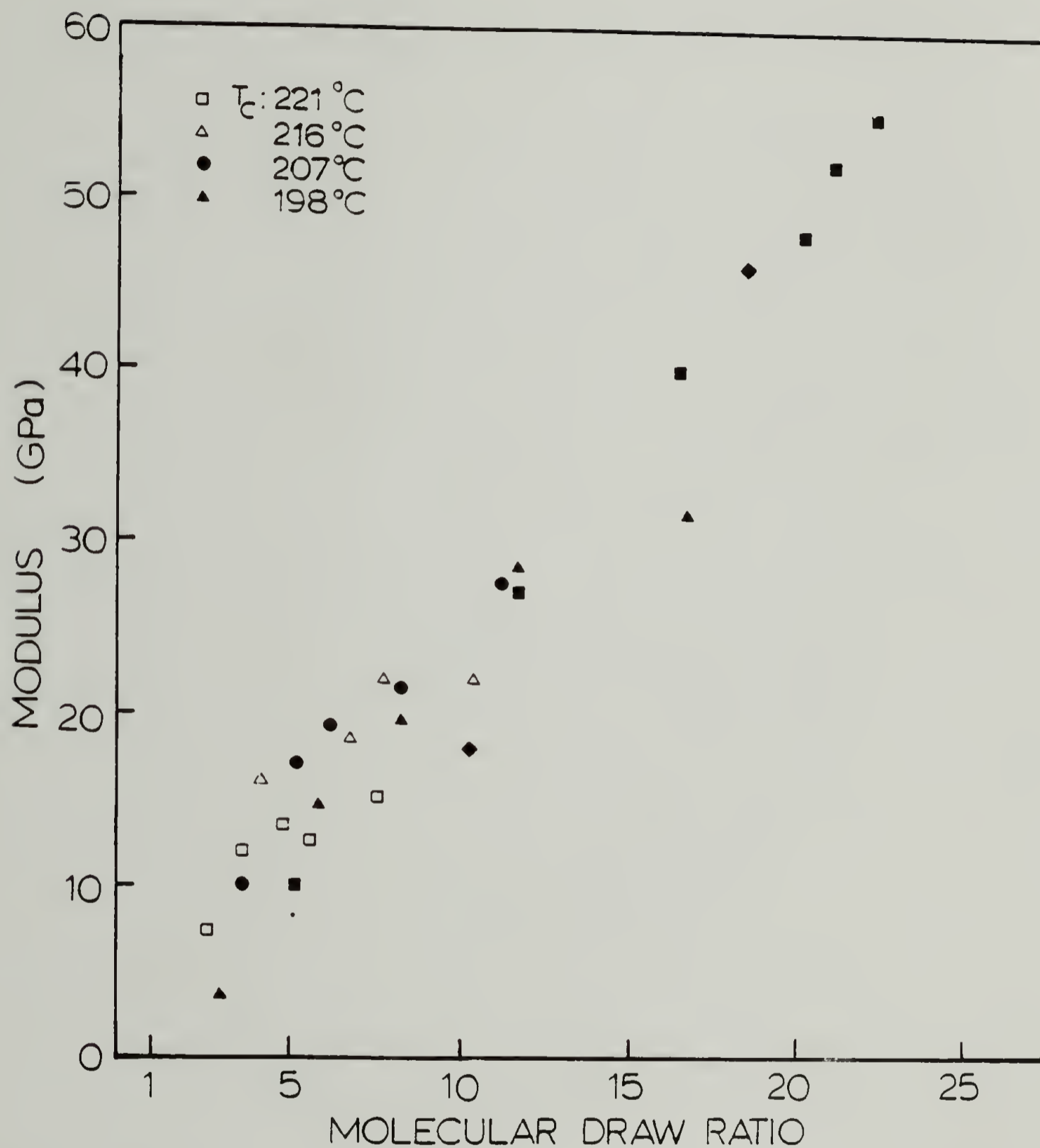


Figure 2.12. Tensile moduli of CEPE as a function of molecular draw ratio. ■ and ◆ are chain-folded PE data from reference [61].

weight of HDPE. MDR can therefore be a good parameter when comparing moduli of drawn PE by the different drawing methods.

2.3.5 Crystallite Size and Distortion

Crystallite size can be determined from the broadening of the diffraction profile by WAXD using Scherrer's equation, with the assumption that broadening is due to size alone. The use of this method is often limited by the resolution of the instrument. For most X-ray diffractometers, the upper limit of the measured crystallite size is in the order of 100 nm. However, using a high resolution diffractometer, Schonfeld and Wilke [92] measured CEPE lamellae with a coherent lateral dimension of more than 200 nm. Table 2.2 lists the crystallite size measured from the (110), (220), (200) and (020) planes for billet 1, using Scherrer's equation and the Gaussian approximation of equation 2.13.

With careful alignment and using narrow slits, the instrumental broadening of the D-500 diffractometer is reduced to a reasonably small value, 0.08° . The lateral crystallite sizes along the (200) and (020) planes are 42 nm, and along the diagonal (110) planes the size is 44 nm (Table 2.2). These sizes are unusually smaller than would be expected for a CEPE. There are several possible reasons: the use of Scherrer's equation by ignoring the broadening effect due to distortion gives a lower

estimate; there could be the presence of defects in the crystal, effectively dividing it into smaller coherent dimensions for diffraction. It was also reported that, when the profile broadening is small compared to the instrumental broadening, Cauchy's approximation should be used instead [67], which increases the measured crystallite size to ~63 nm for (200) and (002) planes, and 67 nm for the (110) planes as shown in column two of Table 2.2. A further consideration of the distortion effect using Hosemann's equation and the second order (220) reflection increases the size only slightly to 71 nm. The reason for such a small increase is because the crystals are relatively free of distortion, with $g_{II} = 1.73\%$

More important in the present study is the change of crystallite size on drawing. Fig. 2.13 shows that crystallite size along the (200), (020) and (110) planes decreases sharply on the early stage of drawing and levels off to 29 nm for \bar{D}_{200} , 21 nm for \bar{D}_{020} and 32 nm for \bar{D}_{110} . The rapid decrease is due to the breakup of the lamellae into smaller blocks on drawing. The morphology changes with the development of the fibrils, with its size remaining nearly constant on further drawing as shown in Fig. 2.13 above EDR 10. The different sizes along (110), (200) and (020) planes suggests that the fibril is not circular in cross-section but more of a ellipsoid.

The (002) diffractions are too weak for accurate

measurement in the present study to allow the determination of crystal continuity along the draw direction.

Fig. 2.14 shows Hosemann's distortion parameter, g_{II} for billet 1 as a function of EDR determined from the line broadening of (110) and (220) reflections. The crystals of undrawn billet 1 show low distortion, with $g_{II} = 1.7\%$. i.e. a very small fluctuation of neighboring (110) planes within the crystal lattice. Wilke and Martis [93] had previously measured values of g_{II} of chain-folded PE, before and after drawing to a draw ratio of 16, to be 0.08 and 1.0%, and concluded that g_{II} does not change on drawing. The present results, however, showed that g_{II} increases first on drawing, reaching a maximum of 2.3%, at EDR 7.5, and then decreases on further drawing to 1.4% at EDR 16, a slightly smaller g_{II} than the starting billet. The increase of g_{II} on initial drawing is to be expected intuitively since there is chain tilting, shearing and breaking up of lamellae into blocks as suggested in Peterlin's model of deformation [26] and consequently an increase in statistical fluctuations between neighboring planes. At higher draw, the crystal blocks are incorporated into the newly formed fibrils which slide past each other on further drawing. The size of the fibrils remains constant and g_{II} decreases. The maximum of g_{II} occurs at EDR 7.2, ahead of the draw ratio

Table 2.2

Change of Crystallite Sizes on Extrusion
Drawing for a CEPE Billet Crystallized at 221°C

Extrusion Draw Ratio	Calculated by By Gaussian Approximation			Calculated by By Cauchy Approximation		
	\bar{D}_{110}	\bar{D}_{020}	\bar{D}_{200}	\bar{D}_{110}	\bar{D}_{020}	\bar{D}_{200}
	(nm)			(nm)		
1	44.1	41.9	42.3	67.4	62.0	63.5
4.9	34.1	23.8	30.7	47.6	29.9	41.5
7.4	33.7	22.8	28.1	46.8	28.4	37.1
9.0	32.0	21.0	25.0	43.7	25.7	31.7
11.5	30.1	20.8	28.1	40.5	25.4	36.9
16.6	33.5	-	29.7	46.5	-	39.4

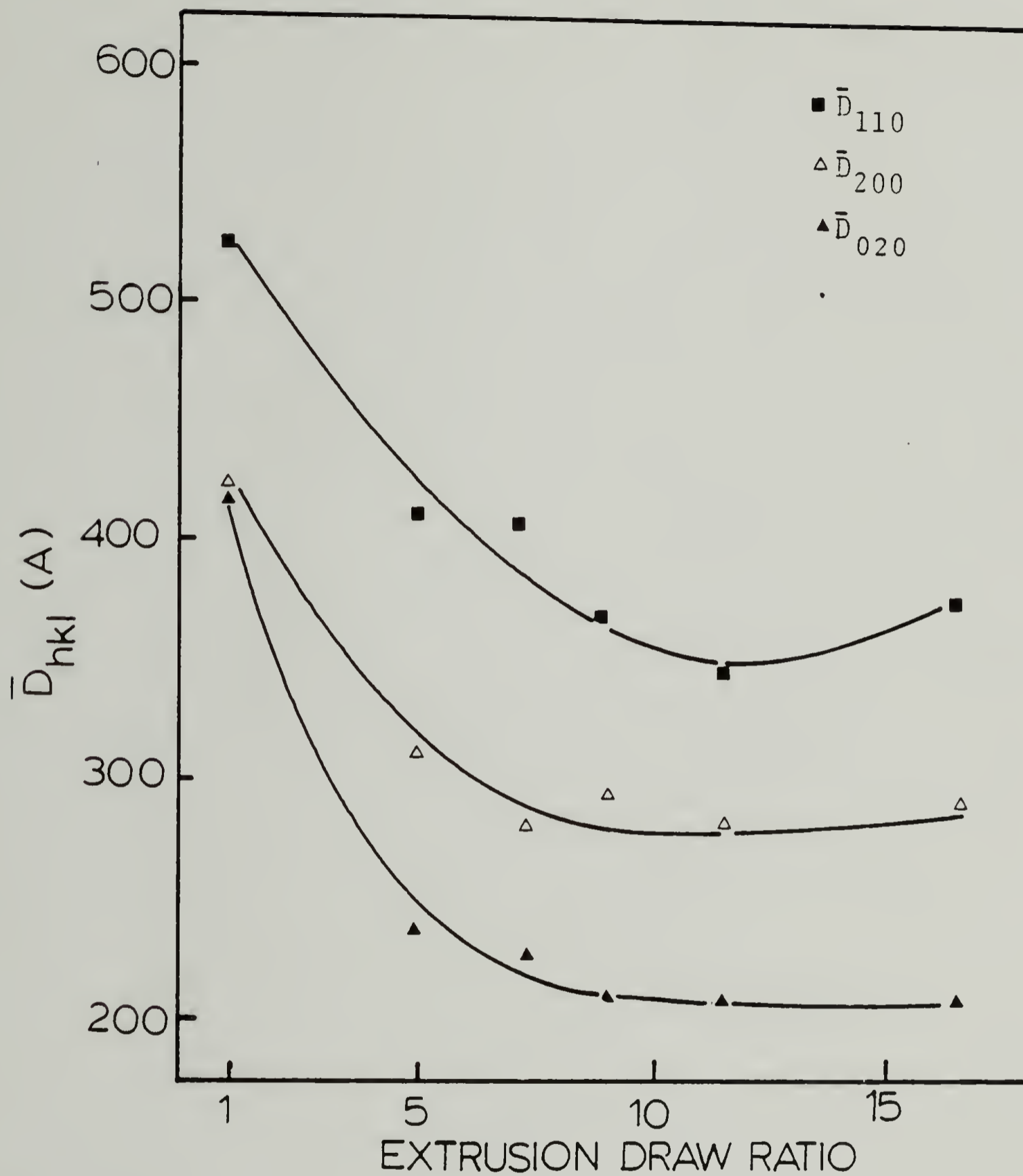


Figure 2.13. Change of crystallite size \bar{D} along the (110), (200) and (020) planes as a function of extrusion draw ratio for billet 1.

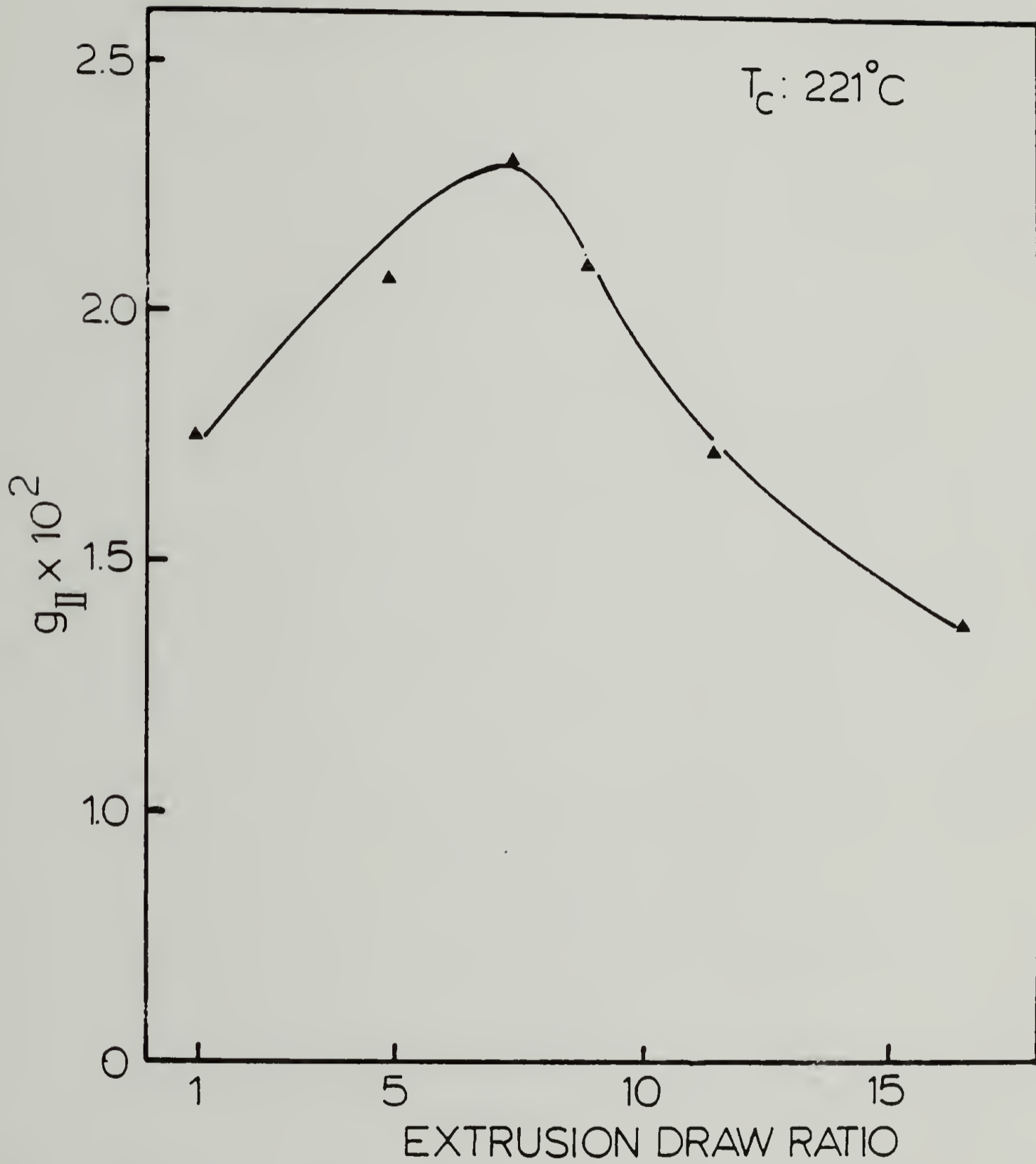


Figure 2.14. Change of distortion parameter, g_{II} , as a function of extrusion draw ratio for billet 1.

in which \bar{D}_{hkl} reaches the plateau.

2.3.6 Deformation Mechanism

Fig. 2.15 is the electron micrograph of a fracture surface replica of billet 1 drawn to EDR 4.9. It shows the co-existence of undrawn, partially drawn lamellae and fibrillar structure. This observation provides an additional clue to the plastic deformation mechanism. A now widely accepted mechanism for semi-crystalline polymers was proposed by Peterlin [26]. It consists of three deformation stages; involving the shear, rotation, chain tilt and slip in lamellae before neck, the transformation of lamellae into bundles of microfibrils and the sliding of microfibrils and fibrils past each other in the strain-hardening step. The deformation in solid-state extrusion is adequately described by this model with the neck in the die region and with substantial admixture of shear fracture of stacks of lamellae [94].

Chain-extended lamellae are extremely large and can be easily observed by electron microscopy showing the characteristic striations which run parallel to the c-axis direction. Thick lamellae of both selenium and CEPE had been reported to survive drawing with individual lamellae showing tilted chains embedded in a matrix of fibrils [43]. Due to the inhomogeneity in the deformation of bulk polymer and the low draw efficiency of highly

Figure 2.15. Transmission electron micrograph of fracture surface replica of billet 1 drawn 4.9X showing coexistence of undeformed, tilted, and partially drawn lamellae and generated fibrillar structure. Arrow indicates drawing direction.



chain-extended PE, even at EDR 4.9 (MDR 1.7), which would normally have exhibited a substantial fibrillar structure, features as in Fig. 2.15 could still be observed. The undrawn lamellae show c-axis perpendicular to the draw direction and can be seen to be the last to be drawn out, as had been observed in the deformation of PE spherulites [95], in which the polar zones where the c-axis is perpendicular to draw direction, survived deformation until higher elongation. Therefore, their survival at relatively low MDR can be observed. The tilted lamellae are distinguished as those surrounding the fibrillar structure with striations tilted towards the draw direction. The tilt angle, as measured from the angle between the striations and lamellar surface normal is $32-38^\circ$. Higher tilt angles are not observed and the transformation into fibrillar structure is discontinuous. Chain tilting as observed here must be distinguished from those observed in roof-shape PE crystals crystallized at high temperatures where the tilt angle varies from 18 to 46° corresponding to some simple, low index planes [98]. In the present case, the chains above and below the fibrillar structure in the deformation zone are observed to tilt and converge towards the draw direction.

In the study of drawn PE of low draw ratio, Peterlin and Meinel [97] showed, from the development of a four-point small-angle X-ray pattern and the splitting of

the (110) and (200) wide-angle X-ray diffractions, that the rotated lamellae also have chains tilted up to 48° . The rotation of the lamellae to 45° gives maximum plastic compliance for chain tilt and slip for its subsequent destruction. The observation in Fig. 2.15 shows discontinuous transformation of lamellae with tilted chains into a fibrillar structure and is consistent with Peterlin's model of plastic deformation.

2.4 Conclusion

Highly crystalline CEPE with a lamellar thickness comparable to the molecular chain length contains few trapped entanglements and interlamellar links to provide continuity and stress transfer for effective orientation during drawing. This is shown by the slow development on drawing of the crystal orientation functions. The efficiency of drawing increases with billets crystallized with higher undercoolings and increasing amorphous content as a result of increasing chain entanglements and interlamellar links. The efficiency reaches a maximum of 0.71 in solid-state extrusion. Tensile moduli are found to correlate linearly with MDR irrespective of morphology, draw temperature and technique. Crystallite sizes along the (110), (200) and (020) planes decrease sharply on

initial draw and level off at EDR 10. The Hosemann's distortion parameter increases initially to a maximum at EDR 7.5 and then decreases on further drawing. Electron micrographs of fracture surface replicas show the survival of lamellae at low drawing. Regions of undeformed, tilted and partially drawn lamellae are found to coexist with the newly generated fibrillar structure. This is consistent with Peterlin's model of plastic deformation.

C H A P T E R I I I

MELTING AND RECRYSTALLIZATION DURING DEFORMATION OF SEMI-CRYSTALLINE POLYMERS

3.1 Introduction

Several deformation mechanisms have been proposed to describe the morphological changes during drawing of semi-crystalline polymers. A widely accepted one, particularly suited for polyethylene, is that of Peterlin [26], which involves the shearing, rotation, chain tilt and slip in the lamellae and their transformation into bundles of microfibrils. For many years, it has been disputed whether the morphological changes on deformation involves melting and recrystallization.

Recent advances in drawing have produced PE of uniaxial draw ratio more than 10X its "natural draw" [98]. This was thought to be possible only if the local strain energy during deformation is high enough to melt the chains which could then be easily drawn to the high draw ratio and give the ultra-high modulus fibers [99].

This also explains the shrinkage behavior of drawn PE during annealing [100]. The cold drawn sample shrinks

much more than PE obtained by hot drawing. It has been rationalized that hot drawn PE contains crystalline bridges which are formed during deformation giving crystal continuity along the draw direction. They are relatively stable to annealing as opposed to the taut tie molecules of cold drawn PE, which relax during annealing and therefore shrinks much more.

The strongest and often-cited evidence for melting during deformation is the lamellae long period of the drawn PE fibers, measured from small-angle X-ray scattering (SAXS), depends on the draw temperature, irrespective of initial lamellar thickness [101]. At any particular draw temperature, such long period also has been found to be independent of draw ratio once the lamellae have been fully transformed into microfibrils. Indeed, the long period increases with draw temperature, in a way similar to its dependence on crystallization temperature [102]. Such comparable behavior suggests that the long period must be produced by the same process, i.e. through recrystallization. The above observations apply to both tensile and compressive deformations [101, 103].

A melting and crystallization process during deformation is also a consequence of the proposed random switch-board model of chain folding in lamellae [104]. In this model, entanglements are trapped in the fold loops and the lamellae are interconnected such that their

relative mobility is impeded during deformation. To transform them into the fibrillar structure of the drawn polymer, entanglements must be relieved through melting and recrystallize as folded chains in the fibrils.

Meinel and Peterlin [105] have calculated the conversion of deformation work into heat under adiabatic condition. They find that the rise in temperature is insufficient to cause crystal melting in PE. A similar conclusion was also reached by Vincent [11]. Deformation during solid-state extrusion used in this laboratory is so slow that heat transfer to surrounding environment is maintained such that the whole system is virtually isothermal.

Interest in this problem was revived when Juska and Harrison [99] proposed a deformation mechanism for PE which evokes melting at all draw temperatures in which the spherulitic lamellae are converted into microfibrils through isolated deformation zones of crazes and shear bands.

Subsequently, Wignall and Wu [106] cleverly used the anomalous molecular weight segregation effect in small-angle neutron scattering (SANS) of deuterated PE and hydrogenated PE blend to study this problem. They found a large reduction in SANS molecular weight when the samples were deformed between 50 and 119°C, which is similar to the phenomenon observed in melting and quenching and

therefore concluded the reorganization of morphology during deformation is similar to melting and recrystallization. However, work by Wu et al. [107] on poly(ethylene terephthalate) found the change in synchrotron SAXS patterns when deformed at room temperature does not indicate any melting and recrystallization.

The strongest experimental evidence of melting and recrystallization during deformation is the observed unique dependence of long period on draw temperature, yet in previous works this was evaluated only with initial lamellae <100 nm thick. It is thus proposed here to study this problem by deforming, using solid-state extrusion, a high pressure crystallized chain-extended PE which has lamellar thickness in the region of $10^2 \sim 10^3$ nm. Chain-extended PE can only be crystallized under high pressure, >350 MPa [47]. Should melting occur, recrystallization would result in folded chains since the extrusion pressure is not high enough to recrystallize into chain-extended lamellae. The periodicity of recrystallized folded chains along the draw direction could then be detected by SAXS.

3.2 Experimental

High density PE pellets (Du Pont Alathon 7050) with molecular weights, M_w 59,000 and M_n 19,000 were crystallized at constant pressure 460 MPa and at four crystallization temperatures of 221, 216, 207 and 198°C into chain-extended PE, as described in Section 2.2.1; and quenched from 160 C at a constant pressure of 160 MPa into chain-folded PE billets. Each was solid-state extruded at 100°C through a conical brass die with 20° entrance angle in an Instron capillary rheometer up to draw ratio 23.4. In addition, chain-extended PE billet crystallized at 216°C and the quenched chain-folded PE billet were also extruded at a constant draw ratio of 12.9 at constant temperatures from 70 to 125°C all at a plunger speed of 0.01 cm/min.

SAXS of the extrudates were measured using the Oak Ridge National Laboratory SAXS instrument at 5m working distance with Cu K_α radiation and a two dimensional detector. Intensity was corrected for detector sensitivity, sample absorption, background and dark current. The circular beam stop is 1 cm in diameter such that the detector intensity is cut off at $k=0.008 \text{ \AA}^{-1}$ ($k=4\pi \sin\theta/\lambda$). Maxima observed at this k is an artifact

of the beam stop. Long period is measured from the peak position of the intensity maxima and using the Bragg's equation. For undrawn samples, the intensities were Lorentz corrected.

Thermal analysis of the samples were measured using a Perkin-Elmer Differential Scanning Calorimeter DSC-II equipped with a thermal analysis data station. Indium was used for calibration. Heating rate was 2.5°C/min.

3.3 Results

Characterization of the four chain-extended PE billets prior to drawing are shown in Table 2.1. The number average lamellar thickness as measured from fracture surface replicas by electron microscopy decreases systematically from 480 nm to 270 nm with decreasing crystallization temperature 221 to 198°C respectively. Fig. 3.1(a) and (b) show SAXS of these two undrawn billets after Lorentz correction. No prominent maxima can be detected except a very weak shoulder at $k=0.02 \text{ \AA}^{-1}$. The fluctuation of intensity of this shoulder is within the error of measurement, however, repeated scans produced the same weak shoulder. Therefore, this is likely to be real and not from statistical fluctuation of intensity. The quenched chain-folded billet shows two orders of strong

maxima, Fig. 3.3(a), with a long period of 33.7 nm.

The first set of experiments were carried out by extrusion drawing of both the chain-extended and chain-folded polyethylene billets at a constant temperature of 100°C to varying draw ratio. On deformation, all four chain-extended PE billets show two-point meridional scattering with weak intensity maxima, Fig. 3.2. The long period decreases with draw to a constant value of ~24 nm (Table 3.1). However, the quenched chain-folded polyethylene shows a contrasting type of scattering with strong intensity maxima, Fig. 3.2(b). The long period also decreases to ~23 nm, close to those found in extruded chain-extended PE and to values previously reported at the same draw temperature by both tensile and compression drawing [101, 103].

The second set of draw experiments were carried out by extruding the chain-extended PE billet crystallized at 216°C and the quenched chain-folded polyethylene sample to a constant draw ratio of 12.9 at a series of constant temperature from 70 to 125°C. At this draw ratio, lamellae of the initial spherulitic texture have been fully transformed into the fibrillar morphology. The draw temperatures cover both "cold" and "hot" (temperature above the α_c transition) drawing.

SAXS shows weak meridional maxima after the chain-extended PE has been extruded: Their intensity

decreases to a small hump as the draw temperature was increased, Fig. 3.3(a) and (b). The long period increases from 17.1 nm to 30.1 nm when the extrusion temperature is increased from 70 to 125°C respectively, Fig. 3.4. When the extrusion temperature is increased, the iso-intensity contour plots, Fig. 3.5(a) to (c), change from a well defined two-point meridional scattering to a near circular isotropic scattering pattern at 125°C. Thus indicates significantly poorer orientation at the higher draw temperature. However, an intensity scan along the meridian still shows weak maxima.

DSC scans of the undrawn and drawn chain-extended PE billet crystallized at 216°C are shown in Fig. 3.6. The undrawn chain-extended PE has a small endotherm, about 4% of the total peak area, at 130.5°C. This low temperature endotherm has been attributed to the low molecular weight fraction rejected during high pressure crystallization [55], and are able to crystallize into either fully extended or chain folded lamellae during cooling. The presence of this small endotherm is interesting, and even crucial to the conclusions of this study. The rejected low molecular weight fraction, when crystallized even into fully extended form, gives a lamellae thickness of <100 nm. The shoulder observed in SAXS has a long period corresponding to 35 nm. Thus falls within the thickness expected from the rejected low molecular weight fraction.

Table 3.1

Long Period of Chain-Extended and Chain-Folded
Polyethylene Billets Extruded at 100°C

Long Period (nm) from Extrudates of Chain-Extended
Polyethylene Billets:

Draw Ratio	Billet Number:			
	1	2	3	4
4.1	-	29.4	31.3	30.1
4.9	22.3	-	-	-
7.2	22.3	29.3	30.6	27.7
9.0	23.3	30.1	26.3	-
11.4	25.7	24.4	25.7	27.0
16.4	24.5	23.8	25.1	25.0
23.4	-	-	-	22.4

Long Period (nm) from Extrudates of Chain-Folded
Polyethylene Billet:

Draw Ratio	Long Period
Undrawn*	33.7
5.8	31.1
9.1	25.7
12.2	23.4
14.8	27.0
16.2	21.4

* Lorentz correction necessary

Figure 3.1. SAXS of undrawn CEPE crystallized at (a) 221°C and (b) 198°C.

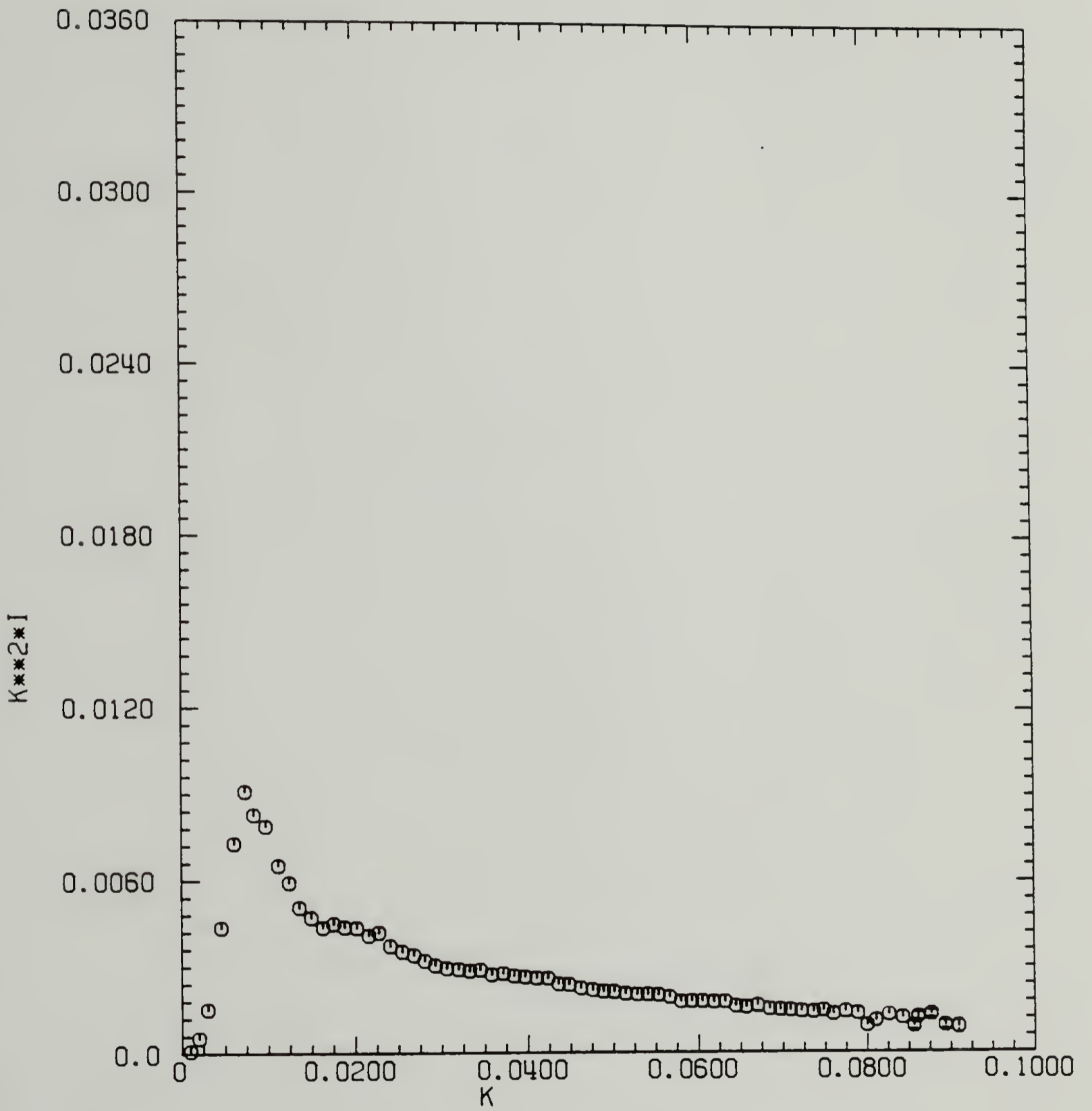


Figure 3.1 (a)

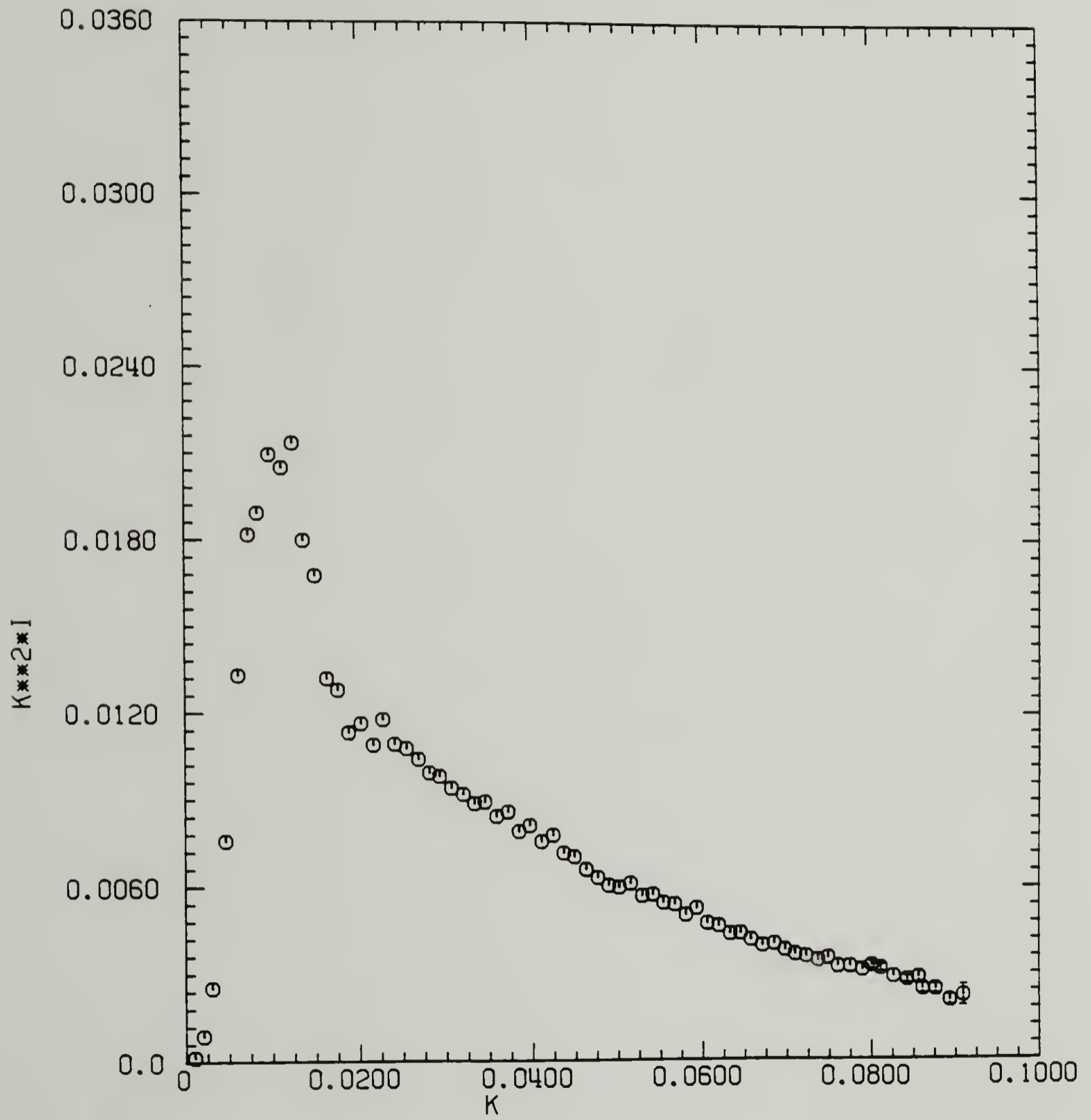


Figure 3.1(b)

Figure 3.2. Meridional SAXS scans of CEPE
billet 2 extruded at 100°C to draw ratios (a)
4.1 and (b) 16.4.

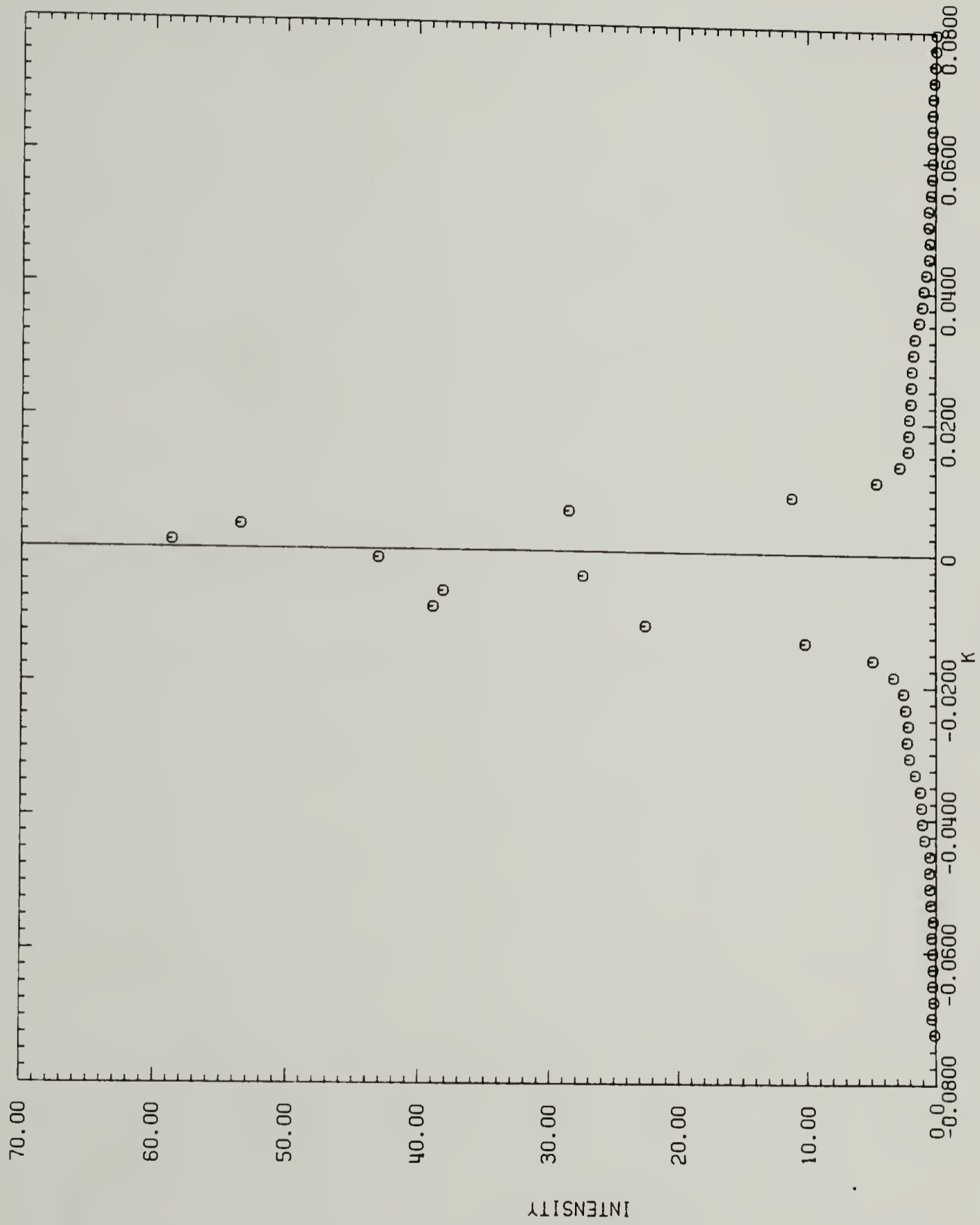


Figure 3.2 (a)

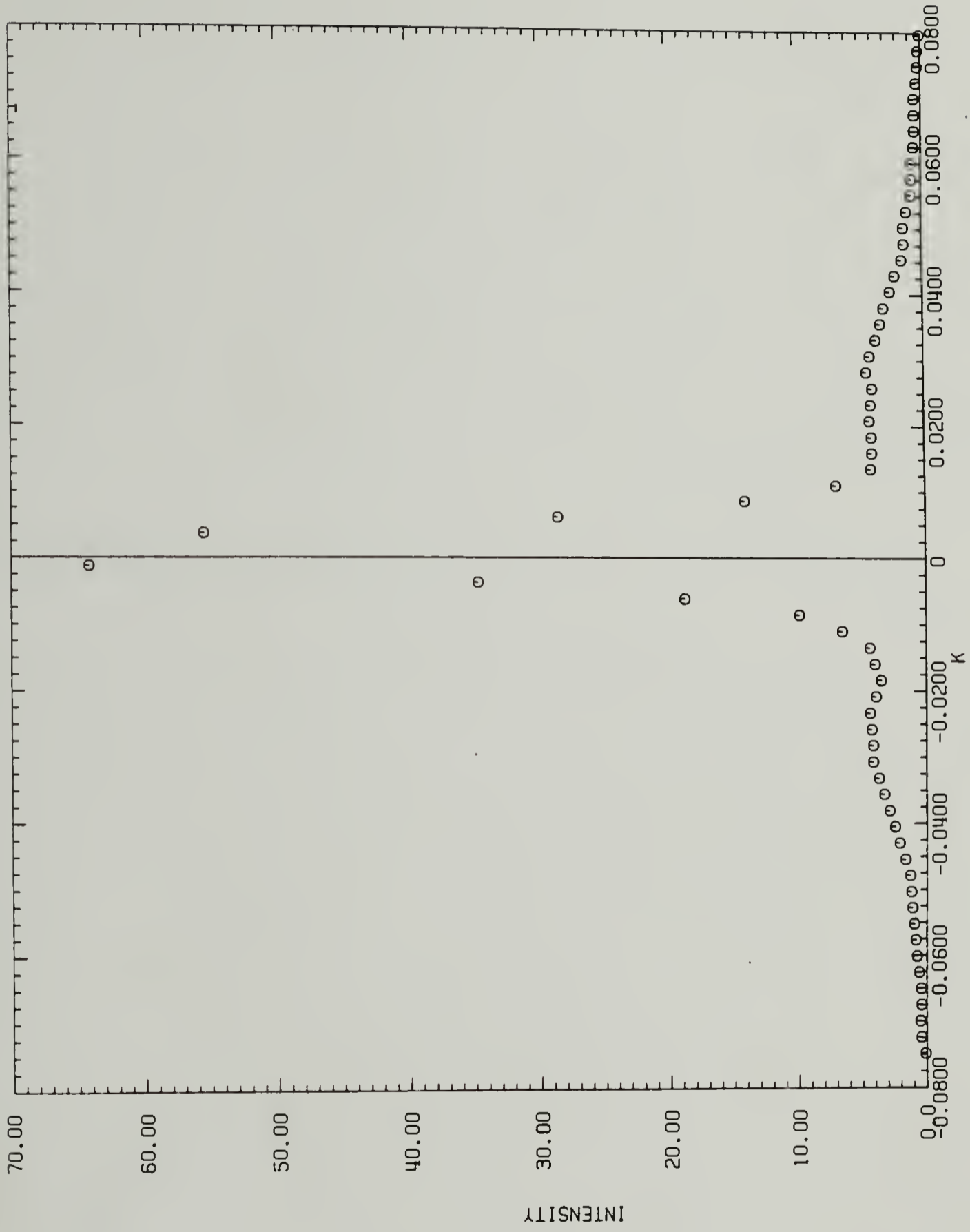


Figure 3.2 (b)

Figure 3.3. SAXS scans of (a) undrawn CFPE and (b) at draw ratio 12.2, extruded at 100°C.

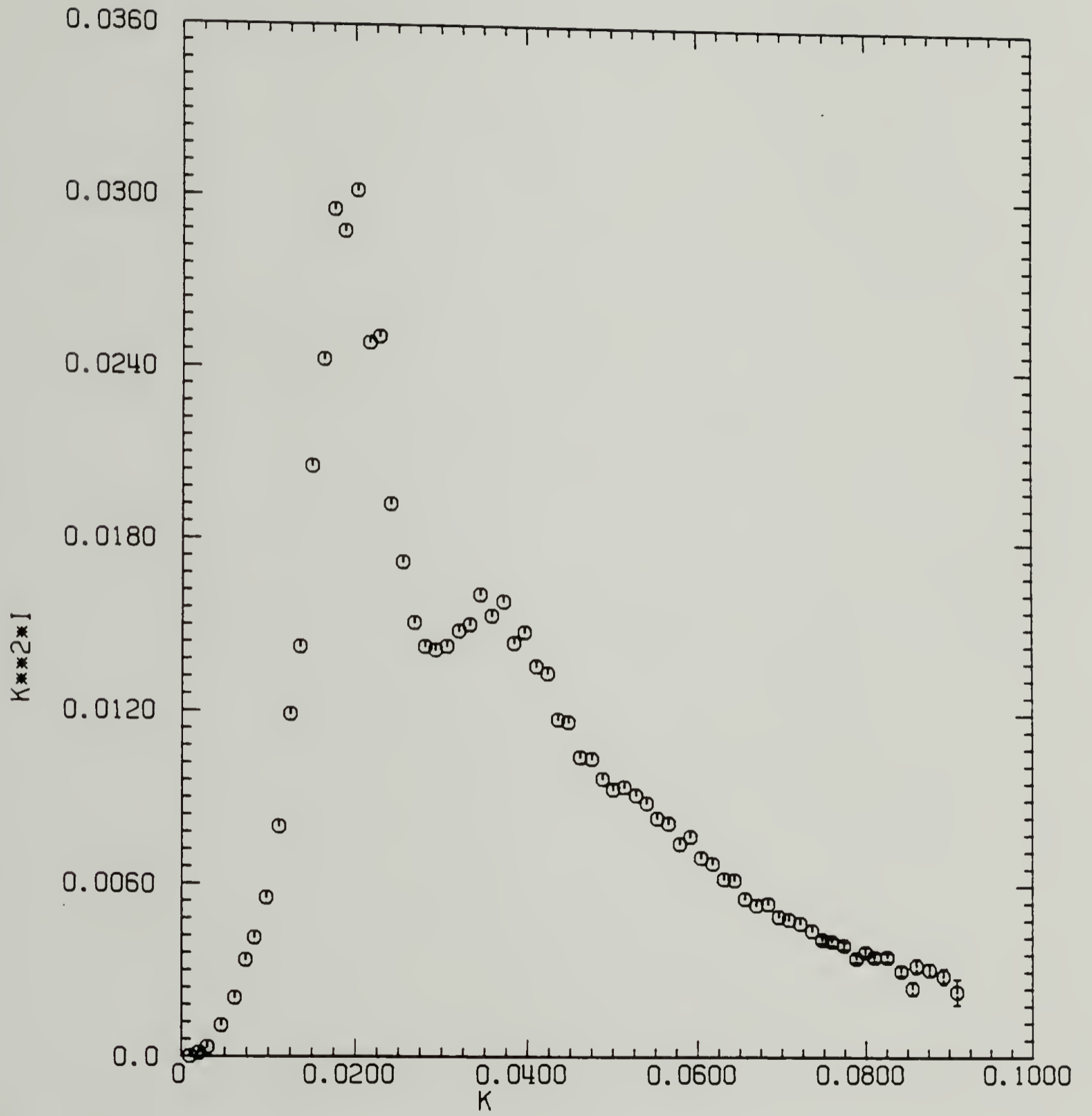


Figure 3.3 (a)

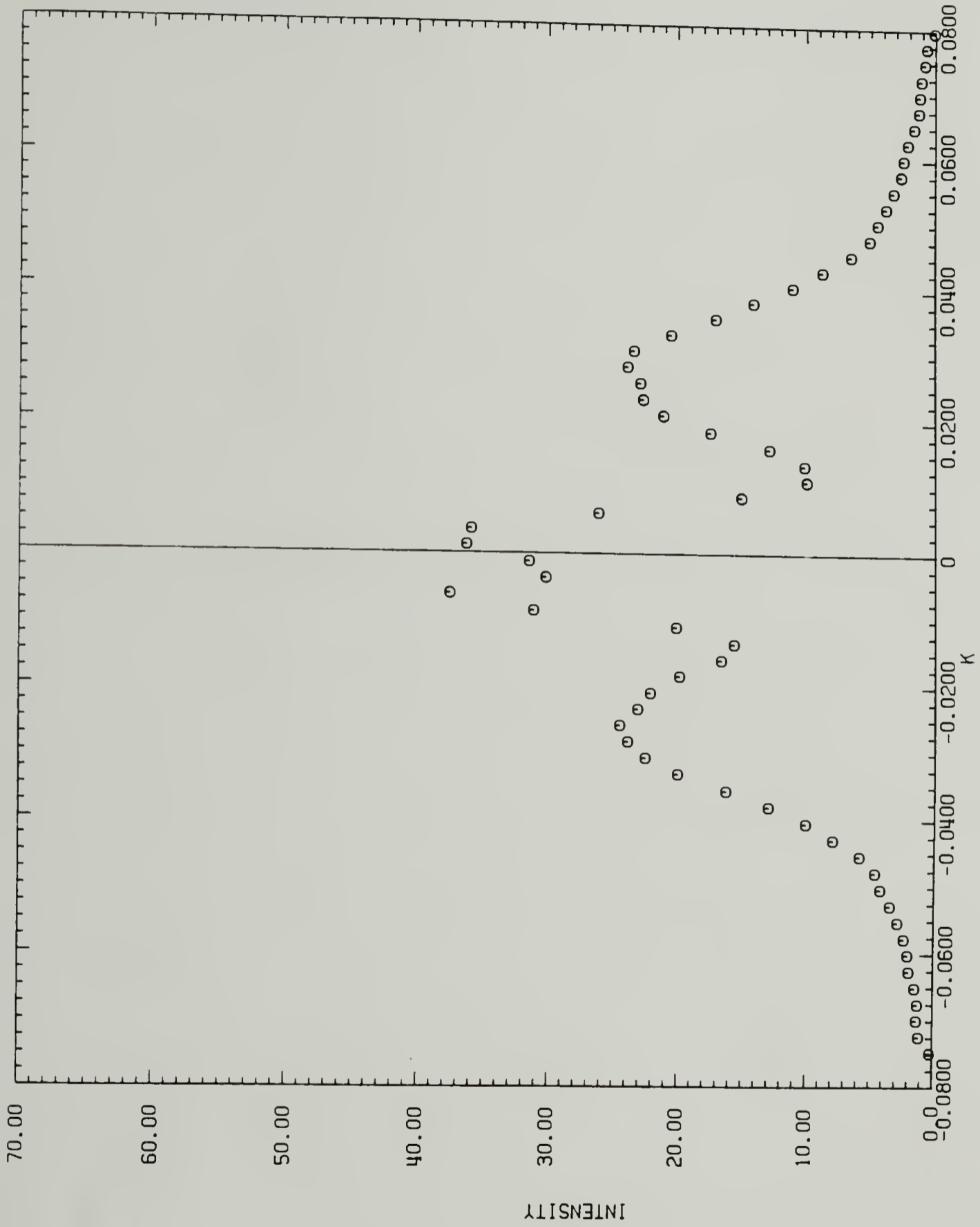


Figure 3.3 (b)

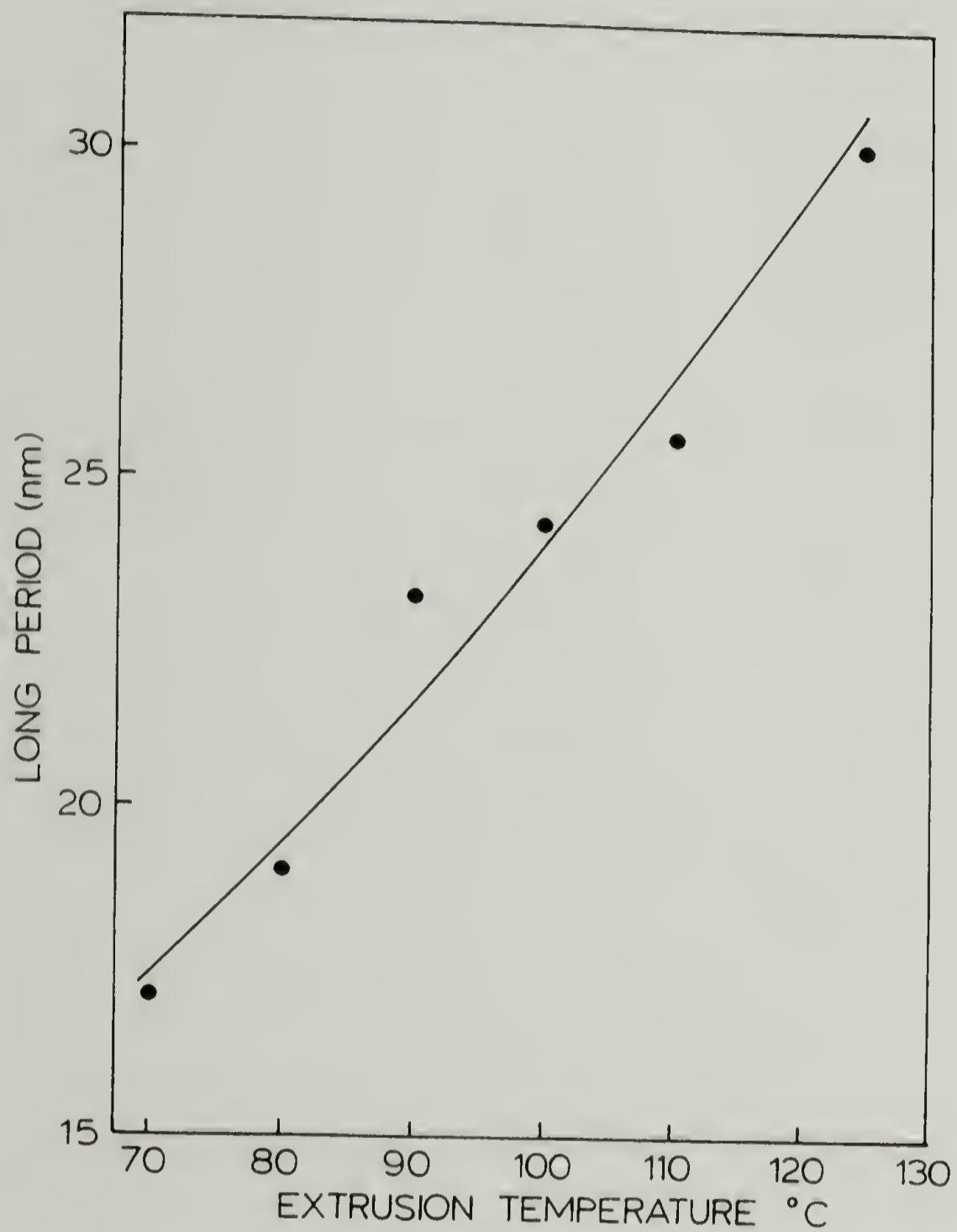
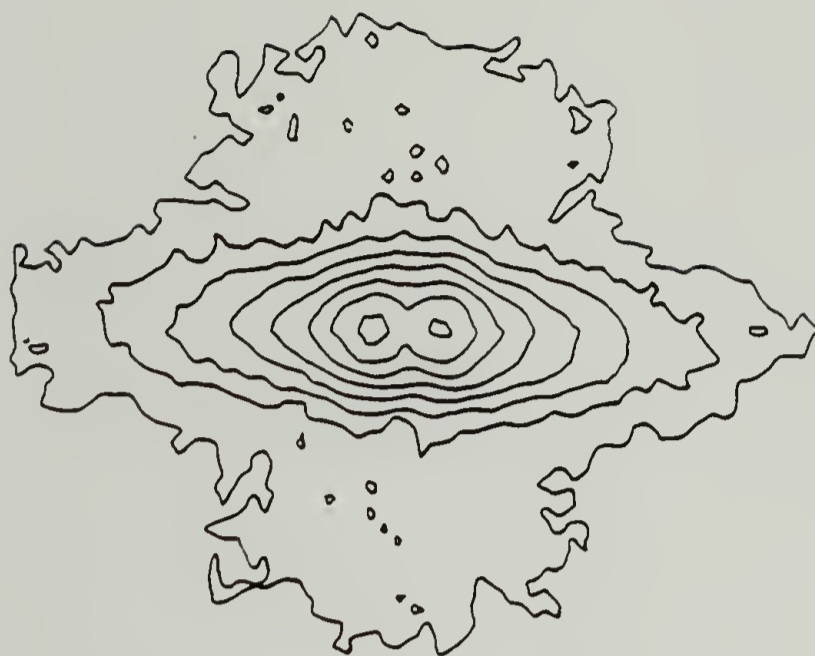
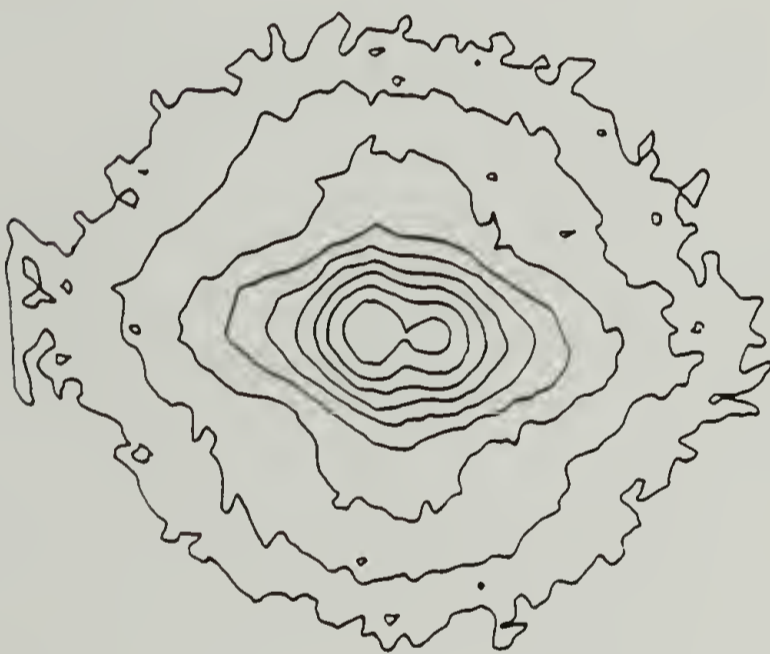


Figure 3.4. Long period of CEPE billet 2 extruded at increasing temperature to constant draw ratio of 12.9.

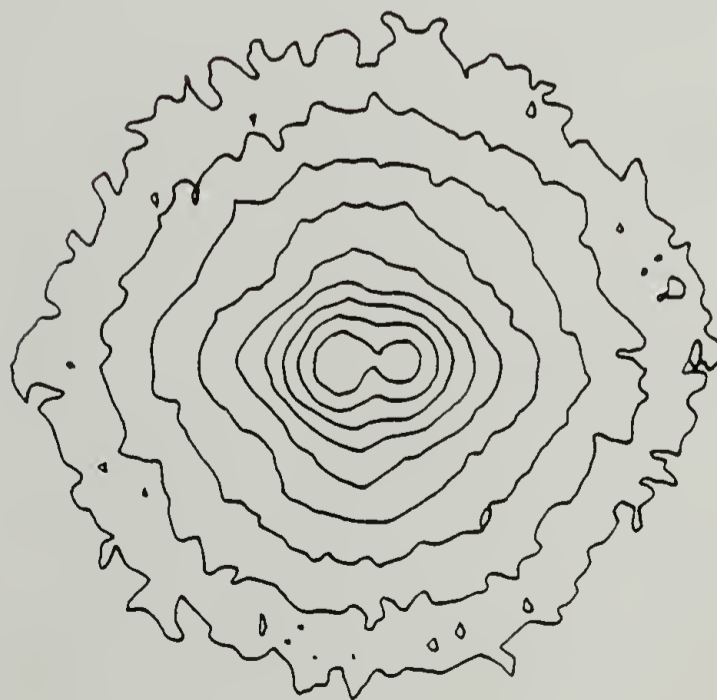
Figure 3.5. SAXS isointensity scattering patterns of CEPE billet 2 extruded to constant draw ratio of 12.9 at (a) 70, (b) 100 and (c) 125°C.



(a)

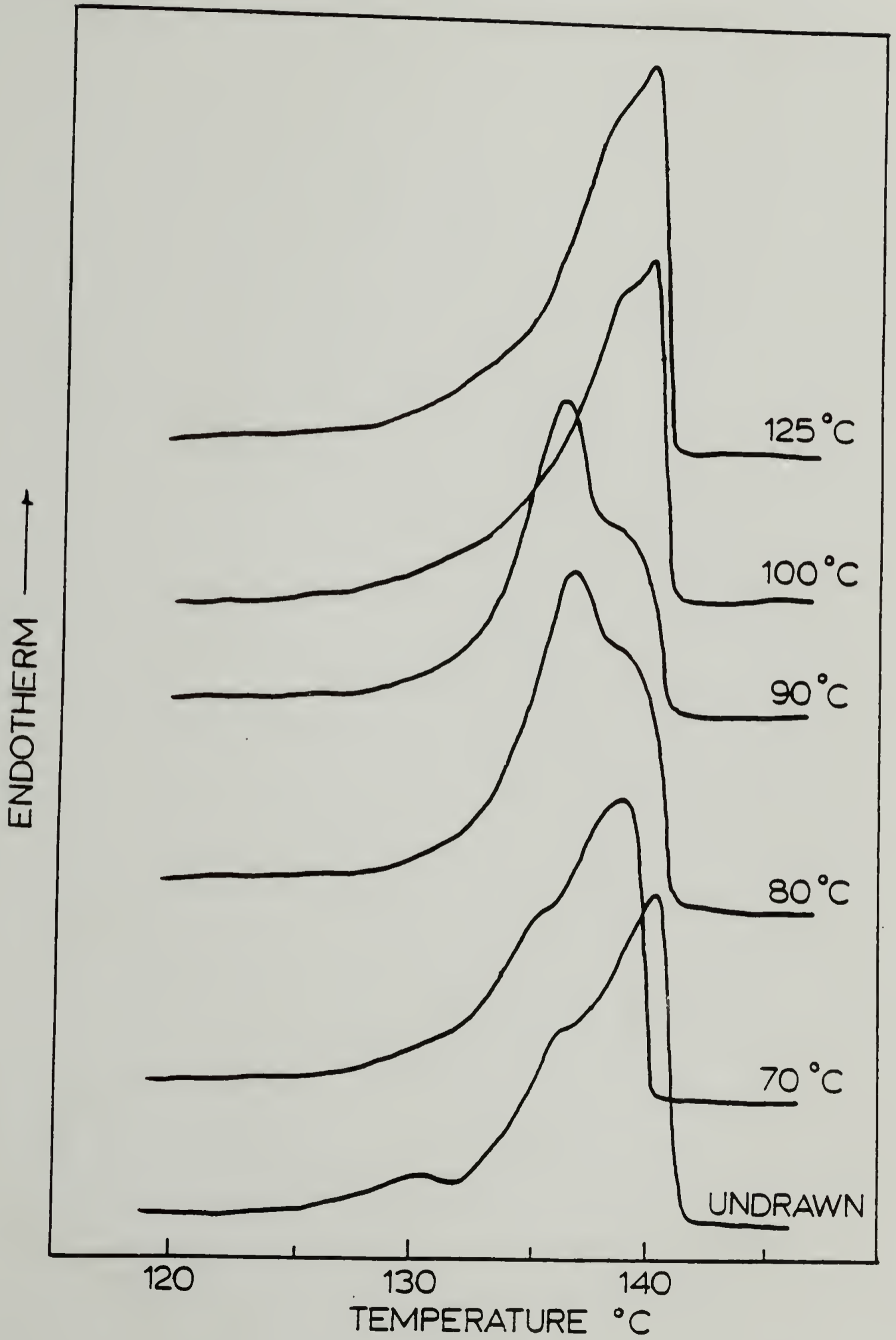


(b)



(c)

Figure 3.6. DSC scans of undrawn CEPE billet extruded at increasing draw temperature.



On drawing, this low temperature endotherm disappears, merging with the higher temperature endotherm,, Fig. 3.6. The highest endotherm, with peak melting point of 141°C , also decreases both in temperature and magnitude as extrusion temperature is increased, while the 136°C shoulder increases in magnitude and becomes dominant at a draw temperature of 90°C . At higher draw temperature, $>100^{\circ}\text{C}$, a single endotherm is observed with peak maximum at 139°C .

3.4 Discussion

SAXS results of chain-extended PE extrusion drawn at 100°C with increasing draw ratio display weak intensity maxima along the meridian. The corresponding long period at high draw reaches a plateau of ~ 23 nm irrespective of the initial lamellar thickness. When extruded to a constant draw ratio, with increasing draw temperature, the long period increases with draw temperature. These observations are consistent with the often cited evidence by advocates of melting and recrystallization during deformation. However, this deduction is not as straight forward as it appears in light of thermal analyses and consideration of the scattering patterns.

The total integrated intensity of SAXS over the whole

angular range is the invariant, Q , defined by

$$Q = \int_0^{\infty} I(s) s^2 ds \quad (3.1)$$

for an isotropic system. $I(s)$ is the measured scattered intensity, s is the scattering vector. For an anisotropic system with cylindrical symmetry about the fiber direction, s_1 ,

$$Q = \int_0^{\infty} \int_0^{\infty} I(s_1, s_2) s_1 ds_1 ds_2 \quad (3.2)$$

For a two phase system, Q is proportional to the mean squared electron density difference, $\langle (\rho - \bar{\rho})^2 \rangle$, between the amorphous and crystalline phase.

$$\begin{aligned} \langle (\rho - \bar{\rho})^2 \rangle &= (\rho_1 - \rho_2)^2 \phi_1 \phi_2 \\ &= \frac{4\pi Q}{i_e N^2 d a \lambda^3 P_0} \end{aligned} \quad (3.3)$$

where a = sample to detector distance

i_e = electron scattering cross-section

N = Avogadro's number

d = sample thickness

P_0 = primary beam intensity

and ρ_1 and ρ_2 are electron densities of each phase with sharp boundary and ϕ_1 and ϕ_2 are their respective volume fractions.

Thus the change of electron density difference on deformation can be obtained from experimental evaluation

of the invariant which requires accurate measurement of the scattered intensities at both very small and very large angle. It has been found that in solid-state extruded PE [108, 109], the electron density difference between crystalline and amorphous phases becomes smaller as draw ratio and orientation increases resulting in diminished intensity. The overall scattering patterns, Fig. 3.5, and wide-angle X-ray photographs, show at higher draw temperature, orientation of the extruded chain-extended PE is poorer due to greater relaxation and/or less efficient orientation. Therefore, it is unlikely that $(\rho_1 - \rho_2)$ decreases in this case. Then the decrease in SAXS intensity is due to a decrease in the fraction that gives scattering intensity maxima.

SAXS and DSC of the undrawn billet show even in chain-extended PE, that there is a small fraction of low molecular weight PE rejected during crystallization, characterized by a weak shoulder in SAXS and a long period of ~ 33 nm. The observed SAXS maxima of extruded chain-extended PE is so weak that the scattering fraction must be very small and likely originates from the fraction of rejected crystals.

The chain-extended PE crystals do not melt and recrystallize during deformation in the present study. Comparing the SAXS of drawn chain-extended PE with that of chain-folded PE, the former exhibits weak intensity

maxima. Should melting have occurred, the drawn chain-extended PE would have recrystallized into a chain-folded lamellae because the extrusion pressure was <180 MPa which is insufficient for recrystallization into the chain-extended morphology. Then the observed intensity maxima would be in the same order as that of the chain-folded PE extruded under the same conditions.

There are two possible reasons why chain-extended crystals apparently do not melt during deformation: first, chain-extended PE crystals have slightly higher melting point of 141°C. However, the difference between melting points of chain-extended and chain-folded PE are not that large to expect an entirely different drawing behavior.

A more likely reason is chain-extended lamellae have thickness in the same order as the molecular chain length and therefore have few folds per chain and consequently reduced entanglements. The deformation of such thick lamellae with reduced entanglements can be different from the chain-folded lamellae which are profusely interconnected. Disruption of the thick lamellae still occurs during deformation as shown by a shift in the highest endotherm to lower temperature and a decrease in magnitude. However, chains are easily unravelled when the draw temperature is high, above the crystal dispersion temperature, the interchain dispersive force is drastically reduced. Slipping of chains can occur in

crystallographic planes which contain the chain direction when the applied stress reaches the critical resolved shear stress. The slipped chains can incorporate into the drawn microfibrils without the necessity of melting. It is therefore concluded that deformation of chain-extended PE with high chain extension does not involve melting and recrystallization.

3.5 Conclusion

SAXS of solid-state extrusion drawn chain-extended PE shows weak intensity maxima along the meridian. The long period increases with increasing draw temperature. When drawn at 100°C, all four chain-extended PE billets with varying initial lamellar thickness, showed a constant periodicity of ~24 nm at high draw, comparable to the long period obtained in chain-folded PE extruded under similar conditions. From thermal analyses and consideration of the overall X-ray scattering patterns, the observed weak long period originates from the small fraction of low molecular weight PE rejected during high pressure crystallization. The chain-extended lamellae do not melt and recrystallize during the draw conditions thought to be critical for the evaluation of melting and recrystallization process during deformation. Crystallographic slip is the dominant mechanism.

C H A P T E R I V

CRYSTAL STRUCTURES OF NYLON 6

4.1 Background

Nylon 6 is polymorphic, existing in several crystal forms. More than a dozen crystal structures have appeared in the literature, each being named with a greek letter prefix. Certain structures, though being called differently, do not appear to have significantly different crystallographic data. On the other hand, some with the same name have structures belonging to different crystal classes. There are also proposed structures that have been shown to be unacceptable. Thus the state of Nylon 6 crystal structures can be very confusing. This chapter reviews the literature and discusses which structures are more generally accepted by researchers in Nylon 6. A clear picture of the crystal structures is important in the understanding of the structure-property relationship in the drawing of Nylon 6 in the following 2 chapters, 5 and 6.

Nylon 6 is polymerized from ϵ -caprolactam and has $\text{-(CH}_2\text{)}_5\text{NHCO-}_n$ as its monomer unit. The polar carbonyl

groups form hydrogen bonds with neighboring chain imino hydrogen atoms. Infrared (IR) study had shown that more than 99% of the monomer units in the crystalline region formed hydrogen bonds [110]. Therefore arrangement of the Nylon 6 chains in the crystal must maximize hydrogen bonding. Fig. 4.1(a) shows the arrangement of parallel Nylon 6 chains in a planar ziz-zag conformation; only 50% of the monomer units can form hydrogen bondings between neighboring chains. To get 100% hydrogen bond formation, the amide groups must be twisted out of its plane and give an overall pleated arrangement. This is one of the structures proposed for a γ -Nylon 6. Alternatively, full hydrogen bond between the planar ziz-zag chains can be formed if the adjacent chains are arranged antiparallel as in Fig. 4.1(b). This antiparallel arrangement is found in the structure of the α -Nylon 6 and was proposed [111] before the idea of chain folding in polymer crystals. Now it can be visualized, if the Nylon 6 chains of the lamellae fold back, maximum hydrogen bonding can be formed between antiparallel chains.

Crystal structure determination is usually done with X-ray diffraction. To give a complete description of the structure, the following information is required:

1. Unit cell parameters with the reflections indexed, number of chemical units/cell and the calculated crystal density.

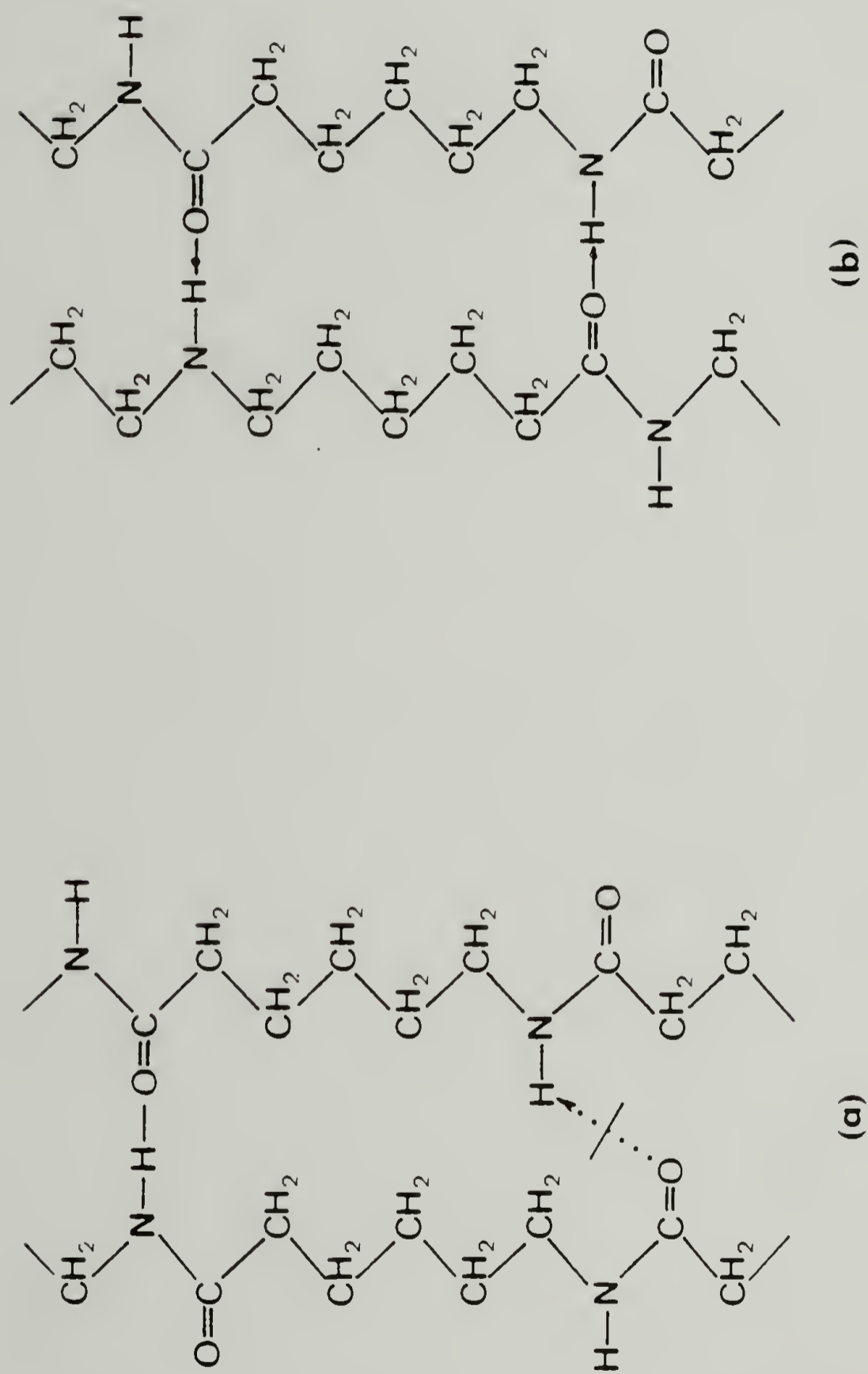


Figure 4.1. Nylon 6 chains arranged in (a) parallel and (b) antiparallel. Arrow indicates hydrogen bond.

2. Assignment of space group.
3. Atomic arrangement within the unit cell.
4. Structure factor calculation, refinement and comparison with experimental intensities.

Spectroscopic tools are often used to supplement the information. However, not all crystal structure determination are thorough because polymers usually show few reflections. It is therefore necessary to evaluate reliability.

Brill [112] was the first to determine the crystal structure of Nylon 6 to be monoclinic. A later triclinic structure given by Kordes et al. [113] was not really different since it could be reduced to the monoclinic cell of Brill with similar unit cell parameters. More precise determination was later done by Wallner [114], and Holmes, Bunn, and Smith [111] who proposed a monoclinic Nylon 6 crystal with the chains arranged antiparallel. Holmes et al. recognized from the appearance of extra reflections from some samples that there are alternate ways of packing the chains and called this secondary structure " β " to differentiate it from the α -structure they reported. Their determination of the α -structure was not only precise but complete. There is no argument on the acceptance of their crystallographic data of the α -structure. The confusion lies in the γ -structure and the several alternate structures which have been

proposed.

Table 4.1 tabulates the crystallographic data of all the proposed structures. The unit cell axes listed have been transformed so that they have the b-axis as the chain axis and interaxial angle, β , as usually given for a monoclinic cell. This is necessary to avoid confusion as to which is the chain axis. It must be noted that in rhombohedral, hexagonal or orthorhombic cells, the chain axis is the c-axis by convention. This is sacrificed here for ease of comparison. To make the discussion of the secondary structures easier, they are divided into two sections according to their annealing behavior and the process by which they are obtained: i.e. from melt processing or from crystal transformation by chemical method.

4.2 Mesomorphic Structure from Melt Spinning

Ziabicki [115] found when Nylon 6 was spun rapidly from a melt into a dry atmosphere, a new structure was obtained. This structure was unstable and transformed into the α -structure when exposed to moisture or on annealing. It was found to have a rather imperfect hexagonal packing with the chains set randomly in the hexagonal plane like in a mesophase and was called

Table 4.1
Summary of Crystal Structures of Nylon 6 Reported in Literature

Crystal System	Lattice Constants a (nm) b (nm) c (nm)	β	Space Group	Crystal Density g/cm ³	Number of Chains/Ce11	References
monoclinic	.966 1.72 .832	65	-	-	-	Bri11 (112)
monoclinic	.945 1.708 .802	68	-	-	4	Wallner (114)
α - monoclinic	.956 1.724 .801	67.5	P2 ₁	1.23	4	Holmes et al. (111)
triclinic*	.984 1.70 .808	66.4	-	-	-	Kordes et al. (113)
β - hexagonal	.48 .86 .48	60	-	1.10	1	Ziabicki (115)
β - hexagonal	.485 .84 .485	60	-	1.099	-	Avramora et al. (115)
α - paracrysta- lline monoclinic	- - -	62-67	-	-	-	Roldan et al. (118)
α -pleated monoclinic	.956 1.688 .956	121	P2 ₁ /n	1.137	4	Stepaniak et al. (120)
γ - rhombohedral	.479 1.67 .479	60	-	1.13	1	Vogelsong (124)
γ - monoclinic	.933 1.688 .478	121	P2 ₁ /a	1.17	2	Arimoto (125)
γ - monoclinic	.962 1.66 .935	60	P2 ₁ /a	-	2	Ota et al. (126)
γ - monoclinic	.914 1.668 .484	121	-	1.188	2	I11ers et al. (119)
γ - orthorhombic	.483 1.668 .783	90	-	1.191	2	
γ - orthorhombic	.482 1.670 .782	90	-	-	-	Bradbury et al. (126)

* $\alpha=90^\circ$, $\gamma=77.4^\circ$

β -form. Avramora and Fakirov [116] recently used reflection high energy electron diffraction to support the presence of this mesophase structure, however, they found a shorter fiber identity period of 0.84 nm. It was claimed with this method, structure from a very small area of the sample can be determined without the complication of the presence of other crystal forms as in a bulk sample structure determination by X-ray. Hexagonal packing was also suggested by Reichle and Pretzche [117], although called the γ -form it was no different from the β -form already suggested by Holmes et al.

Roldan and Kaufman [118] attempted to classify Nylon 6 structures into groups according to order and stability; from amorphous to the stable α -crystal. In addition to the α -crystals, there are three more groups: viz. a stable γ -hexagonal structure, an unstable β -crystal with structure similar to a nematic liquid crystal and an α -paracrystalline structure with varying unit cell. There were no exact data given for this last group. However, the idea of a paracrystalline structure is not to be dismissed and will be discussed later. The above structures, except that of Avramora and Fakirov, have a fiber identity period >1.700 nm, but not as extended as the α -crystal of Holmes et al. of 1.724 nm. From standard bond angles and bond lengths, a fully extended Nylon 6 chain with two monomer units is 1.74 nm.

Therefore, even the stable α -structure has its amide groups slightly twisted. To differentiate these hexagonal structures with >1.7 nm fiber period from those obtained by KI_3 solution treatment which has shorter fiber period of <1.7 nm, Illers et al. [119] called them γ^* .

More recently, Stepaniak et al [120] reexamined this γ^* -crystal and found it to be the same as the β -structure of Ziabicki. However, they proposed a new monoclinic cell, called α -pleated crystal, with hydrogen bonding between antiparallel chains similar to the α -structure. This is radically different from what was proposed before, which had hydrogen bonds between parallel chains. The reason for the antiparallel chain bonds is attributed to the observed annealing behavior, in which this structure can be converted to the α -structure without the breaking of hydrogen bonds as would be required in the case of the γ -structure obtained from KI_3 solution treatment and therefore more stable in annealing. The hydrogen bond sheet distance is expanded to 0.956 nm and pleated in such a way to account for the shortening of the chain.

4.3 γ -Structure from Iodine Treatment

When Kinoshita [121] investigated the structure of an

extensive series of polyamides, it was concluded that Nylons formed from the ω -amino acids have two basic types of structure: either with extended zig-zag chains or with twisted amide groups causing the shortening of the chain. These two forms are the α - and γ -crystals. It was first reported by Ueda and Kimura [122] when the α -structure was treated with KI_3 solution and washed with sodium thiosulfate, a γ -structure was obtained. This structure cannot be converted into the α -form by annealing but does so on deformation [123]. Because of this different annealing behavior, it was distinguished from the γ^* -crystal by Illers. Several papers were published to determine if it is different from the previously found or β -structures obtained from spinning.

Vogelsong [124] determined it to be hexagonal with hydrogen bond alternates between (100) and (010) planes. Each chain is thus bonded to four neighbors with a three dimensional network type of structure. This structure has one chain per unit cell and the amide plane tilted to give shortening of the chain axis. This model was contested by Arimoto et al. [125] who made detailed structure determination by X-ray aided by IR studies. Essentially, their unit cell data are nearly the same (Table 4.1) but with different molecular chain packing. In the γ -structure of Arimoto, the hydrogen bond is in the (100) plane. Each chain is bonded to two neighbors of parallel

chains and the amide group twisted out-of-plane giving a pleated hydrogen bond sheet structure. This structure has two chains per unit cell because the hydrogen bonded sheets alternate with antiparallel chains. Evidence for this is the presence of the $(1k\bar{1})$ reflections and confirmation from the IR study of Bradbury and Elliot [127] who however proposed the unit cell to be orthorhombic with a random variation of the chain sense from sheet to sheet as opposed to the (100) plane of Arimoto, as observed by the presence of a layer line streak. However, there is no difference between these two unit cells, one can be translated to another and symmetry considerations claimed by Arimoto favored the monoclinic cell.

The above structures are sometimes called pseudo-hexagonal by some researchers because the interaxial angle, β , is almost 60° , but the structure has monoclinic symmetry, so the term pseudo-hexagonal should be avoided.

4.3 Conclusion

Even though there is confusion on the secondary structure of Nylon 6, Parker and Lindenmeyer [129] after carefully comparing them, concluded that there are at least two basically different structures as was suggested

by Kinoshita. A fully extended chain of the α -structure and the pleated chain structure which can be further divided according to their annealing behavior: the mesomorphic β -structure of Ziabicki and the γ -structure obtained from the α -crystals by treatment with KI_3 solution. In the present author's opinion, this subdivision is not necessary.

Polymer crystals obtained are usually imperfect compared to small ionic crystals. Consider the process by which these secondary structures are obtained: the rapid quenching from high speed spinning does not allow perfect crystals to be formed. The Nylon 6 chains are "frozen-in" during spinning giving the rather imperfect mesomorphic β -structure. However, the γ -crystals obtained by KI_3 solution treatment are from the more stable, well formed α -crystals. Even though hydrogen bonds are broken in the intermediate complex and there is some chain mobility to allow hydrogen bonds to reform between antiparallel chains. Such chain mobility is never of large scale as compared to that of melt spinning. Therefore the γ -structure generated is dictated by its precursor α -crystals. The more perfect is the precursor crystals, the more stable is the generated γ -crystals towards annealing. If a rapidly spun fiber with the mesomorphic β -structure were to be treated with KI_3 solution, what would be the generated structure?

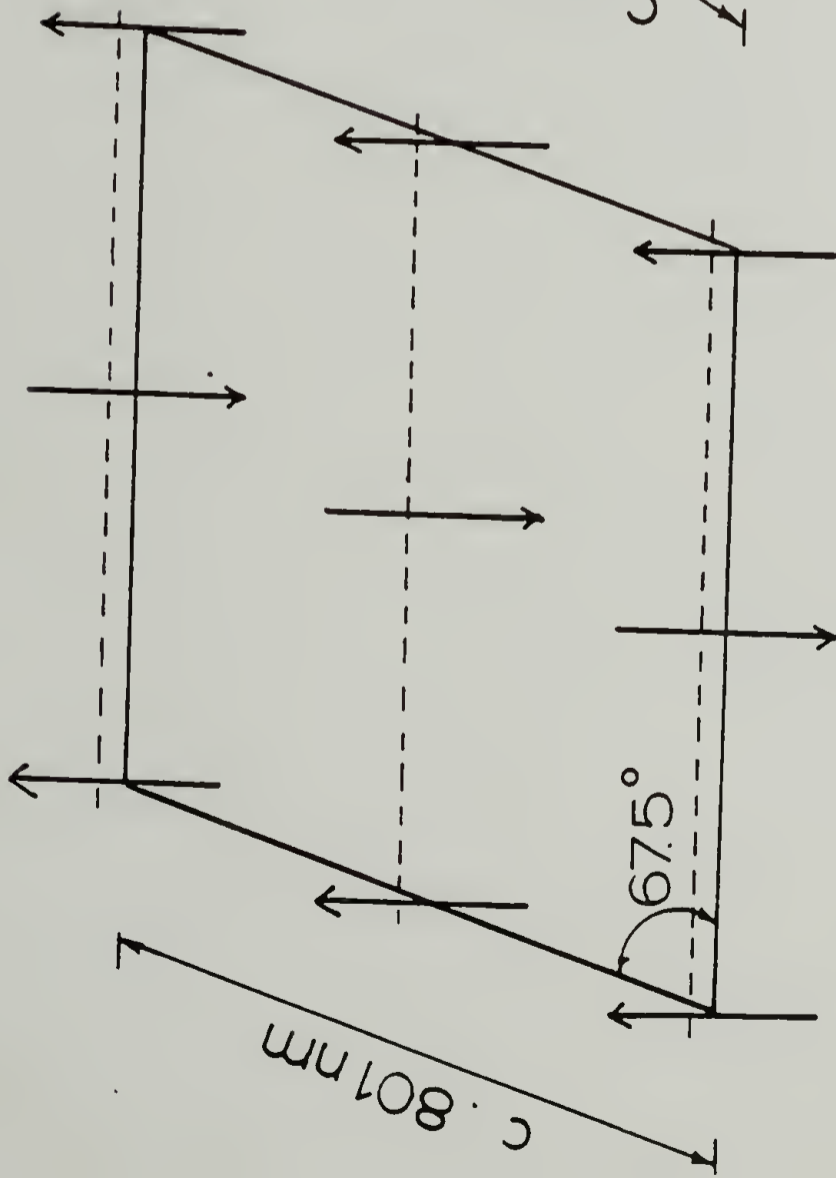
Although we are not aware of such a study, a prediction is that a γ -structure would be obtained since complexing with the polar iodine is determined by the ability to compete for hydrogen bond formation rather than the starting structure. The γ -structure obtained would have poor stability in annealing because of the poorly developed structure of the precursor.

Thus to distinguish the secondary structure into β - and γ - is not necessary. One can introduce the Hosemann paracrystalline concept [68], already suggested by Roldan and Kaufmann [118], to describe the β -structure as one with high distortion of the γ -structure.

It is therefore concluded here that there are basically two types of crystal structures, α - and γ - , for Nylon 6 and their unit cells are given by those of Holmes et al. [111] and Arimoto [125], Fig. 4.2(a) and (b). Depending on the processing condition, the γ -form can be obtained with varying degree of distortion, one of which is the mesomorphic β -form.

α - CRYSTAL

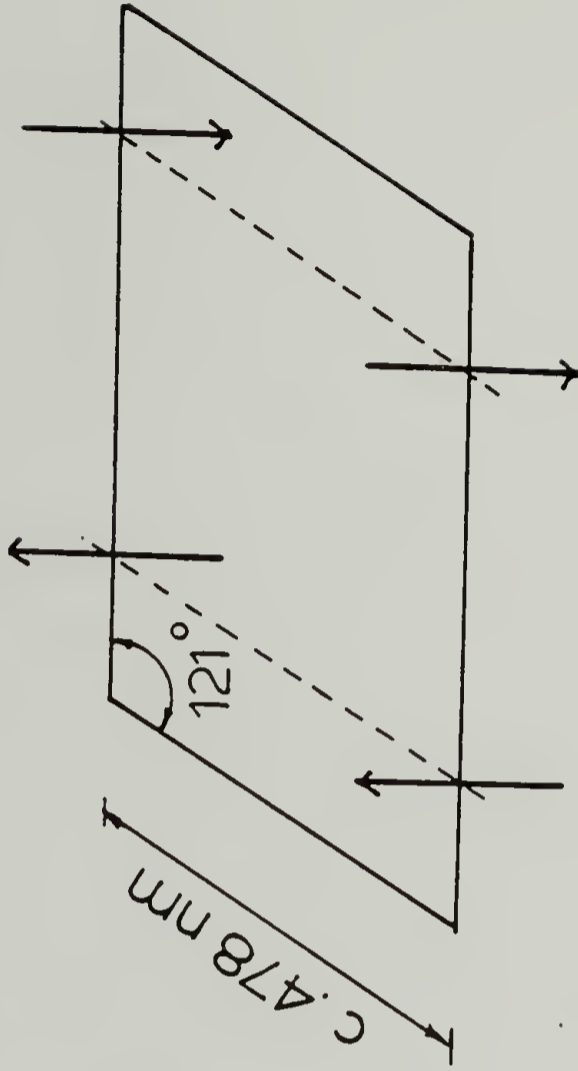
b 1.72 nm



a . 956 nm

(a)

γ - CRYSTAL
b 1.688 nm



c . 933 nm

(b)

Figure 4.2. Crystal structure of (a) α - and (b) γ -Nylon 6.

C H A P T E R V

SOLID-STATE CO-EXTRUSION OF NYLON 6 GEL

5.1 Background

Pennings and coworkers [130] reported ultra-high modulus PE of >100 GPa made by a continuous growth technique from solutions subjected to either Poiseuille or Couette flow. It was subsequently recognized that the fiber was produced from a gel layer where the fibrous seed-crystal was attached. The success of this technique is due to reduced molecular entanglements in the gel and to the efficient stretching of chains in a flow field.

Melt crystallized polymers usually have a high entanglement density which limits drawability. The molecular entanglements can be reduced by dilution with solvent. The number of entanglements in the solution, N_{soln} , is related to that in the melt, N_{melt} , by the polymer volume fraction, ϕ [131]:

$$N_{\text{soln}} = N_{\text{melt}} \phi \quad (5.1)$$

If the solution gels on cooling without collapsing

and retains all the solvent, the resultant gel can then be assumed to have the same entanglement density as the solution. The maximum draw ratio, λ_{\max} , has been shown [131] to relate to both the entanglement density and ϕ by

$$\lambda_{\max} = (N_{\text{melt}} / \phi)^{0.5} \quad (5.2)$$

Thus, the more dilute the solution, the higher is the maximum draw possible. However, there is a limit to dilution, as a coherent gel cannot be formed when the concentration is too low for polymer coil overlapping. Therefore, a high molecular weight polymer is usually used to prepare a low concentration gel. For PE, the typical molecular weight is $\sim 10^6$ in a gel of 1 to 2% concentration.

The potential of drawing gel as a route to high modulus fiber has received considerable attention [132, 133]. Smith and Lemstra [133] further extended the method to ultra-draw either a dried, molded or cast PE gel film. Such dried gel was reported to draw well, even up to 20X at room temperature [134]. Other polymers that form gels, polypropylene [135, 136] and poly(vinyl alcohol) [137] have also been reported to draw well by this method, resulting in high modulus fibers.

Lloyd [138] noted nearly 60 years ago that a gel is something which is easier to recognize than to define. This is still true today. A general definition of gel is

a colloidal semi-solid system rich in liquid [139]. The gel has at least two compositions and the states of their aggregation differ. Fig. 5.1(a) to (d) illustrate the four states of aggregation of a gel. Entanglements or contacts acting as junction points are necessary to give a spatial network to trap the liquid. Fig. 5.1(a) shows spherical particles adhering to each other in a linear array through interacting forces to form the network. These can be cohesive force, polar force or an intermediate linkage like tightly bound water molecules. An example of this is the gel formed by the spherical particles of bentonite clay. Rodlike particles can also build up a continuous framework in a similar way to form gel as in Fig. 5.1(b). Most polymer gels are, however, represented by the systems shown in either Fig. 5.1 (c) or (d).

When a polymer solution is cooled, it crystallizes. The micelle or crystallites formed can act as junction points for gel formation, Fig. 5.1(c). They can be very small or large junctions, not only in size but also in lattice order. Fig. 5.1(d) represents crosslinked polymers swollen with solvent forming a gel. In the present context, gel refers to a macroscopically coherent structure with the crystallites acting as spatial junction points, trapping a large amount of solvent.

In general, gels are not formed from a good solvent.

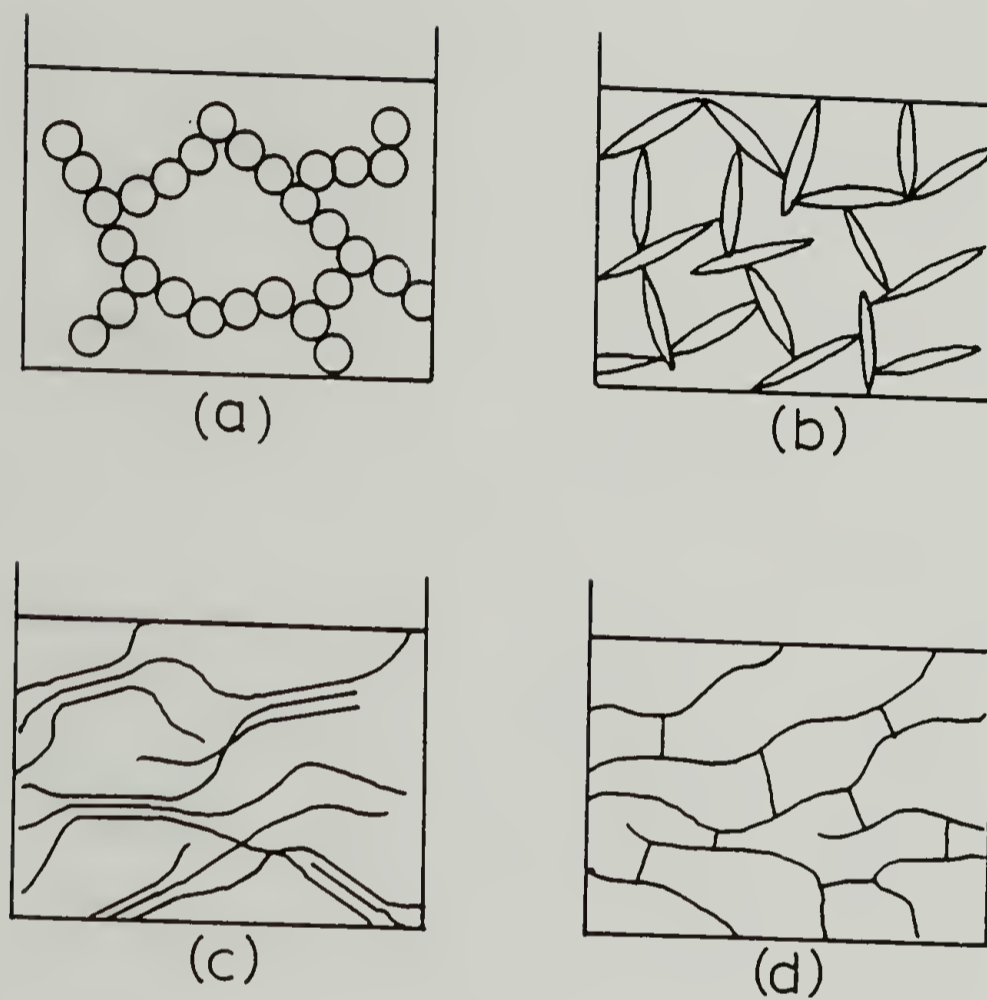


Figure 5.1. Schematics of the four states of aggregation for gel formation, (a) spherical particles linked linearly, (b) framework of rod-like particles, (c) micelles or crystallites of polymer and (d) crosslinked polymer network.

Gelation occurs when solubility is reduced by a variation of temperature or addition of a poor solvent to a polymer solution [140]. Apart from gelation involving flow, polymer can also gel under quiescent conditions as when a hot, semi-dilute solution is rapidly cooled. Gelation of semi-crystalline polymer has long been recognized as a crystallization process [139]. One molecular chain may form cohesive junction points with others at several loci along the chain to form a molecular network. If the junction is very small, the gel approaches a homogeneous one phase system. With several chain segments arranged in lateral order, the junction can then form micellar crystals. It was suggested by Keller [141] that micellar crystals are responsible for gel formation for polymers such as PE, poly(vinyl alcohol) and isotactic polystyrene. During the cooling process, larger lamellar crystals can also be crystallized simultaneously, which often gave the gel an opaque appearance. Thus in most polymer gel systems, micellar crystals are mixed with lamellar crystals which could possibly have tie molecules giving connectedness aiding gel formation.

Nylon 6 forms a gel when its solution in hot benzyl alcohol is cooled to room temperature [142]. Stamhuis and Pennings [143] investigated its morphology by electron microscopy and found interlacements of thin fibrillar crystals of 10 - 20 nm lateral dimension, aggregated into

ribbons of high aspect ratio. These fibrillar crystals have their chain axis perpendicular to the flat surface and the hydrogen bond direction is in the long axes of the crystal. The interlacements trap solvent and form a gel. Gelation in this case is analogous to the gelation of rodlike particles which form a continuous framework through physical contacts as in Fig. 5.1(b); the bulk of the molecular chains are not spatially spaced like a network. Thus Nylon 6 gel does not necessarily have as much reduced molecular entanglement as a PE gel.

The gel of Nylon 6 was reported to be brittle and could not be drawn [143]. However, by using solid-state co-extrusion with the gel film supported on each face by the surfaces of poly(oxyethylene) co-extrudate, a partially dried Nylon 6 gel was drawn up to 5.7X. This chapter investigates the drawing behavior and properties of the drawn gel. A deformation mechanism is proposed for the observed double orientation.

5.2 Experimental

Pellets of high molecular weight Nylon 6 ($[\eta] = 4.67$ dl/g in 85% formic acid, $M_v = 183,000$, Allied Chemicals) were dissolved in benzyl alcohol at 5 wt% concentration at 165°C. The solution was stirred for 1 hour under a N_2 atmosphere and was then poured into a petri dish lined

with filter paper where it gelled at room temperature . Solvent was subsequently removed by blotting with layers of filter paper applied at slowly increasing pressure, up to 40 MPa in a press. This was repeated until a partially dried gel was obtained. Solvent was further removed under vacuum at 40°C to give the final gel with ~20 wt.% solvent.

A 2 mm wide strip of the gel film, dried as above, was placed in the center of a split poly(oxymethylene) billet and co-extruded through a conical die of 20° entrance angle in an Instron capillary rheometer at 150°C. This extrusion temperature was chosen as a convenience as poly(oxymethylene) melts at ~160°C and draws easily up to 8X. Draw ratio was measured from the displacement of the lateral marks scribed on the gel prior to draw. About 10 wt% solvent remained in the extrudate and was removed in vacuum oven at 100°C for 48 hours.

Thermal behavior was characterized with a Perkin-Elmer DSC-II using a heating rate of 10°C/min. Indium and tin were used for calibration. Perkin-Elmer large volume stainless steel sample pans with O-ring seals were used for thermal analysis of the gel.

Tensile modulus at 0.1% strain was measured using a floor model Instron tensile tester at a strain rate of 0.01 min⁻¹ .

Total orientation of the drawn gel was measured by

birefringence using a Zeiss polarizing microscope with an Ehringhaus calcspat compensator. As the drawn gel developed double orientation, a Zeiss universal stage was used to measure birefringence as a function of tilt angle, α , by rotation about the draw axis [144, 145]. The sample was placed in between a glass hemisphere of 1.555 refractive index for beam convergence. This limits α measured up to 40° . Birefringence, Δ_i at the tilt angle α is given as

$$\Delta_i = \frac{R_\alpha}{t(1 - \sin^2 \alpha / n^2)^{-0.5}} \quad (5.3)$$

Extrapolation to $\alpha = 90^\circ$ gives birefringence of the other pair of axes.

Pole figure which shows the overall orientation was constructed from wide-angle X-ray scans using a Siemen D-500 diffractometer equipped with a scintillation counter operating at 40 kV and 30 mA, using a Cu K_α radiation with Ni filter. For each incremental azimuthal angle, ϕ , of 10° , the sample was scanned from polar angle, $\omega = 0$ to 360° , at a fixed 2θ angle for the (200) reflection. From $\phi = 0$ to 60° , the sample was scanned in a normal transmission mode [146]. From $\phi = 60$ to 90° , because of interference by the sample holder, an equi-angle reflection method [147] was used and the intensity at the common $\phi = 60^\circ$ was used as a scaling factor as described

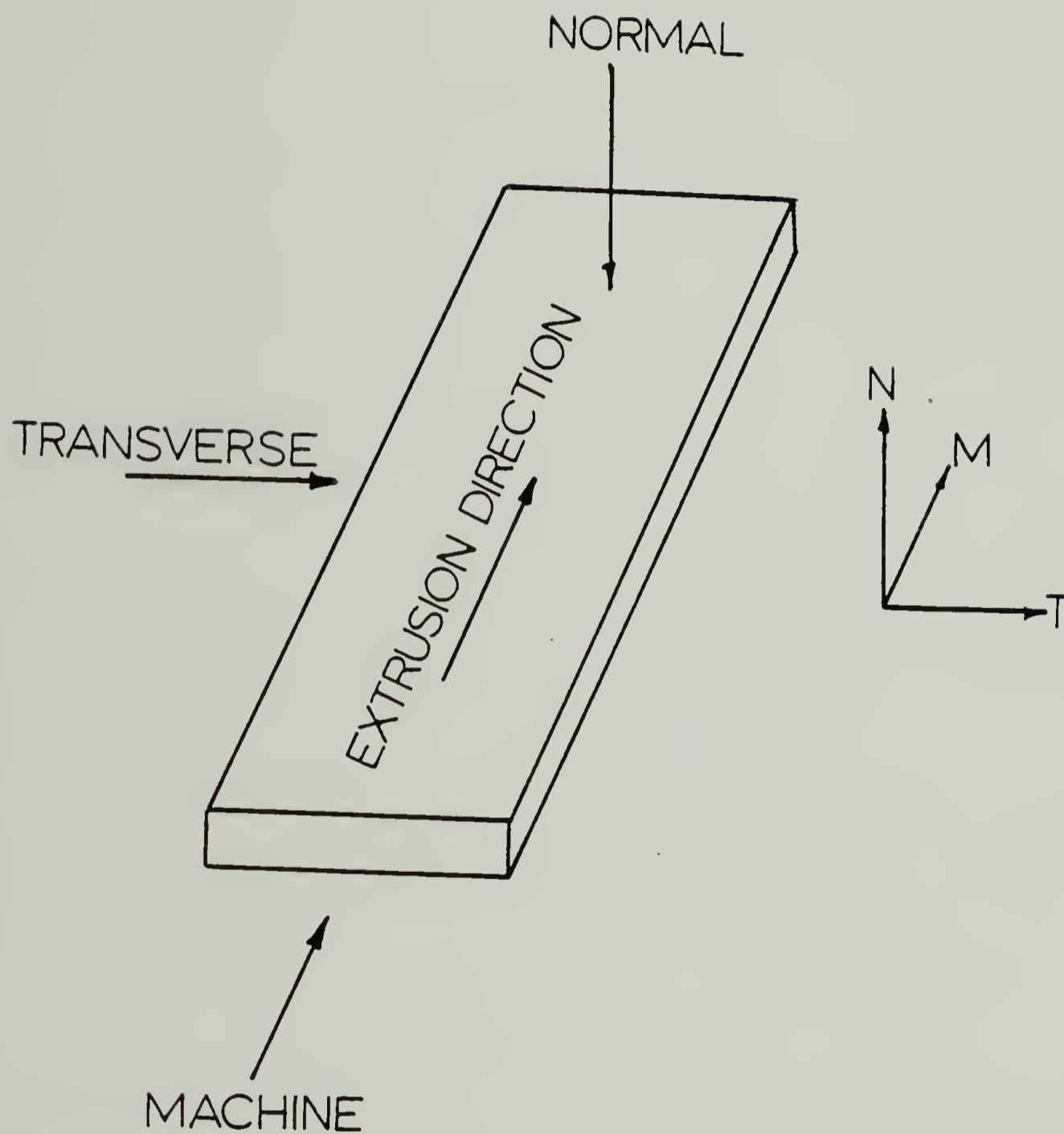


Figure 5.2. X-ray beam directions with respect to the coordinates of the gel film, normal (N), transverse (T) and parallel to the extrusion, also called the machine (M) direction.

by Alexander [67]. The intensities were corrected for background and absorption for both the transmission and reflection modes, and are normalized. Thus the average iso-intensity contour is 1 in the pole figure.

A flat film Statton camera with a sample-to-film distance of 5 cm and 32 cm was used to obtain, respectively, both the wide- and small-angle X-ray diffraction (WAXD and SAXS) photographs. The pinhole collimated X-ray beam was directed normal, transverse and parallel to the sample film plane and draw direction as defined in Fig. 5.2. The intensity of the SAXS films was measured with a Nonius microdensitometer. The long periods were calculated from the position of the peak maxima using Bragg's equation.

Crystallite size in the a-axis direction was measured from the broadening of the (200) diffraction with the diffractometer. The divergence and anti-scatterer slits were 0.3° and the receiving slit was 0.015° . The scanning rate was $0.2^\circ 2\theta/\text{min}$. The hexamethylene tetramine peak at $17.8^\circ 2\theta$ was used to correct for instrumental broadening. The crystallite size was calculated using Scherrer's equation (2.10).

5.3 Results and Discussion

5.3.1 Nylon 6 Gelation

When a hot Nylon 6 solution in benzyl alcohol was poured into a petri dish and allowed to cool at room temperature, it gelled at 40 - 45°C as observed by the increased viscosity. The gel at this stage is transparent. On further cooling, it became turbid. This Nylon 6 gel is inelastic and breaks up into lumps on deformation and therefore cannot be drawn in its present form. On prolonged standing, syneresis occurs. This is a process in which the liquid constituent of the gel is exuded slowly irrespective of the vapor pressure imposed upon the system and is accompanied by shrinkage in its volume. Syneresis is a continuation of the gelation process and it has been observed that the aggregates that caused gelation continued to grow larger [139]. Thus gelation is a non-equilibrium process. It was even reported for a poly(ethylene terephthalate) gel that crystallites were formed only during syneresis [148,149].

When benzyl alcohol was removed by evaporation in a vacuum oven at room temperature, a white, porous and brittle mass of Nylon 6 was left. When it was soaked in benzyl alcohol, it imbibed the solvent but did not revert back to the gel state, which is therefore irreversible. Many inorganic gels exhibit this type of behavior [139]. However, when benzyl alcohol was removed with pressure applied onto the gel simultaneously, a compact, translucent film was obtained. With 10 - 20% of the

solvent deliberately left in it, the film appeared leatherly and this partially dried gel film was prepared as a starting material for drawing in this study.

Fig. 5.3 shows the DSC scan of the gel heated at $10^{\circ}\text{C}/\text{min}$. A broad endotherm from 89 to 124°C is observed with the peak melting point at 104.9°C . This endotherm is from the dissolution of the crystals in the gel and has a ΔH of 5.63 kJ/kg. When the heat of fusion is expressed in terms of the solid content, ΔH is 112.6 kJ/kg (59.9% crystallinity) which is very high showing the aggregates of the gel are highly crystalline. This is comparable to the 55% crystallinity obtained from a dried gel film by DSC.

Stamhuis and Pennings [143] found that the peak melting point of the gel is dependent on both heating rate and on the gelation temperature. Lower heating rate increases the peak temperature. For a 2 wt.% gel, the peak temperature was 101°C when the solution was gelled at 25°C and increases to 124°C at 100°C gelation temperature.

When the dissolved gel was cooled from 130°C to room temperature in the DSC at 2.5 and $10^{\circ}\text{C}/\text{min}$, no exotherm was observed. It was therefore thermally irreversible at these cooling rates. However, when the sample was left standing at room temperature for over 1 week, reheating produced the same exotherm. Thus it is likely that crystals are formed and continued to grow during syneresis

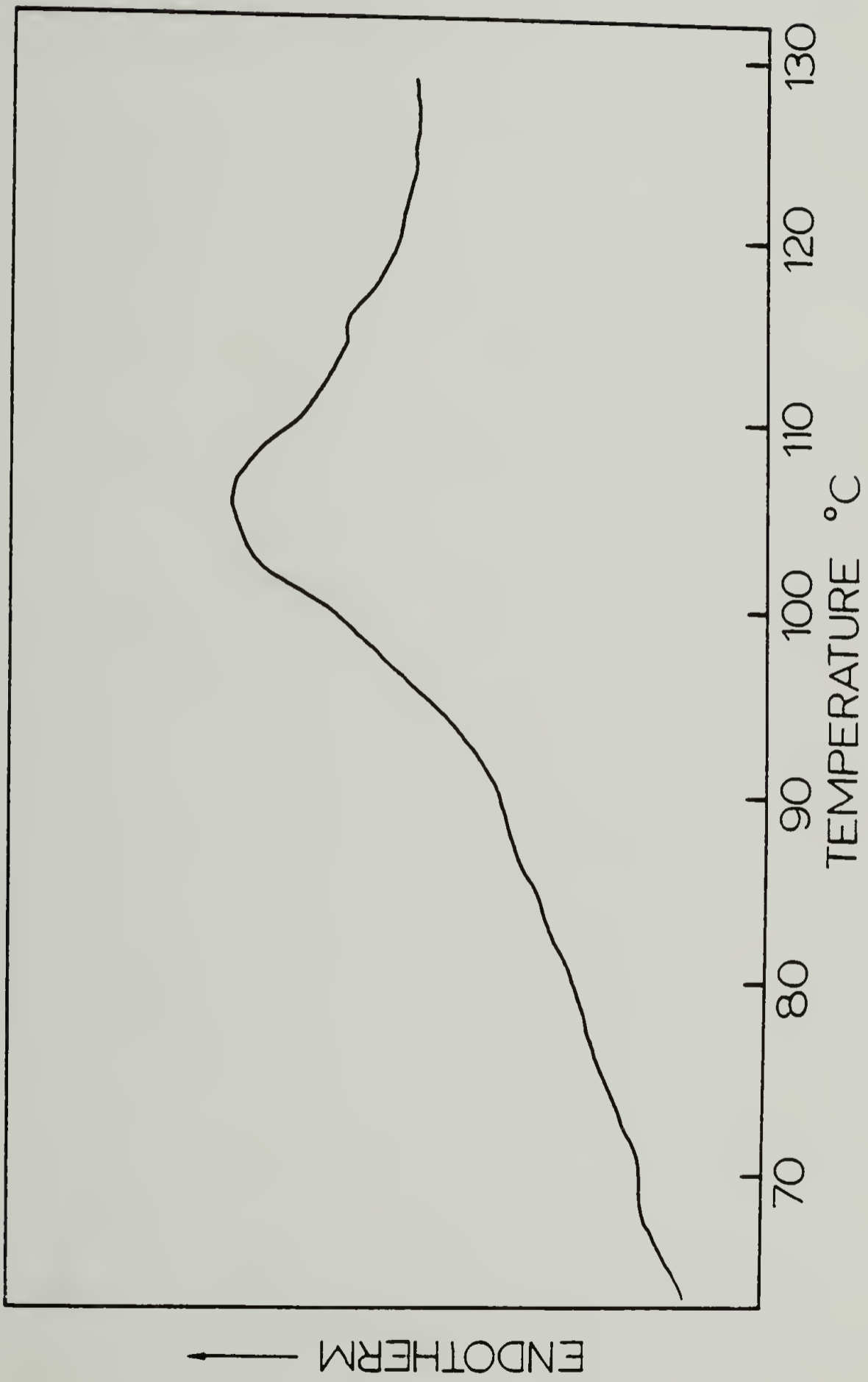


Figure 5.3. DSC scan of a 5 wt% Nylon 6 gel.

as in the poly(ethylene terephthalate) gel.

5.3.2 Characterization of Undrawn Gel Film

Nylon 6 was found to gel into the α -crystals with a high crystallinity, 55%, as measured from DSC. This crystal form is the one normally obtained by solution crystallization. A DSC scan of a thoroughly dried gel, Fig. 5.4, shows two prominent endotherms with peak melting point at 210 and 219.5°C. The two endotherms have approximately equal peak area. Double endotherms in solution crystallized Nylon 6 have previously been reported [150]. Kyotani [151] attributed the low temperature endotherm to the formation of smaller lamellar crystals which crystallized during cooling after the isothermal crystallization. Prolonging the isothermal crystallization time was reported to give only the single high temperature endotherm of more perfect, larger lamellar crystals. However, Stamhuis and Pennings had shown that Nylon 6 gel has long ribbons of aggregated fibrillar crystals. This morphology was also obtained from stirred crystallization in a 1,2,6-hexanetriol solution and has a melting point of 223°C [151], nearly the same as that of the large lamellae from prolonged isothermal crystallization. Thus in the present gel system, the observed high temperature endotherm is likely for fibrillar crystals mixed with possibly some large

lamellar crystals.

Fig. 5.5(a) and (b) shows WAXD and SAXS photographs of a dried gel film prior to extrusion draw. The X-ray beam was directed perpendicular and parallel to the film plane. When viewed perpendicularly, Fig. 5.5(a), there are two (200) and (002) isotropic rings. The inner (200) reflection is much more intense than the outer (002) reflection. SAXS however shows that over a larger range, the system is not entirely isotropic as indicated by an uneven intensity distribution of the rings. When the X-ray beam is placed parallel to the film plane, Fig. 5.5(b), wide equatorial (200) and (002) arcs are observed superimposed on the Debye rings, and SAXS shows wide meridional maxima. These indicate that orientation has been introduced in the gel film with the b-chain axis weakly oriented perpendicular to the film plane as a result of squeezing during solvent removal. This is confirmed by the WAXD photograph, taken with the beam parallel to an unpressed gel, which shows only isotropic rings. The preorientation, however, does not cause the observed double orientation of crystals in the drawn gel, to be discussed later. It does affect the distribution of crystals when viewed parallel to the draw direction.

5.3.3 Properties of Drawn Gel Film

Thermal analysis by DSC of the drawn gel film is

shown in Fig. 5.4. With increasing draw ratio, the low temperature endotherm decreases in magnitude and shifts slightly towards higher temperature, completely disappearing at draw ratio 4.6 and onwards, leaving only a single endotherm with a peak melting at 224°C at draw ratio 5.4. The disappearance of the low temperature endotherm must be due to the destruction of these lamellar crystals on draw leading to their incorporation in a newly formed fibrous morphology. The fate of the ribbons of fibrillar crystals on draw is not revealed by DSC since its melting point is in the same range as that of the drawn fibrous morphology [152]. The crystallinity decreases with drawing by $\sim 9\%$ at the highest draw ratio 5.7 (Table 5.1). A major decrease had also been observed for crystalline poly(ethylene terephthalate) [153] with yet no satisfactory explanation.

As pointed out earlier, Nylon 6 gel formation does not necessarily result in significant reduced molecular entanglement. The maximum draw ratio of 5.7 obtained here is comparable to those previously reported for Nylon 6 [154]. Tensile moduli of the drawn gel are shown in Fig. 5.6. The moduli of a solvent cast film, drawn under similar conditions and shown by the broken line, are included for comparison. At equivalent draw ratios, the modulus of the gel film is modestly higher, reaching 5.6 GPa. Annealing at 190°C with both ends fixed shows a

Figure 5.4. DSC scans of undrawn and drawn Nylon 6 Gel films.

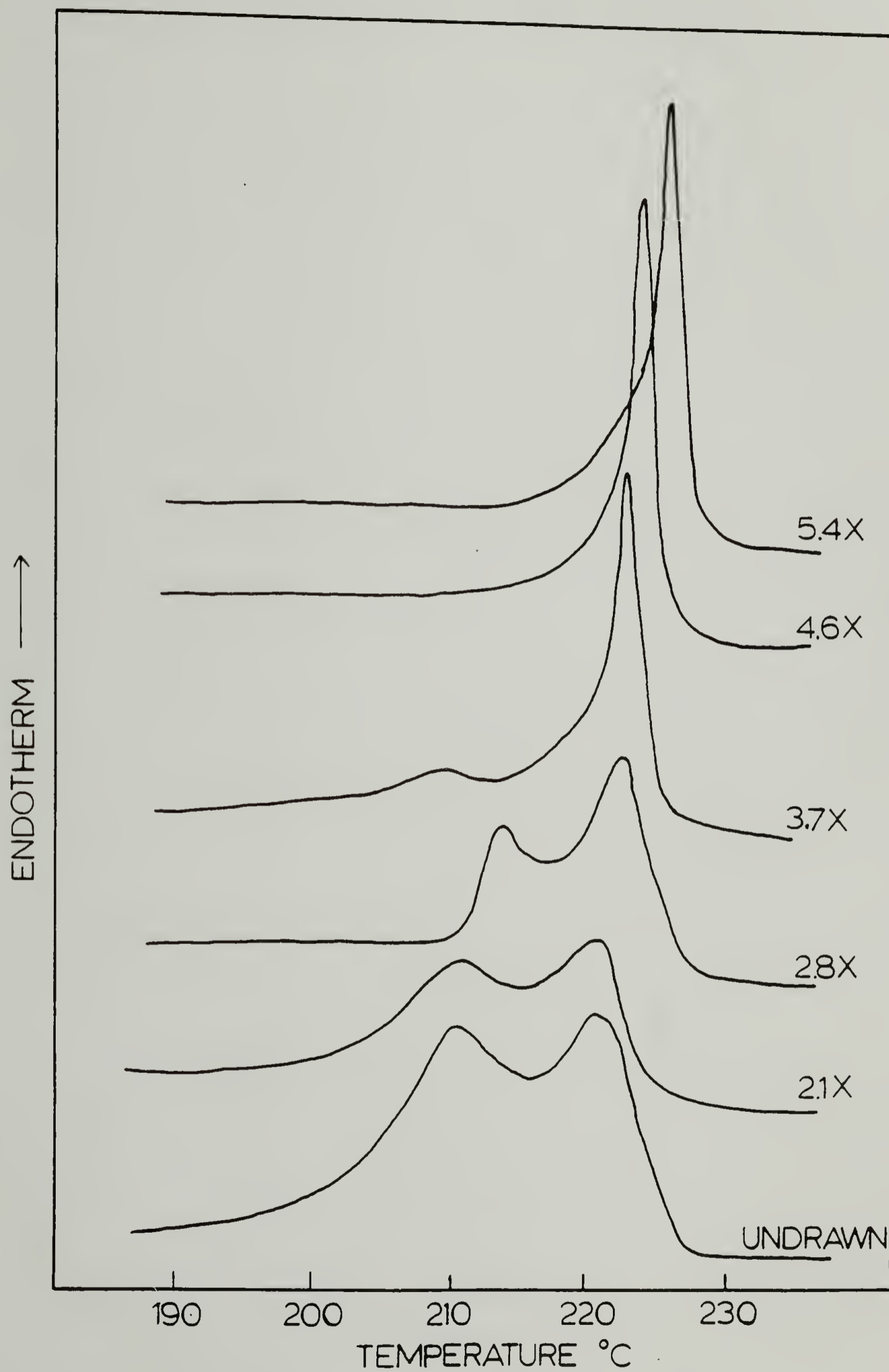


Figure 5.5. WAXD and SAXS photographs of undrawn, dried gel with X-ray beam (a) normal and (b) parallel to film plane.

SAXS



WAXD



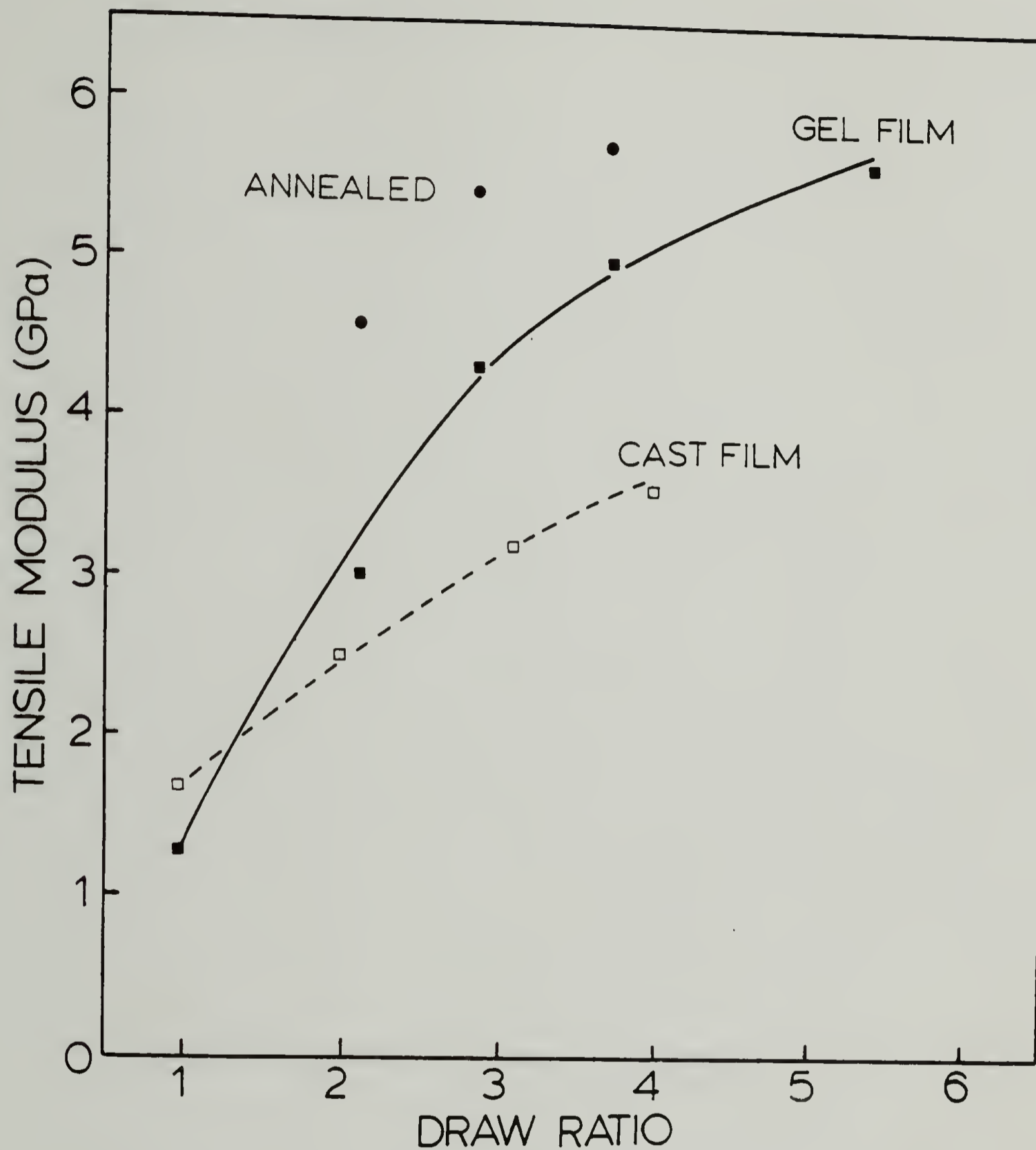


Figure 5.6. Tensile modulus as a function of draw ratio for solvent-cast Nylon 6 film; Nylon 6 gel film before and after annealing at 190°C.

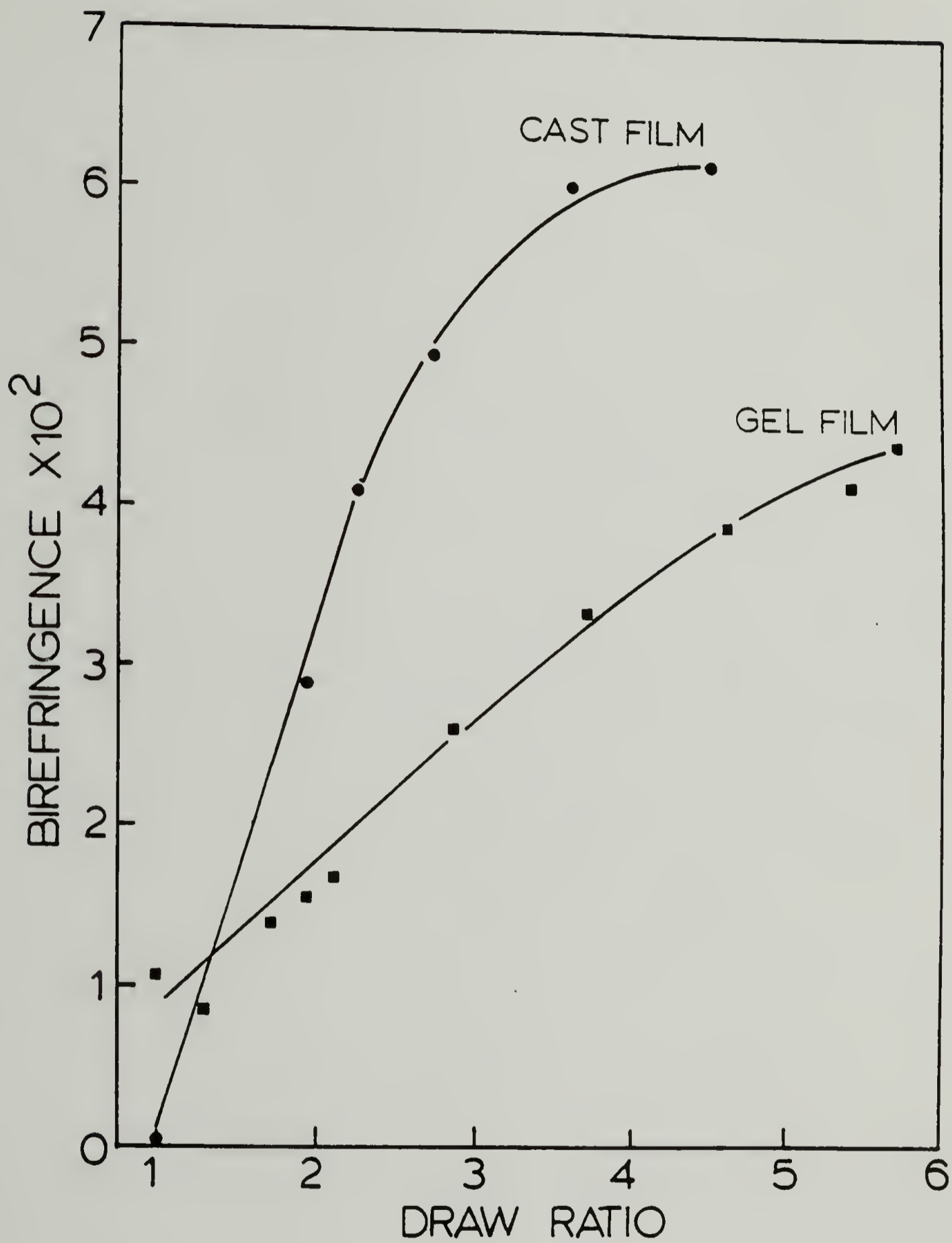


Figure 5.7. Birefringence as a function of draw ratio for Nylon 6 gel and solvent-cast Nylon 6 films.

Table 5.1

Change in Percent Crystallinity as Measured by
DSC as a Function of Draw Ratio

Draw Ratio	% Crystallinity
Undrawn	55.0
2.1	47.8
2.9	48.7
3.7	47.3
4.6	45.6
5.4	45.0
5.7	45.5

slight improvement in the modulus, Fig. 5.6.

The total orientation of both the amorphous and crystalline chains was measured by birefringence, Fig. 5.7. The undrawn film is slightly birefringent, $\Delta = 0.011$, which is due to the orientation introduced during solvent removal. On drawing, the birefringence increases, almost linearly to 0.044 at a draw of 5.7. By comparison, the drawn solvent cast film increases sharply at low draw, reaching a plateau of 0.061 at a draw of 3.5 with values consistent with reports on uniaxially drawn Nylon 6 film and filament [154]. The lower birefringence of the drawn gel can be explained. Investigations by both WAXD and SAXS show double orientation; there are two populations of crystals with chain axis either parallel or perpendicular to the draw direction. Since birefringence is the difference in refractive indices along and perpendicular to draw, the presence of a crystal fraction with chain axis perpendicular to draw direction reduces the birefringence.

5.3.4 Deformation Mechanism

Double orientation on deformation has been reported for several types of gel [149, 155, 156]. An elegant explanation has been offered by Keller [141] in which the initial gel contains a mixture of both micellar and lamellar crystals. On deformation, the micellar crystals

orient with their chain axis in the draw direction as in the stretching of a network, while the lamellar crystals align with their lamellar planes along the stretch direction and therefore with chain axis perpendicular to draw. An unconnected lamellar crystal could possibly orient this way on drawing without much chain unravelling. It is less likely that lamellar crystals with molecular weight $\sim 10^6$ and possibly interconnected, will do so rather than orienting with chain unravelling to form fibrous morphology with chain axis in the draw direction.

Since gelation of Nylon 6 is caused by the interlacement of fibrillar crystals, a different morphology from a PE gel, an alternative mechanism is proposed: orientation of crystals with chain axis in the draw direction arises from the fibrous morphology normally observed in uniaxial drawing. The second orientation of crystals with chain axis perpendicular to draw direction, are from the fibrillar crystals which have chain axis perpendicular to the surface plane and with the hydrogen bond in the long axis. They rotate when subjected to torque on deformation so that the long axis (a-axis) is preferentially oriented in the draw direction and consequently with chain axis perpendicular to draw. This is similar to the rotation of needle shape crystals in segmented polyurethane to give a negative orientation as proposed by Bonart [157]. This proposed mechanism is

shown to be consistent with the birefringence, WAXD and SAXS results as a function of draw ratio.

Pole figures are the best way to show unambiguously complex orientation. The normal of the diffraction plane when intersected with a hypothetical sphere of reflection gave the pole. A stereographical projection of the distribution of these poles is a pole figure which is plotted with a series of contour lines of constant intensity. Therefore, it is a visual representation of the orientation distribution. Fig. 5.8 shows a (200) pole figure of a gel film drawn 4.6X. Double orientation can be easily seen from this plot with the pole strongly concentrated at the equator, and another less intense concentration at $\phi = 65^\circ$. The pole at the equator is from crystals oriented with their chain axis parallel to the draw direction. The distribution of the intensity is uneven along the equator, with higher intensity, >2.0 , concentrated at $\omega = 0^\circ$ and gradually decreases to 1.0, the average intensity at $\omega = 90^\circ$. Thus the distribution of this crystal is not centrosymmetrical about the draw axis. There is a higher population of the crystals with (200) planes parallel to the film plane than to the transverse plane. The less than average intensity of the pole at $\phi = 65^\circ$ shows that there is a smaller population of crystals with chain-axis oriented perpendicular to the draw direction. Though pole figures are the best way of

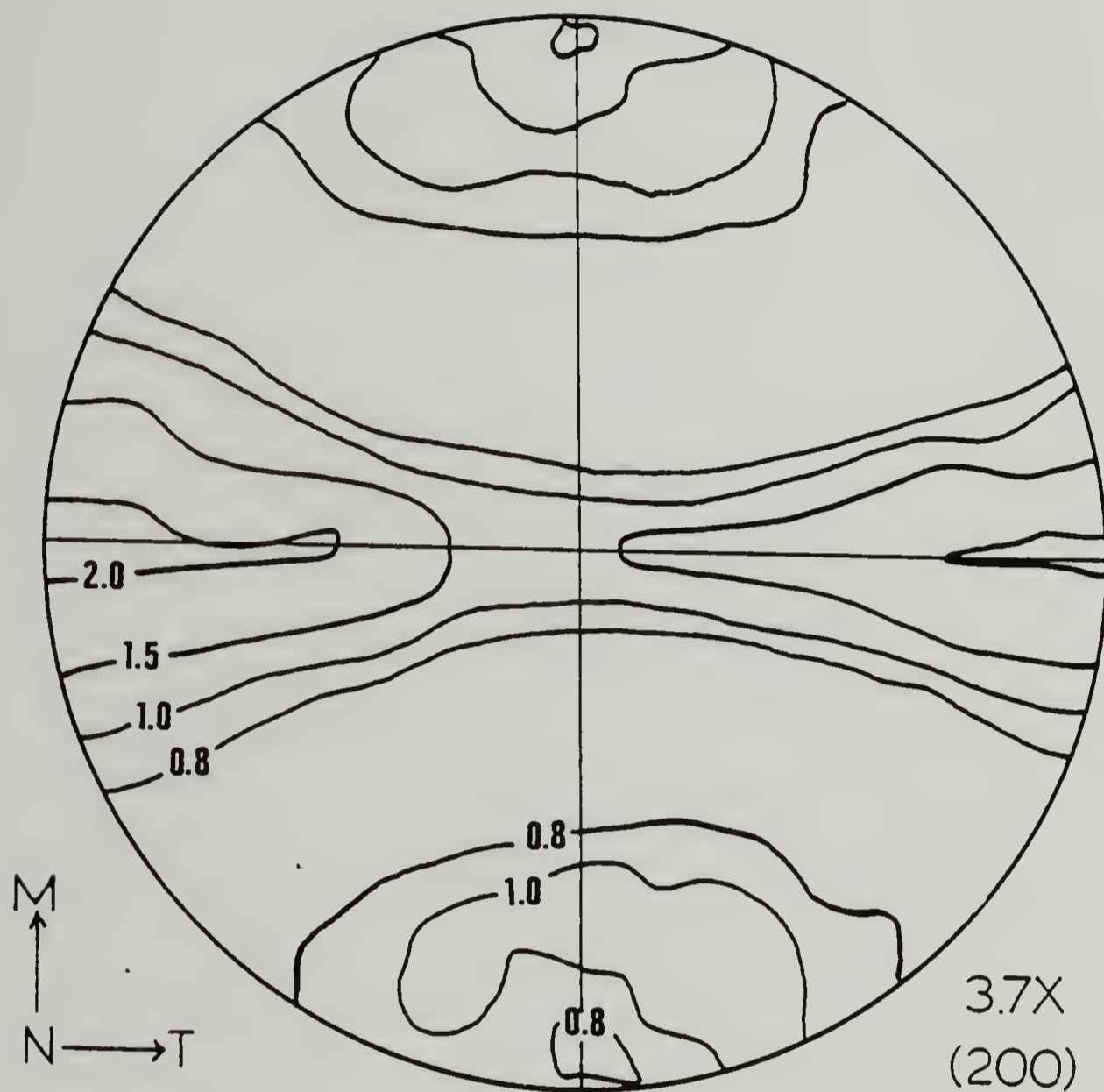


Figure 5.8. Pole figure of (200) reflection of Nylon 6 gel drawn 3.7X.

Figure 5.9. WAXD photographs of Nylon 6 gel film with increasing draw ratio, X-ray beam normal to film plane.



1.9X



1.7X



1.3X



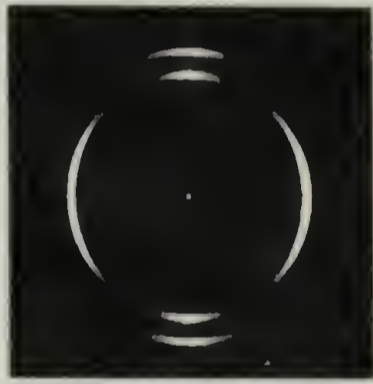
UNDRAWN



4.6X



3.7X



2.9X



2.1X

EXTRUSION DIRECTION
←

showing complex orientation, they are somewhat laborious. Alternatively, WAXD films were taken with X-ray beam directed normal, transverse and parallel to the plane of the gel film to show the orientation development on drawing.

Fig. 5.9 shows a series of WAXD photographs of the gel films with increasing draw ratio: the X-ray beam is normal to the film plane. The undrawn film shows isotropy with (200) and (002) Debye rings. The outer (002) reflection is mixed with (202). For convenience, we refer to this as (002) only. At low draw ratio, up to 1.7X, the inner (200) reflection forms meridional arcs with broad azimuthal spread, while the outer equatorial (002) arcs are also broad but less intense. At draw ratio of 1.9, the spread of these two arcs becomes narrower with simultaneous development of a faint (200) reflection at the equator. These equatorial arcs become prominent at a draw 2.9X while the meridional (200) arcs become narrower in spread and split with maximum intensity centered at a $\sim 22^\circ$ angle to the extrusion direction. Correspondingly, the azimuthal spread of meridional (002) also becomes narrower. There is a faint reflection located diagonally with its spacing nearly the same as that of the outer (002) reflection, which was indentified as a weak (202) reflection. At higher draw of 4.6, the intensity of meridional (200) arcs decreases sharply when compared to

its equatorial reflection.

Because of the complex orientation, we also examined both WAXD and SAXS with the X-ray beam transverse and parallel to the draw. The transverse diffraction shows similar patterns to that of diffraction normal to the film plane. At low draw, the parallel direction diffraction shows a weak orientation which was introduced during squeezing in the gel film preparation with a broad equatorial (200) arc. On further drawing to 3.7X, it develops into a ring of uneven intensity around the draw direction as already shown by the pole figure of Fig. 5.8, so the system can be described as having double orientation of the crystals but not entirely centrosymmetric around the draw direction at higher draw.

In Fig. 5.9, the equatorial (200) and (002) reflections can be identified as from the normal fibrous morphology with chain axes parallel to the uniaxial draw direction. The meridional (200) reflections are, however, from crystals with their chain axes oriented perpendicular to the draw direction. The reflections are suggested here to be from the fibrillar crystals which have chain-axis perpendicular to their flat surfaces.

To show how these diffraction patterns are obtained for these crystals, a reciprocal $a^* - c^*$ lattice for the fibrillar crystals with their chain axis oriented perpendicular to the draw direction is constructed. Since

WAXD patterns are taken with a flat film camera and with Cu K $_{\alpha}$ radiation of wavelength 0.154 nm, the surface of the Ewald sphere is curved. The flat film diffraction pattern is then a slight distortion of the reciprocal lattice representation. Nevertheless, it is useful to show the relative location of the reflections arising from the orientation.

The reciprocal lattice is oriented such that the (002) reflection is at the equator, while the (200) reflection is at the meridian, Fig. 5.10(a). At low draw, the fibrillar crystals rotate when subject to torques. The a-axis orients towards the draw direction. Since the c^* -axis is perpendicular to the a-axis, the measurement of the angle of (002) reflection from the equator, ψ , indicates the angle at which the a-axis is tilted towards the draw direction. Because of wide angular spread of the a-axis, there is a spread of (200) and (002) reflections smeared over the meridian and equator, respectively. This results in WAXD patterns for draw $\times 1.7$ as shown in Fig. 5.9.

At higher draw, when the a-axis of the fibrillar crystals are oriented in the draw direction, ψ becomes 0° . The diffraction pattern is then represented by a reciprocal lattice as in Fig. 5.10(b). In this case the meridional (200) reflections show intensity maxima at an angle of 22.5° from the draw direction, which is indeed

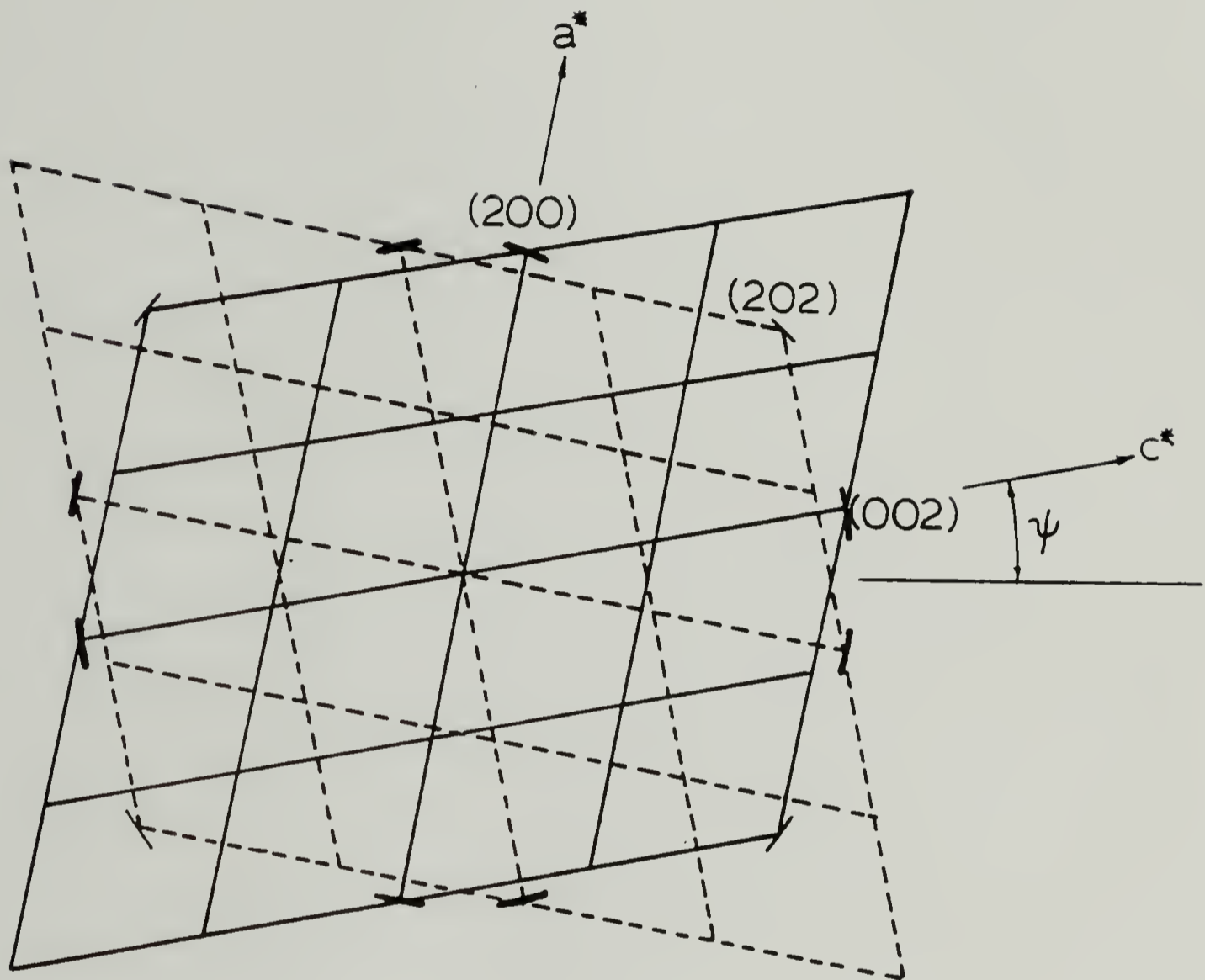


Figure 5.10(a). Reciprocal lattice of Nylon 6 fibrillar α -crystal at low draw (1.9X, showing the relative position of the (200), (002) and (202) reflections as would be observed in WAXD.

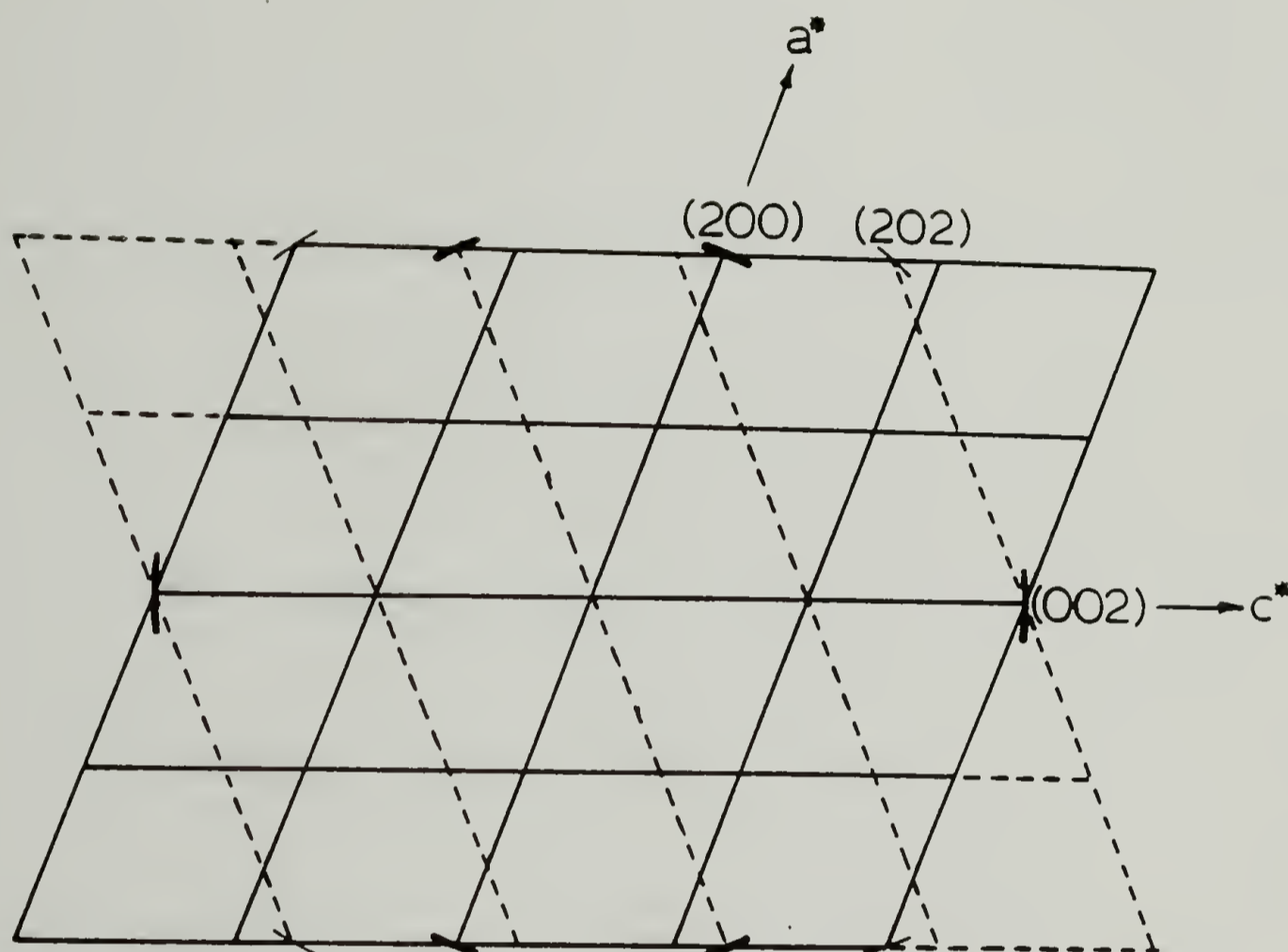


Figure 5.10(b). Reciprocal lattice of Nylon 6 fibrillar α -crystal at high draw $>3.7X$, showing the relative position of the (200) , (002) and (202) reflections as would be observed in WAXD.

Table 5.2

Crystallite Sizes Along a-axis for (200) Equatorial and Meridional Reflections with Increasing Draw Ratio

Draw Ratio	Crystallite Size \bar{D}_{200} (nm)	
	Equatorial	Meridional
Undrawn	10.4	-
1.9	6.4	10.1
3.7	6.2	9.1
4.6	6.9	8.2
5.4	6.9	9.1

observed from draw ratio 3.7X onwards indicating a complete a-axis orientation of the fibrillar crystals in the draw direction. A weak (202) reflection appears diagonally in the reciprocal lattice and is also observed in the diffraction pattern.

If we now superimpose on Fig. 5.10(b) the equatorial (200) and (002) reflections from the normal fibrous morphology with chain axis in the draw direction, the composite will be consistent with the WAXD observed for draw ratio >3.7 of Fig. 5.9.

Crystallite sizes along a-axis for both types of crystal orientations, were measured from WAXD (200) line broadening at the equator and meridian, and are shown in Table 5.2. Scherrer's equation was used after correction for instrumental broadening. It was assumed that broadening is due to crystallite size alone, neglecting lattice distortion. Therefore, the measured size is a lower estimate. The measurement of (002) broadening is not suitable, as it is not a pure peak, but a mixture with (202) reflection. The crystallite sizes of fibrillar crystals along the a-axis, as measured from broadening of the meridional (200) reflection, showed a slight decrease on draw, from 10.1 nm at 1.9X to 8.2 - 9.1 nm at higher draw. For the equatorial (200) reflection, the crystallite sizes remain fairly constant on draw, 6.2 - 6.9 nm. This dimension may be interpreted as the lateral

size of the drawn microfibril and agreed well with those previously reported for drawn melt crystallized Nylon 6. Consider the interchain dimension of 0.4 - 0.5 nm. Arithmetically, this corresponds to about 15 Nylon 6 chains in close lateral packing. This number indicates that the equatorial (200) reflection is unlikely the result of drawing a micellar crystals network.

While the WAXD study gives information of how chains are oriented at the level of unit cell axes, SAXS provides a view of orientation at the larger lamellar level. Fig. 5.11 shows SAXS patterns of gel films with increasing draw ratio. At low draw of 1.3X, there is a marked change of the scattering pattern from nearly isotropic scattering for the undrawn state to a discrete four-point pattern at the equator. At higher draw, the four points move closer to the equator, while meridional scattering develops at 1.9X, thus giving a six-point scattering pattern. On further draw, the equatorial four points merge into two points at 3.7X, giving a final four-point scattering along both the meridian and equator.

To show that the equatorial scattering is not due to voids, the drawn film was immersed in benzyl alcohol (refractive index 1.54) for 14 days. It was then coated with paraffin oil to reduce solvent evaporation under vacuum when taking the SAXS films. The patterns were found to be the same, indicating the equatorial scattering

is not due to voids.

The measured lamellar long periods are tabulated in Table 5.3. The meridional long period of the drawn fibrous morphology is constant at ~ 8.5 nm. The equatorial periodicity of the fibrillar crystals is smaller but remains fairly constant at ~ 6.5 nm on draw. Although Stamhuis and Pennings found the lateral dimension of such crystals to be 10 - 20 nm, the thickness in the chain direction was not reported. The present periodicity is within the range of lamellar thickness obtained for solution grown Nylon 6 crystals [42].

The split angle, ψ , of the equatorial scattering maxima gives the average angle of the long axis of fibrillar crystals to the draw direction. At a draw of 1.3X, the angle is 23.6° and decreases to 0° at 3.7X (Table 5.4). At this draw ratio, the long axis (a-axis) of the fibrillar crystals is already completely oriented in the draw direction. Thus the SAXS results support the observation from WAXD.

From both WAXD and SAXS studies, we showed there is a double orientation in the drawn film. One population of the crystals has chain axis parallel to the uniaxial draw direction. These type of crystals belong to the fibrous morphology normally developed in tensile drawing. The other crystal population has chain axis perpendicular to the draw, and they are identified as the fibrillar

crystals associated with gelation. They rotate when subjected to torques during deformation, with the long axis orienting towards the draw direction. Because hydrogen bond is also in the long axis, chains resist drawing until the later stages when "fracture" possibly occurs and transform partly into the fibrous morphology with chain axis in the draw direction. This causes the depletion of the fibrillar crystals and therefore a decrease in the SAXS equatorial intensity. Fig. 5.12 is a schematic of ribbons of these fibrillar crystals undergoing deformation with their long axis rotating towards the draw direction. The lines represent fibrillar crystals, bundled into larger ribbons, and not the individual molecular chains. At low draw, Fig. 5.12(b) shows the long axis partially oriented towards the draw direction. Since the fibrillar crystals are distributed about the draw direction, this arrangement gives four-point SAXS pattern at the equator. On further drawing, Fig. 5.12(c), the long axis is in the draw direction; the four-point scattering merges with a decrease in the ψ angle and finally coalesces into two equatorial scatterings. Together with this, there is a simultaneous development of the fibrous morphology which has meridional scatterings superimposed on the above, it results in the observed four-point scattering on the meridian and equator shown in Fig. 5.11.

Table 5.3

Long Period from SAXS of Gel Film
with Increasing Draw Ratio
X-Ray Beam Normal to Film Plane

Draw Ratio	Long Period (nm)	
	Equatorial	Meridional
Undrawn	6.4	-
1.3	6.6	8.7
1.9	6.6	8.6
2.1	6.8	8.8
2.8	6.6	8.5
3.7	6.5	8.7
4.6	6.2	8.2
5.4	6.2	8.1

Table 5.4

Change of Angle, ψ , Between Long Axis of
Fibrillar Crystals and the Draw Direction

Draw Ratio	ψ
1.3	23.6
1.9	12.0
2.1	10.1
2.8	9.2
3.7	0

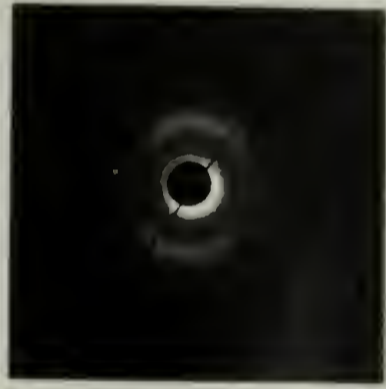
Figure 5.11. SAXS photographs of gel film with increasing draw ratio, X-ray beam normal to film plane.



1.9X



1.7X



1.3X



UNDRAWN



4.6X



3.7X



2.9X



2.1X

EXTRUSION DIRECTION
←

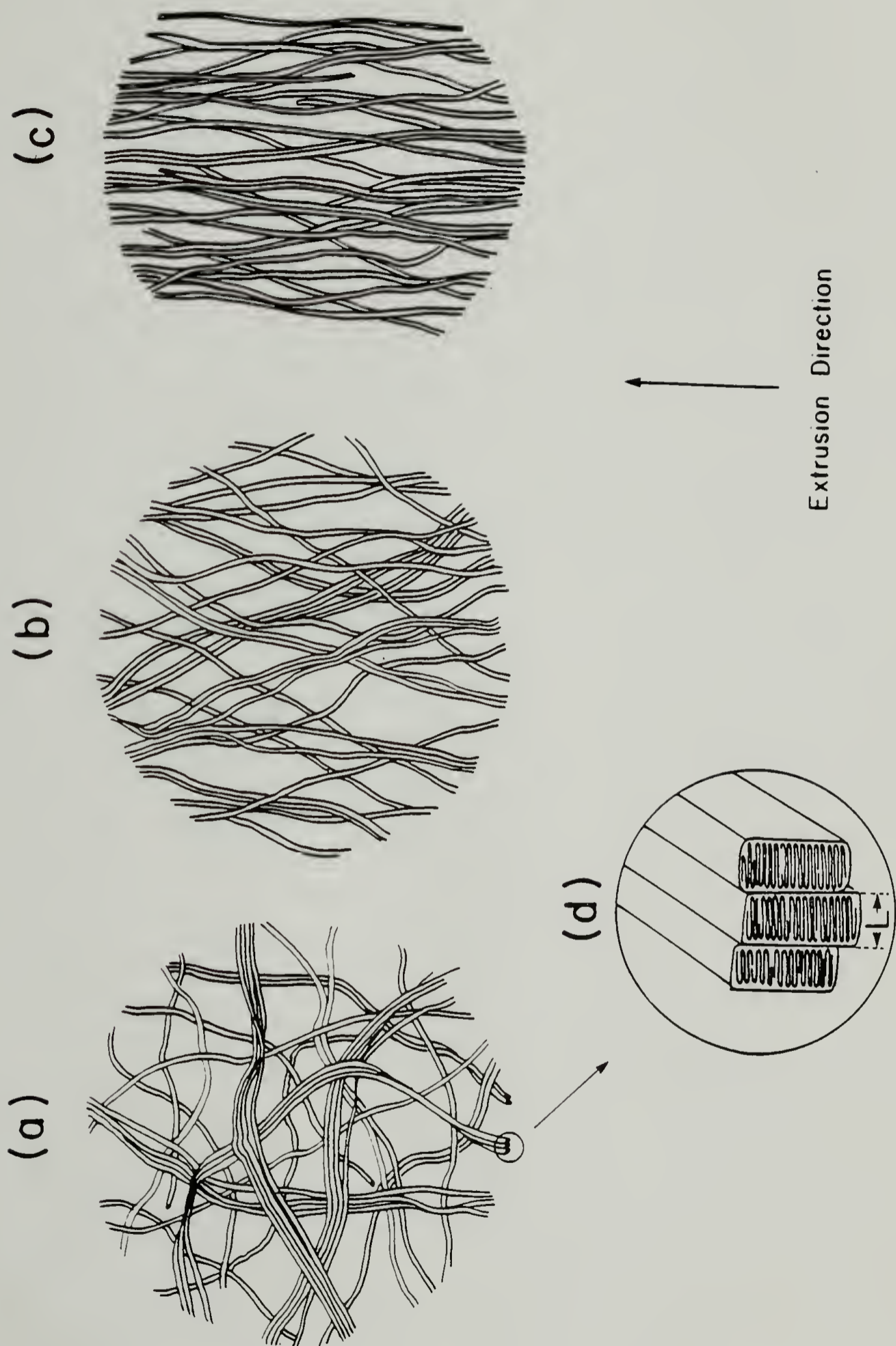
Figure 5.12. Schematic representation of orientation of the fibrillar crystals during deformation.

(a) Undrawn state with random interlacement of fibrillar crystals.

(b) At low draw ratio $< 1.9X$, long axis (a-axis) of the fibrillar crystals weakly oriented towards draw direction.

(c) At high draw ratio $> 3.7X$, long axis of the fibrillar crystals oriented in draw direction.

(d) Enlargement of the aggregates of fibrillar crystals showing the long period.



5.3.5 Annealing Behavior

The drawn gel films were annealed with fixed ends at 190° for 3 hours. The modulus and birefringence increase slightly (Fig. 5.6 and 5.7). WAXD and SAXS with the X-ray beam in the normal and transverse directions are not significantly different from that of unannealed samples. However, when the beam is in the draw direction, superimposed on both the (200) and (002) rings are intense arcs at the equator similar to that of the undrawn state of Fig. 5.5(b). Reorientation of the undrawn fibrillar crystals occurs on annealing with the chain axes partially reoriented normal to film plane. Annealing results in a more complicated orientation.

Birefringence of both unannealed and annealed gel film of draw 2.1X, 2.9X and 3.7X are shown in Fig. 5.13 (a) to (c) as a function of tilt angle, α . For unannealed sample, there is only a slight increase of birefringence with α , indicating a slight departure from isotropy around the draw axis. On annealing, because of the reorientation, the samples not only show higher birefringence but it also increases with tilt angle. The increase is linear for draw 2.9X up to the angles measured, but shows a tendency toward reaching a plateau in draw 3.7X. For the biaxial orientation, the birefringence at $\alpha = 0^\circ$ is different from at $\alpha = 90^\circ$. A plot of birefringence vs. $\sin^2 \alpha$ is linear and

Figure 5.13. Birefringence as a function of tilt angle α for unannealed and annealed drawn gel. Draw ratio (a)2.1, (b)2.9 and (c)3.7.

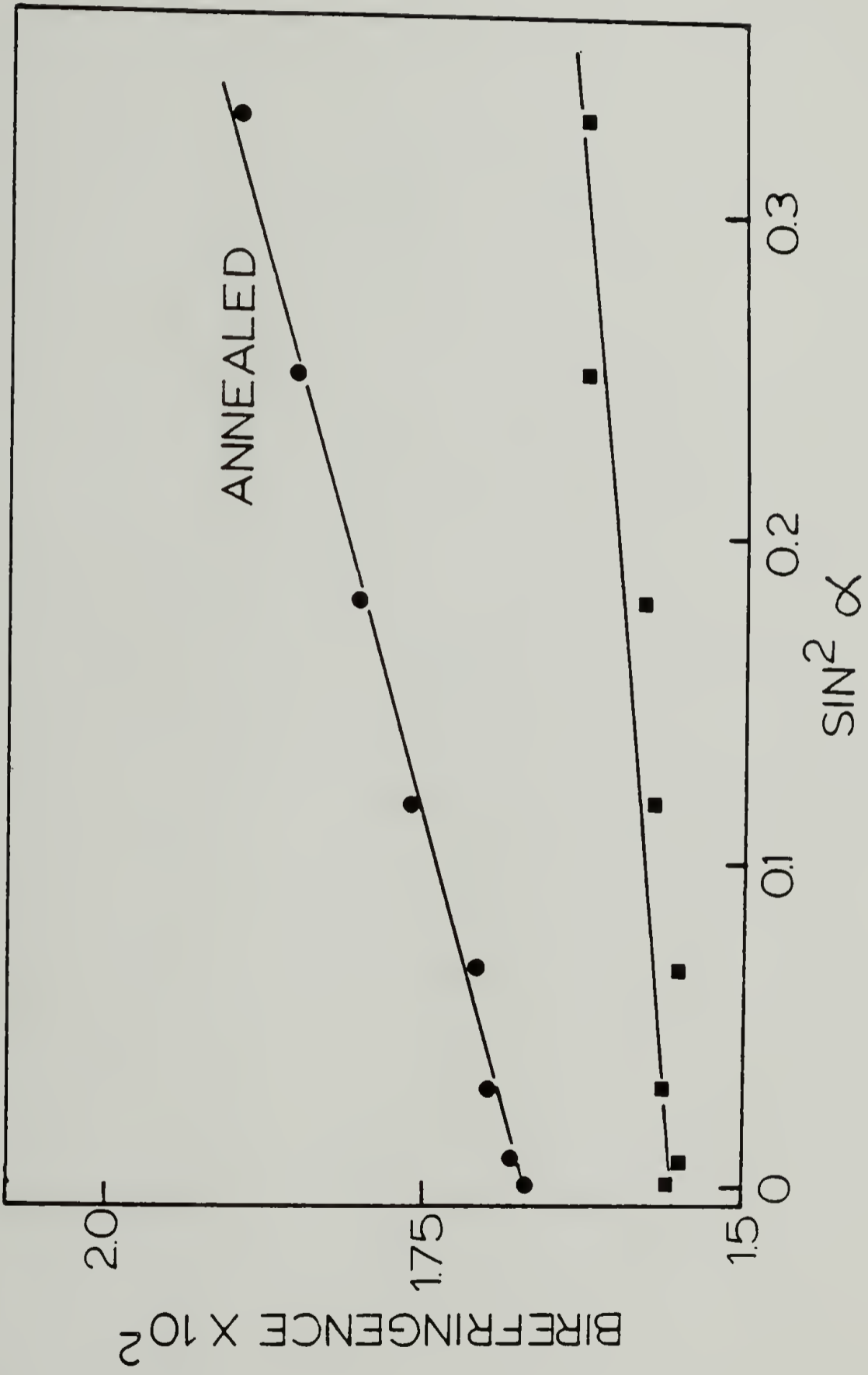


Figure 5.13(a)

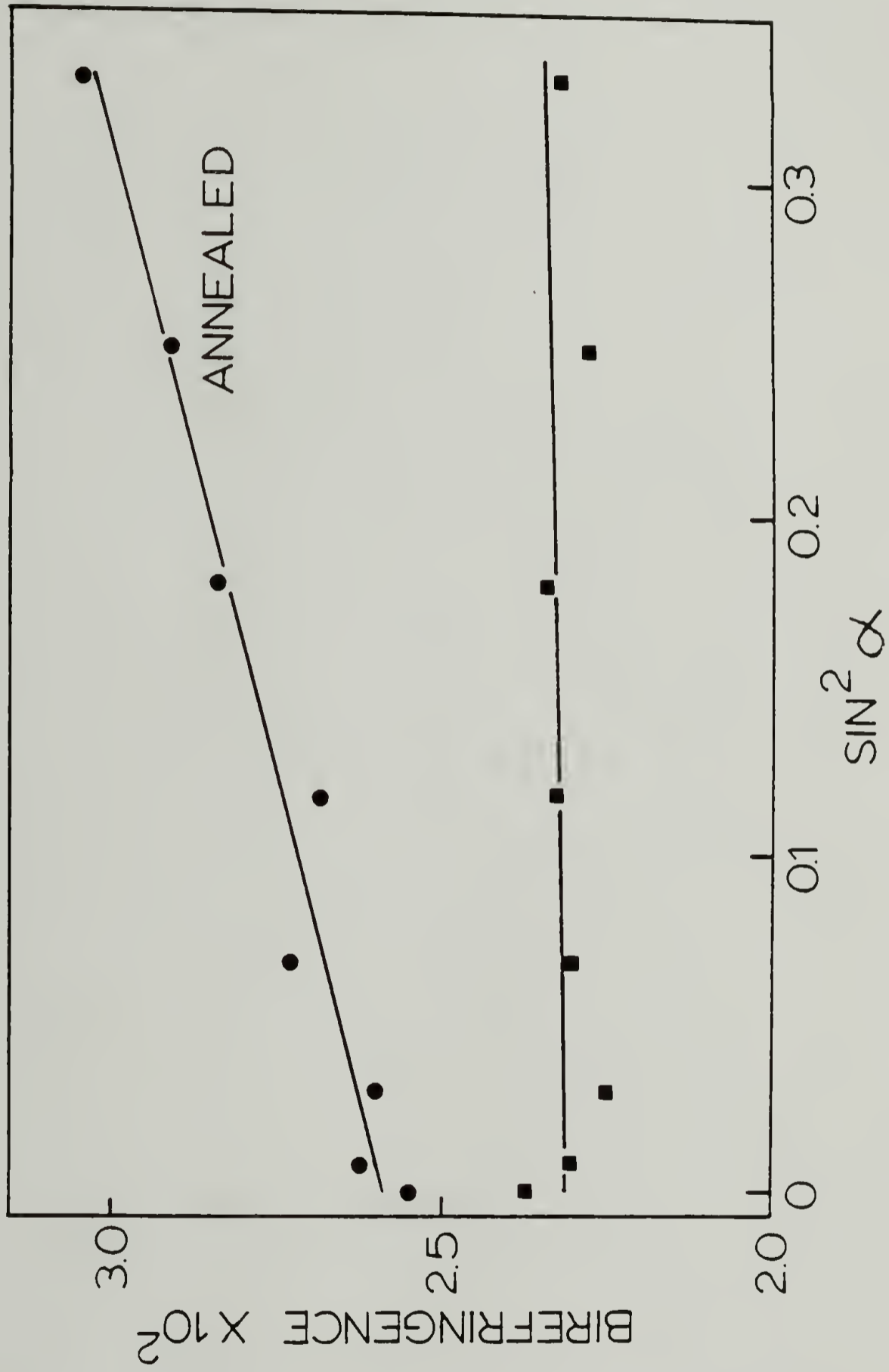


Figure 5.13(b)

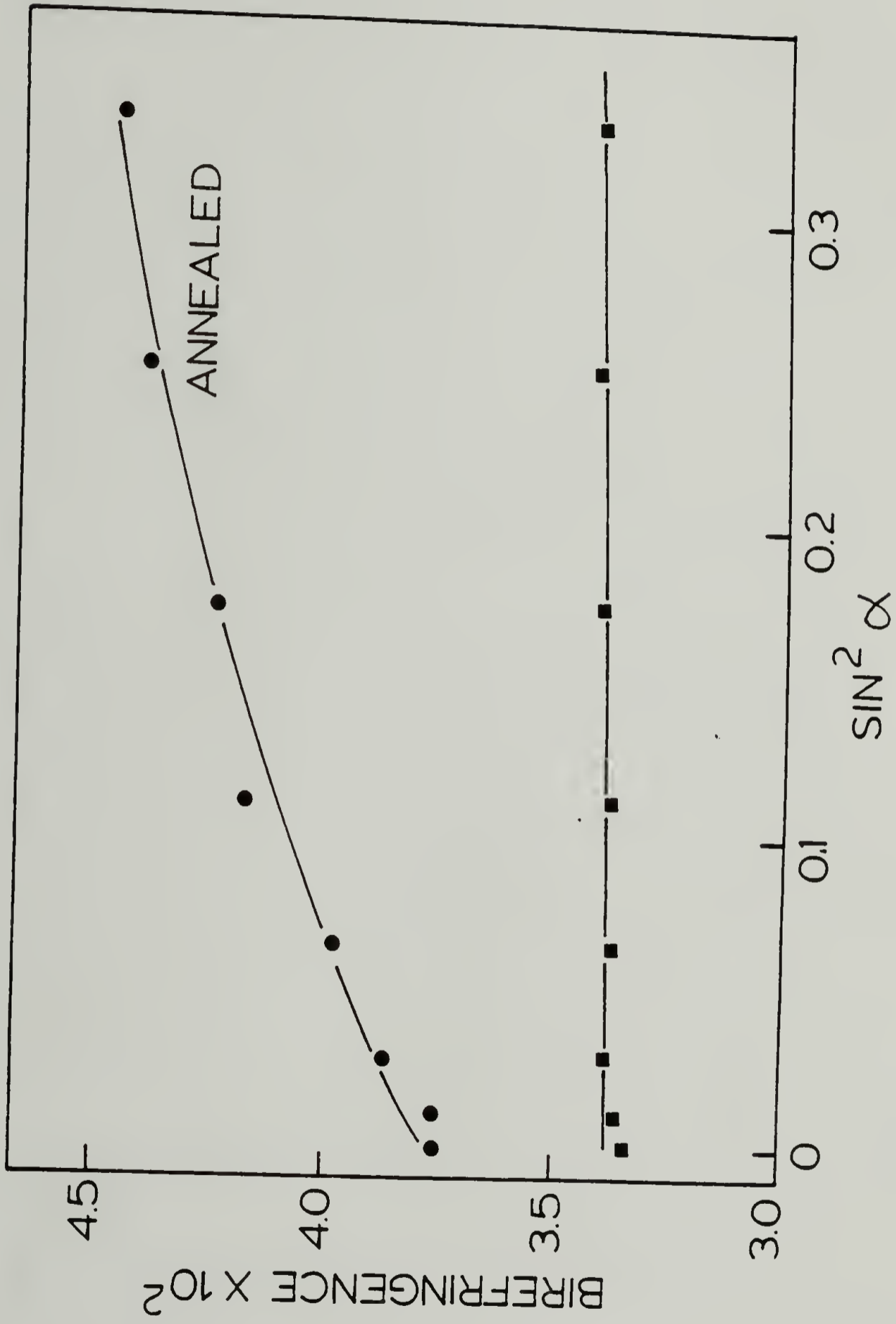


Figure 5.13(c)

extrapolation to $\sin^2 \alpha = 1$ gives the birefringence of the other axes pair [145]. Although the annealed 2.1X film shows a linear increase, it is uncertain that this can be extrapolated to imply biaxial orientation, especially since the annealed 3.7X film shows a non-linear increase. Therefore, reorientation on annealing produced a much more complicated overall orientation.

5.4 Conclusion

A Nylon 6 gel was prepared by cooling a 5 wt.% hot benzyl alcohol solution at room temperature. The gel showed syneresis and was thermally irreversible at heating and cooling rates of 2.5 and 10°C/min. However, after prolonged standing at room temperature, the gel was regenerated. A partially dried Nylon 6 gel film with 20% solvent deliberately left in it was drawn by co-extrusion with poly(oxyethylene) as the outer billet at 150° in an Instron rheometer up to a maximum draw of 5.7X. Tensile moduli developed were comparable to those obtained in a similarly drawn solvent-cast Nylon 6 film. The drawn gel film showed double orientation with one population of crystals oriented with chain axis in the draw direction. These crystals originated from the drawn fibrous morphology. The other crystal population had chain axis

perpendicular to the draw direction and were indentified as the fibrillar crystals that cause gelation. A deformation mechanism leading to this double orientation was proposed from the study of birefringence, WAXD and SAXS. Annealing at 190° C causes reorientation of the fibrillar crystals resulting in a more complex orientation.

C H A P T E R V I

A NEW DRAWING TECHNIQUE FOR NYLON 6 BY REVERSIBLE PLASTICIZATION WITH IODINE

6.1 Introduction

Of the important commercial thermoplastics, Nylon 6 is among the most difficult to draw to high ratio and tensile modulus. Generally, drawing processes result in a maximum draw of about 5. Comparing this to PE which can be drawn 250X leading to a remarkable reported tensile modulus of 222 GPa [3]. The highest reported modulus of drawn Nylon 6 is 14 GPa [6], only a small fraction of its calculated theoretical modulus of 262 GPa [2]. Nylon 6, however, has a high melting point of 225°C; a high modulus Nylon 6 would therefore potentially have a much wider temperature range applications than would a high modulus PE. An advancement in ultra-drawing Nylon 6 thus represents a challenge. Table 6.1 shows the moduli of Nylon 6 obtained to date by the various drawing and/or annealing methods.

The inability to ultra-draw Nylon 6 is largely due to the presence of interchain hydrogen bonds between adjacent

Table 6.1
Tensile Moduli of Nylon 6 Reported to-date Obtained
by the Indicated Methods

Modulus (GPa) As Drawn	Annealed	Draw Ratio	Method	Reference
13	-	12	NH ₃ Plasticization	Zachariades & Porter (158)
2.3	11.1	3	Zone Annealing	Kunugi et al. (189)
7	13	5	Nylon 6/4% LiCl Fiber Drawing	Acierno & Russo (6)
4.6	14	-	High Pressure Annealing of Fiber	Stamhuis & Pennings (190)

amide groups [158]. Hydrogen bond exists in both crystalline and amorphous regions and has an activation energy of ~ 8 kcal/mole. These act as quasi-crosslinks, inhibiting the sliding of chains during drawing. Drawing thus occurs mainly in the softer amorphous phase. With strain-induced crystallization, drawing is further restricted.

6.2 Drawing with Plasticization

Special processes have been developed to improve the ductility of Nylon 6 by destroying the interchain hydrogen bonds. Polar compounds of low volatility, eg. sulfonated esters, have been used as plasticizers in the drawing of commercial Nylon fibers [159]. These plasticizers interrupt the hydrogen bonds and depress both the glass and melting temperatures to facilitate processing. The presence of plasticizers in the final fiber is generally detrimental to its mechanical properties. Ideally, they should be removed after processing. Zachariades and Porter [160] developed the use of a reversible plasticizer to draw Nylons 6 and 11 by imbibing the polymers with anhydrous ammonia to compete for hydrogen bonds. The ammonia is vaporized after solid-state co-extrusion at below the Nylon melting point. Highly drawn Nylon 6 of

12X with tensile modulus of 13 GPa was reported. However, plasticization with ammonia occurred only in the amorphous phase [160], with crystals still inaccessible to drawing.

Wu and Black [162] plasticized Nylon 66 using dry HCl gas at dry ice temperature. Under these conditions, the plasticized Nylon 66 was rubbery and could be drawn easily to 11X. Degassing was carried out by heating the fiber or reacting it with dimethyl acetamide. The draw and yield stresses obtained were however an order of magnitude lower than the untreated yarn due to substantial amount of relaxation taking place during degassing.

Lithium salts have also been added to Nylon 6 by absorption [163], thermal fusion [164] or during polymerization [165] to form a lithium ligand with the carbonyl of the amide group, thereby interrupting the interchain hydrogen bond. The complex formed crosslink junctions resulting in an increase in melt viscosity and in this sense is not a true plasticizer. However, the reduction of its crystallization rate by the formation of the ligand allowed higher draw. The formation of the Nylon 6-Li complex enhances the modulus to 2.5 GPa even in the undrawn state. A high modulus of 14 GPa was reported for the drawn and annealed Nylon 6/Li salt spun filament [166].

In this chapter the reversible plasticization concept is pursued using iodine as a plasticizer for entry in both

amorphous and crystalline phases.

Nylon 6 is polymorphic and exists in several crystal forms, the most important of these are the α - and γ -crystals. Both have monoclinic unit cell structures with the difference in the direction of hydrogen bond between adjacent chains. The α -crystal has hydrogen bonds between antiparallel chains whereas the γ -crystal has bonds between parallel chains. The α -crystals can be transformed into γ -crystals when treated with iodine in potassium iodide solution and followed by iodine removal on titration with sodium thiosulfate [167]. The crystal transformation is complete in both undrawn and drawn Nylon 6, and without a loss of orientation [123]. This crystal transformation implies that the hydrogen bonds in both the amorphous and crystalline phases in the intermediate Nylon 6-I complex must be disrupted to allow chain rotation and mobility to generate the γ -crystals. With this as a basis, a method for drawing the Nylon 6-I complex is developed. The iodine acts as a reversible plasticizer and is removed after drawing by titration with sodium thiosulfate solution to generate the pure drawn Nylon 6 of controlled crystal forms.

6.3 Experimental

Nylon 6 film ($[\eta] = 1.04$ dl/g in 85% formic acid) was used as obtained from Dr. T. Kunugi of the University of Yamanashi, Japan. The film was $130\mu\text{m}$ thick: it was isotropic with no measurable birefringence and of γ -crystal form. It was found that both the α - and γ -Nylon 6 readily absorbed iodine and both complexes showed similar drawing behavior. The film was used as it is for the present study.

The complex was prepared by immersing the Nylon 6 film in a 1N KI_3 solution for 48 hours at room temperature. It was then air dried. Stress-strain measurements were made with an Instron tensile tester, equipped with environmental chamber, at strain rate 0.01 min^{-1} . Dynamic mechanical measurements were made using a Toyo Dynamic Viscoelastometer Model DDV-II.

Thermal analysis was studied using a Perkin-Elmer DSC-II equipped with a data acquisition station. For the Nylon 6-I complex, a stainless steel large volume capsule sealed with O-ring was used to contain volatilization of iodine during heating. Weight loss on heating up to 600°C was measured with a Perkin-Elmer Thermogravimetric Analyzer (TGA). Both were scanned with a heating rate of $20^\circ\text{C}/\text{min}$.

Gas evolved on pyrolysis of the complex at 250°C was trapped in carbon tetrachloride. The trapped species were identified with a Beckman UV-visible spectrometer. The

complex film was very dark and was too optically dense for UV-visible measurement. A partially washed, still brownish, complex film was used instead.

Wide-angle X-ray scan of the complex was obtained with a Siemens D-500 diffractometer equipped with scintillation counter, operating at 30 mA and 40 kV, and using a Cu K_α radiation with Ni filter. Scanning was made on the undrawn complex and at increasing elongation with a stretcher attachment in the diffractometer at room temperature.

Photographic techniques using a Statton flat film camera with 5 cm sample-to-film distance and a Weissenberg camera of 57.3 mm diameter were used to supplement the diffractometer data.

6.4 Results and Discussion

6.4.1 Mechanism of $\alpha \rightarrow \gamma$ Crystal Transformation

Although the transformation of α -crystal of Nylon 6 to the γ -form by treatment with aqueous KI_3 solution has been reported as early as 1958 [122], previous studies emphasized the determination of the newly found γ -crystal structure [124-128] and on the mechanism in which it is generated. The proposed mechanisms are reviewed since this new drawing technique is based on the chain mobility of the complex outlined in the mechanisms.

Frayner, Koenig and Lando [167] suggested from the structural arrangement of the α - and γ -Nylon 6 chains, that if the tight amide folds at the lamellar surface act as pivots and with alternating chains in the γ -form rotated 180° , the methylene groups will then match properly. If the amide groups are further twisted in proper direction to form hydrogen bond between parallel chains, a γ -structure will be obtained. Such a proposal involved large scale movement of the chains and the breaking and remaking of hydrogen bonds, however, it did not consider the role of iodine in the transformation.

Arimoto [168] proposed a mechanism involving iodine entering the crystalline region and coordinating with the oxygen of the amide group to form a complex. Such coordination destroys hydrogen bonds and the amide group is preferentially twisted out-of-plane with respect to the fiber axis. On removing iodine, hydrogen bonds form between the nearest amide groups in parallel chains giving a pleated sheet γ -structure.

An alternate mechanism involving I_3^- ion was proposed by Matsubara and Magill [169] from an infrared (IR) study of the complex. Their study also used N-methylacetamide-iodine complex as a model and led to the same conclusion as Doskocilova and Schneider [170] that the triiodide ion is coordinated to the nitrogen of the amide group with protonation of K^+ or H^+ ions at the

oxygen atom.

The above mechanisms were further reviewed by Abu-Isa [171] who found that when a thin Nylon 6 film is exposed to iodine vapor alone, the IR spectrum obtained is similar to that of the complex obtained from KI_3 solution treatment, except in the degree of severity. Complex formation with iodine vapor alone, though is possible, proceeds very slowly. This finding suggests that molecular iodine is capable of complex formation. We are not aware of further studies to substantiate whether molecular iodine or I_3^- ion is involved in the complex formation with Nylon 6.

Arimoto [172] also found that when non-polar solvent KI_3 solution is used, the amount of absorbed iodine was very much smaller than those in polar solvents at the same iodine concentration. Matsubara and Magill [169], however, found that the IR spectra was unaffected. It is well known that when iodine dissolves in a polar solvent, it complexes with the solvent to give a brown solution of I_3^- ions in equilibrium with I_2 , whereas it dissolves in non-polar solvent to give purple solution of molecular iodine [171]. From these studies of solvent effect, the ability of Nylon 6 to absorb strongly and to produce significant changes in the IR spectra only in a polar solvent indicates, though not conclusively, that I_3^- ion is largely responsible for the complex formation or its

presence kinetically favors iodine absorption.

Even though none of the above mechanisms are satisfactorily confirmed, it is certain that hydrogen bonds in both the crystalline and amorphous regions are interrupted and there is considerable chain mobility in the Nylon 6-I complex during the transformation. Using this idea, a new reversible plasticization method of drawing Nylon 6, with the possible unravelling of chains from previously inaccessible crystalline regions may be developed to give high draw ratio. Iodine can then be removed by reacting with sodium thiosulfate solution. The temperature and solvent used in the reaction determine the type of crystal, α - or γ - formed finally [173]. Using water/ethylene glycol mixture at below 35°C, γ -crystal is obtained. Above 50°C, α -crystals are formed, whereas between 35-50°C, a mixture of both crystals is reported. The reaction condition can thus be used to control the type of crystals desired in the drawn Nylon 6.

6.4.2 Stoichiometry of Nylon 6-I Complex

Many polymers formed complex with iodine. The most important of these are: polyvinyl alcohol which complexed with iodine as the first commercial polarizer [174]; starch forms complex with iodine which fits exactly inside its helical coil to give a blue color as an indicator for titration [175]; poly(vinyl pyrrolidone)-I complex [176] is

another important complex used as blood substitute; more recently, the active research in semi-conducting polymers studied iodine-doped polyacetylene [177]. There were numerous studies on the stoichiometry of these polymer-iodine complexes. However, it is difficult to draw any specific conclusion as the reported stoichiometry varies widely. Even the most studied starch-I complex had become a part of the non-stoichiometry chemistry. Another problem is the positive identification of the complexing species.

Polyiodide was suggested to be the species forming complex with poly(vinyl alcohol), however, calculation by Stein and Rundle [178] showed that the complexing species was molecular iodine polarized by the polymer and arranged linearly rather than a covalently bonded polyiodide. Cournoyer [176] studied extensively poly(vinyl pyrrolidone)-I complex and gave a general stoichiometric formula: $PVP-(I_2)_x (IO^-, I^-)_y$, where the ratio $y/x < 1.5$ depending on the synthesis. This stoichiometry has three complexing species of iodine, iodide and hypiodite. In iodine-doped polyacetylene, the main dopants are I_3^- and I_5^- ions with variable stoichiometry, (CHI_y) , where $y = 0.1-0.3$.

For Nylon 6-I complex, there were fewer studies of the nature of the complex itself. The interest in the past was on the δ -crystal structure generated. There were

conflicting ideas on whether the complexing species is molecular iodine or I_3^- . This problem is reexamined in the present study. There was undoubtedly the presence of molecular iodine in the complex from the present pyrolysis and UV-visible spectroscopic study. The complex stained when it came in contact with another object. There are probably excess iodine absorbed, not participating in the complex formation and therefore are mobile for migration causing staining.

The Nylon 6-I complex film was very dark and too optically dense for UV-visible spectroscopy. The film was partially washed with deionised water to a light brown film and dried. Fig. 6.1 shows the UV-visible spectra obtained. Two strong absorption maxima occurs at 290 and 356 nm which are characteristic of I_3^- ion [179]. Magnification of the spectra at 500-600 nm region shows a very weak shoulder at ~530 nm of iodine. Raman spectroscopy also showed absorption of the asymmetric I_3^- peak at 108 cm^{-1} [180]. A very weak peak at 162 cm^{-1} could be observed, which fell within the I_5^- $155-165\text{ cm}^{-1}$ Raman band for starch- and poly(vinyl alcohol)-I complexes. The presence of this band suggests that some of the iodine present could complex with I_3^- to give I_5^- .

When the Nylon 6 film was immersed in KI_3 solution, it turned dark immediately with noticeable swelling. It was reported in a $5\mu\text{m}$ thick film, formation of complex

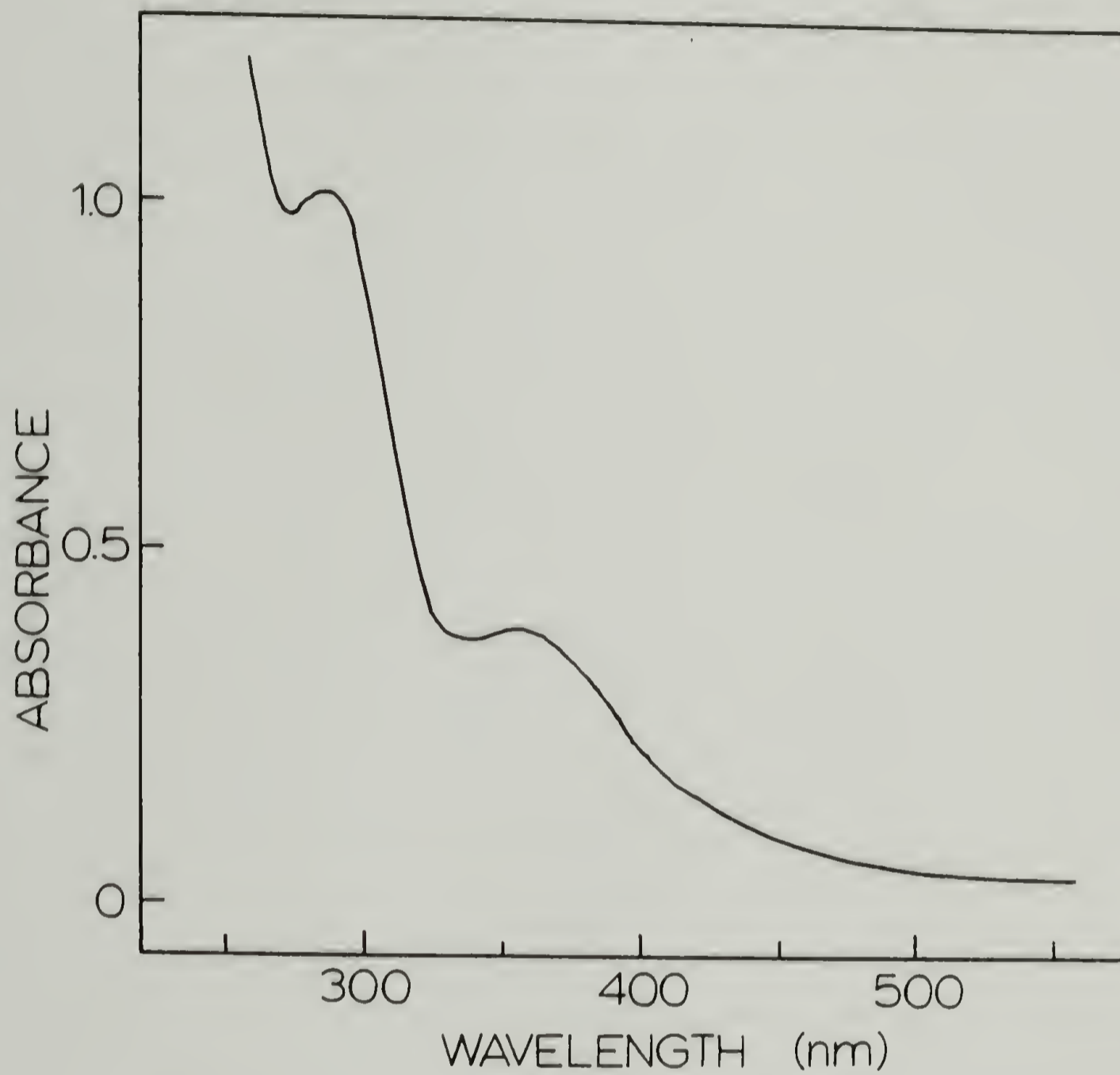


Figure 6.1. UV-visible spectra of a Nylon 6-I complex film partially washed with water.

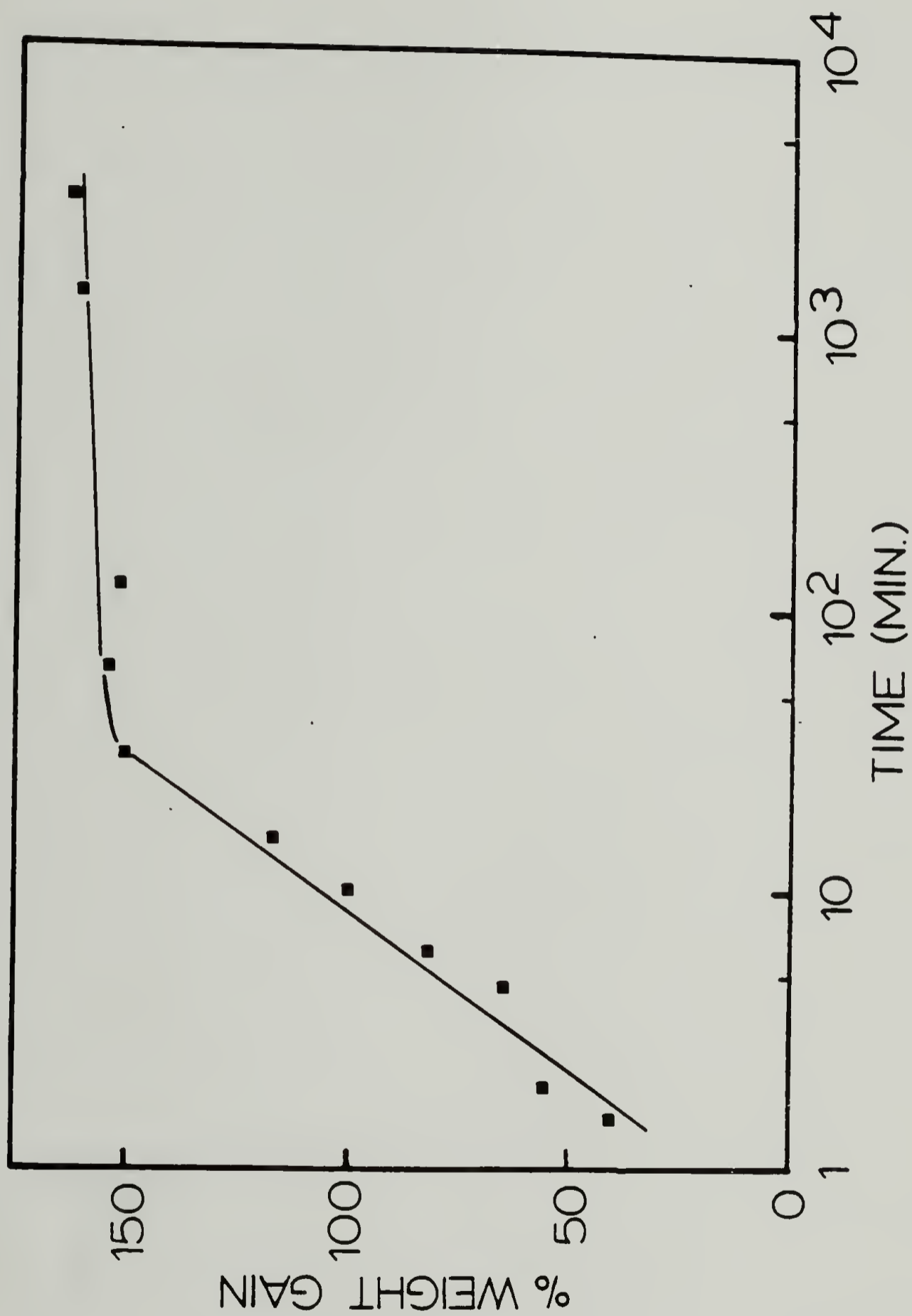
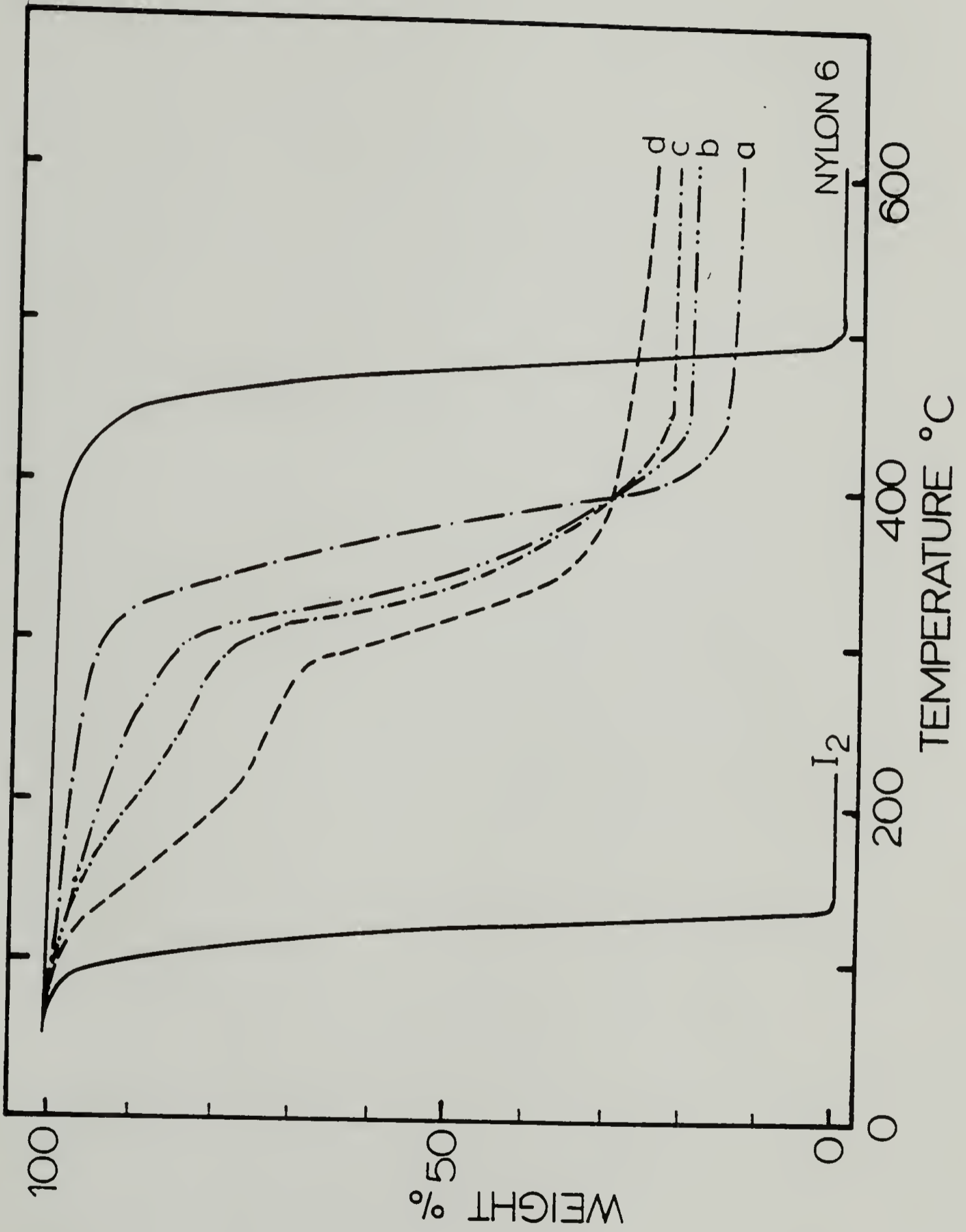


Figure 6.2. % Weight gain of Nylon 6 after immersion in 1N KI_3 aqueous solution as a function of time.

Figure 6.3. Thermal gravimetric analysis of Nylon 6-I complex with increasing amount of absorbed chemical species after immersion in KI_3 solution, (a) 28.7, (b) 51.8, (c) 57.5 and (d) 62.6%.



was complete in <30 sec as observed from the shift of the IR -NH 3300 cm^{-1} band [171]. Fig. 6.2 shows the % weight gain as a function of time when a 130 μ thick Nylon 6 film was immersed in a 1 N aqueous KI_3 solution. Weight gain increased rapidly to ~165% after 1 hr treatment. Weight gain was reported to depend on both the concentration and the solvent of the KI_3 solution [172]. There is a critical concentration, 0.1 mol/l for aqueous KI_3 solution, below which absorption was slow and equilibrium weight gain was <30%. Above 0.2 mol/l, the effect levelled off and further increase in concentration did not produce significant change in equilibrium weight gain. At any equivalent concentration, Nylon 6 absorbed more in a polar solvent than in a non-polar solvent.

Table 6.2 shows the dimensional changes on swelling and after drying of the complex. On absorption, the film swelled with the most prominent increase in thickness, 58.1%. The length and width swelled to a much lesser extent with the total volume increase of 94.5%. On drying, the length and width recovered to near original dimensions but there was still ~30% increase in thickness.

Weight loss of the complex on heating in a TGA is shown in Fig. 6.3. Both weight loss of pure iodine crystals and the untreated Nylon 6 film are included for comparison. Iodine crystals sublimed at $\sim 50^\circ$ and is completely volatilized at 130°C . The Nylon 6 film showed

thermal stability up to 370°C and lost weight rapidly on further heating, turning to ash at 500°C. The Nylon 6-I complex showed two temperature zones of weight loss. The two zones are not well developed when the % absorption of iodine is small, <29%, but become more distinct when % absorption increases. The first temperature zone occurred between 70 and 320°C. For the complex with 28.7% absorption, weight loss began at 70°C and continued gradually in this temperature zone until 320°C, where zone 2 began with a sharp loss in weight. It levelled off at ~400°C with a total loss of 84.4% which is more than the initial % absorption. Therefore, the bulk of weight loss in zone 2 must include Nylon 6. The degradation temperature of Nylon 6 is lowered, likely due to the interruption of the interchain hydrogen bonds. With increasing % absorption, the % weight loss in zone 1 increases and reached a limit of ~30%. There is also a gradual shift in the onset of zone 2 temperature to a slightly lower temperature of 300°C, and a decrease in total weight loss as tabulated in Table 6.3.

Pyrolysis of the complex was carried out at 250°C, zone 1 of the TGA curve. The gas evolved was trapped with a non-polar solvent of carbon tetrachloride which turned purple. Fig. 6.4 shows the UV-visible spectra of the solution with a broad maxima at 525 nm characteristic of molecular iodine. No absorption maxima of I_3^- was

detected. It was therefore concluded that weight loss in zone 1 is due to iodine alone. The amount of iodine absorbed in this zone at equilibrium is high, 29.8%, almost half of what is being absorbed.

If weight loss in zone 1 is from the molecular iodine; weight loss in zone 2 is from the complexed I_3^- ion and the remainder at high temperature zone above 500° is KI_3 salt, from mass balance, the stoichiometry of the Nylon 6-I complex is $(\text{Nylon } 6)(I_3^-)_{0.24}(I_2)_{0.35}$ at the equilibrium absorption. The amount of K^+ ion in this stoichiometry is calculated to be 3.05% by weight. Microanalysis of the complex from atomic absorption gave the K^+ ion content of 4.4%, which is reasonably close to calculation. Furthermore, the amount of KI_3 in this stoichiometry is 31%, residue in TGA at high temperature is a close 29%.

From the above studies, it is most probable that I_3^- is the main species involved in the complex formation. Molecular iodine which is in equilibrium with I_3^- in the aqueous KI_3 solution is absorbed at the same time. Some may have complexed with I_3^- to give I_5^- or participated in the Nylon 6-I complex formation as shown by the weak 530 cm^{-1} shoulder in UV-visible spectra. The majority absorbed do not form complex and can be easily removed by washing with water or on pyrolysis at a low temperature of 100°C .

Table 6.2

Dimensional Changes in Nylon 6 Film on Absorption
in KI_3 Solution

	Percent Increase	
	After 48 hr. Immersion	After Drying
Length	10.0	-1.3
Width	14.0	2.1
Thickness	58.1	29.6
Volume	94.1	27.5

Table 6.3

Weight Loss of Nylon 6-I Complex on Heating
in a Thermal Gravimetric Analyser

(1) Absorption wt. %	(2) Total Loss wt. %	(3) Zone 1 % Loss	(4) Zone 2 % Loss	(1)-(3)
28.7	84.4	6.5	78.3	22.2
36.3	84.0	9.0	75.0	27.3
45.0	80.0	12.0	68.0	33.0
51.8	77.5	14.5	63.0	37.3
57.5	76.5	21.5	55.0	36.0
61.7	75.5	29.0	46.5	32.7
62.6	71.0	29.8	41.2	32.8

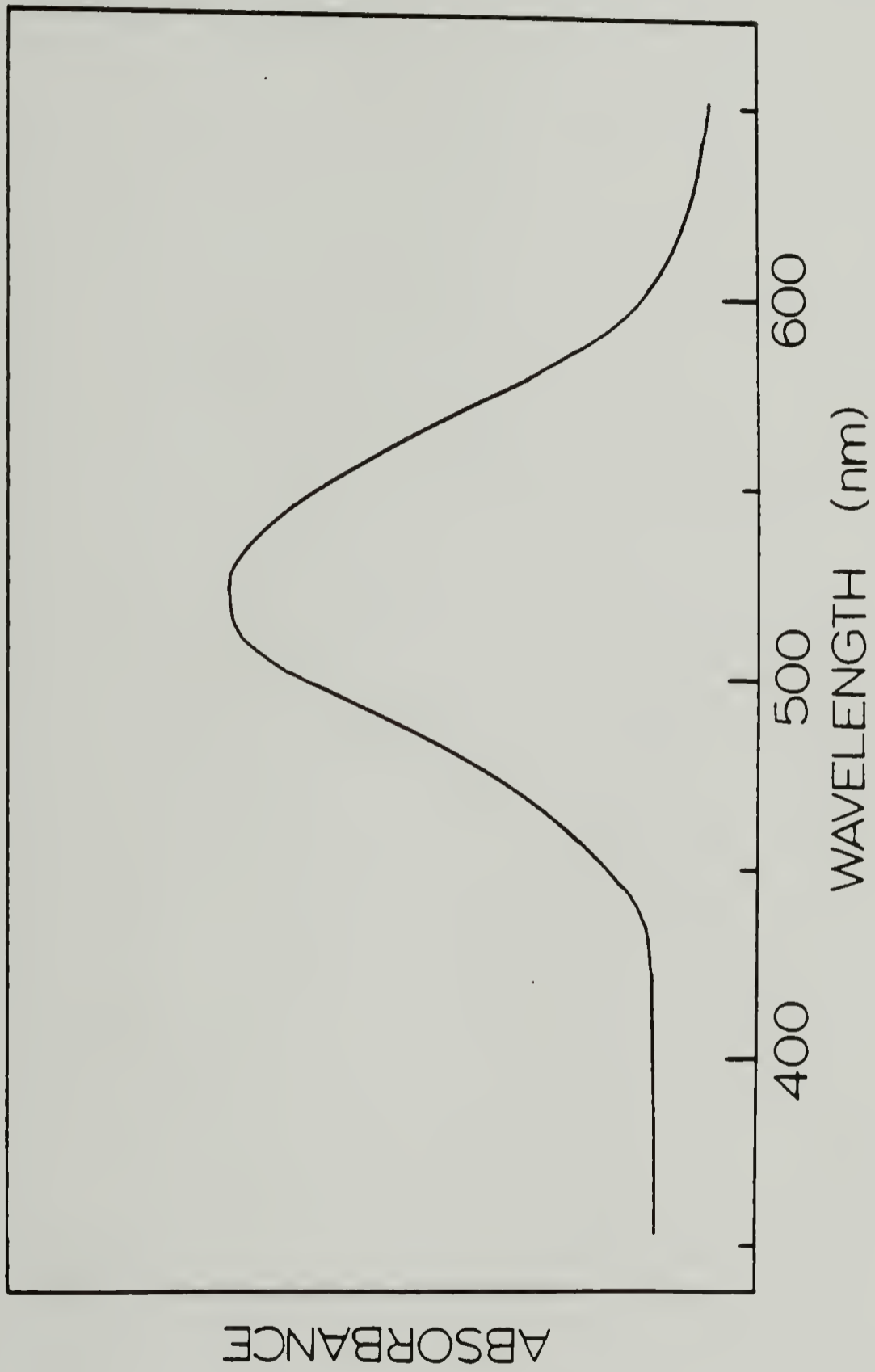


Figure 6.4. UV-visible spectra of trapped evolved gas in CCl_4 on pyrolysis of Nylon 6-I complex at 250°C .

6.4.3 Drawing and Mechanical Properties

The wet complex film immediately after treatment in aqueous KI_3 solution is swollen and soft. It can be easily stretched by hand and shows necking. A stress-strain curve of such film tested with an Instron tensile tester at room temperature is shown in Fig. 6.5. It has a very low yield stress of 5 MPa and necks at 20% elongation. It strain hardens on further stretching and breaks at 550% elongation with a strength of 16 MPa. It is remarkable to note that complexing with iodine changes drastically the drawing behavior of Nylon 6 to a rubbery intermediate complex. A stretched, wet film, on releasing the load, will retract slightly from elastic recovery and contraction from deswelling on solvent evaporation.

A dried complex film is however very much stiffer. To help determine the temperature range for effective drawing, dynamic mechanical properties were measured with a Rheovibron at three different frequencies of 11, 35 and 110 Hz. Plots of dynamic mechanical loss $\tan \delta$ results are shown in Fig. 6.6. The curves at 35 and 110 Hz are displaced vertically for visualization. Two loss peaks are found for the complex. A small peak occurs at $\sim 40^\circ\text{C}$, its maxima does not shift appreciably with change of frequency. The second loss peak is of much higher magnitude, with maximum $\tan \delta$ of 0.2. The maxima occurs at 41°C at 11 Hz, increasing to 53°C at 110 Hz. Up to

60°C, the results are reversible, however, above 80°C, the complex shows irreversible viscous flow.

In an untreated γ -Nylon 6, dynamic mechanical study gives three relaxation peaks [181]. The highest α -relaxation is the glass transition, T_g , which is 80-90°C. T_g of Nylon 6 is strongly influenced by the presence of water which can drastically reduced it. β -relaxation occurs at $\sim -40^\circ\text{C}$ and is associated with the presence of water. Its magnitude decreases when water content in Nylon 6 is reduced. The γ -relaxation of crankshaft motion of the methylene chains in the amorphous phase at $\sim -120^\circ\text{C}$ is, however, not observed for the complex. Thus, comparing the dynamic mechanical properties of the complex with that of γ -Nylon 6, the relaxation temperature at 41°C of the complex must be the α -relaxation which has been depressed by the plasticizing effect of iodine and the presence of some water as is evidenced from the appearance of a small β -relaxation peak at -40°C . The α -relaxation of the complex is also detected in a DSC which shows prominent second order transition at a lower temperature of 32.5°C, Fig. 6.7. Above 40.°C, iodine sublimed giving an endotherm which formed a continuation of the second order transition.

From the maxima of $\tan \delta$ curves, $\log f$ (frequency) is plotted against the reciprocal relaxation temperature,

$1/T$, Fig. 6.8 to give the Arrhenius activation energy ΔH_a of 17 kcal/mole. Kunugi [182] found from the stress relaxation of oriented Nylon 6, the Arrhenius plots of shift factor were represented by two straight lines having a break point at 80-110°C, corresponding to the temperature of the breakdown of interchain hydrogen bonds in the amorphous region. ΔH_a above this temperature range was 17 and 33 kcal/mole for Nylon 6 drawn 3 and 4 fold respectively. A value of 34 kcal/mole was also reported by Hoashi and Andrew [181]. The measured ΔH_a for the complex is low compared to the reported values. This low ΔH_a implies greater molecular chain mobility. By analogy, this must be resulting from the plasticizing effect of iodine with the interruption of intermolecular hydrogen bonds.

Fig. 6.9 shows the stress-strain curves of Nylon 6 and its iodine complex at temperatures below and above the α -relaxation. The solid lines are Nylon 6 which shows high yield stress of 55 MPa and breaks at 180% elongation at room temperature. Increasing the draw temperature to 55°C lowered the yield stress but did not increase the elongation at break appreciably. At room temperature, the yield stress of the complex is comparatively low, 24 MPa, and decreases with increasing temperature. At 55°C, the complex shows rubbery behavior and elongates to 790% before breaking. This is a much higher draw than possible

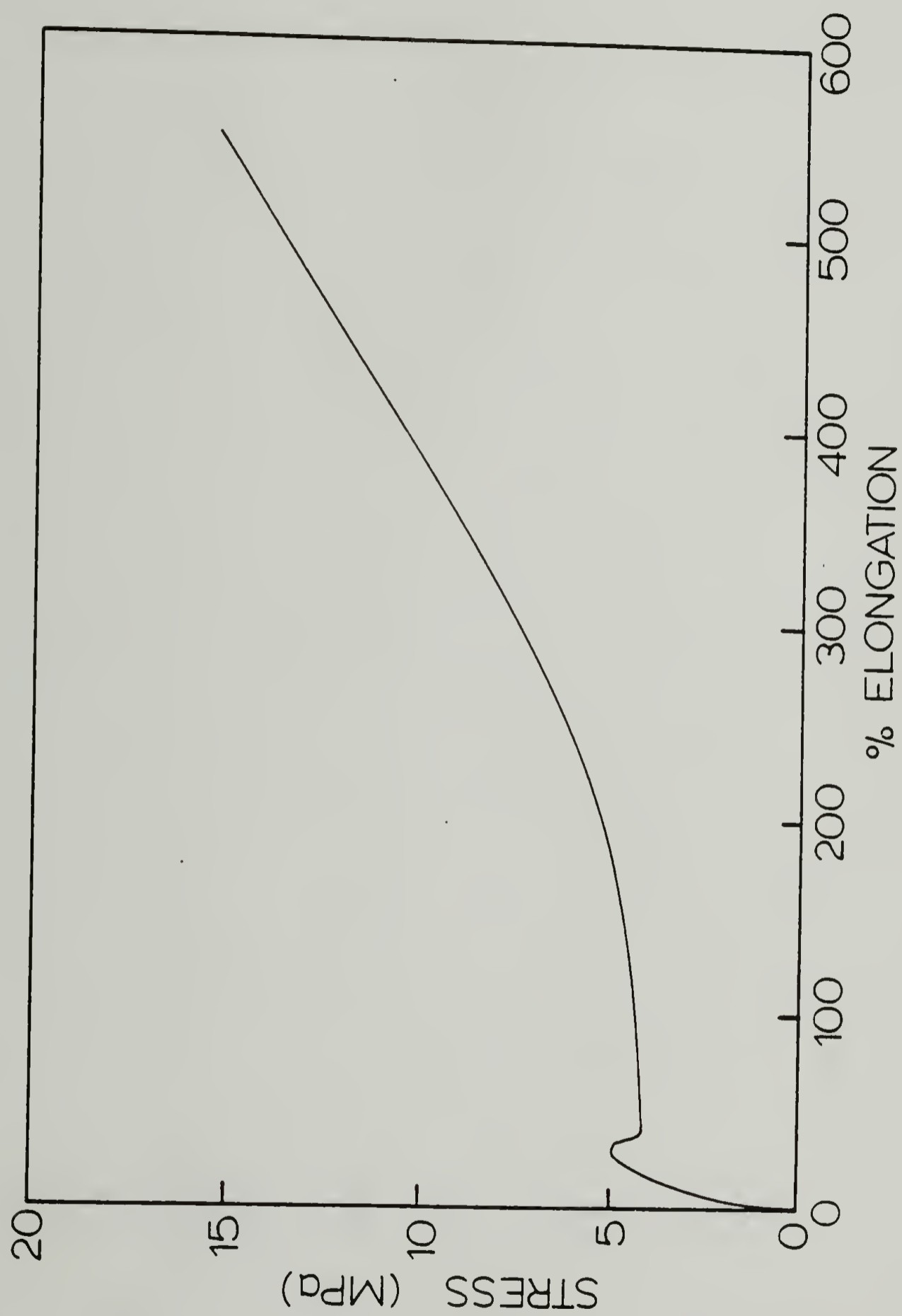


Figure 6.5. Stress-strain curve of a wet Nylon 6-I complex film, tested immediately after immersing in a 1N aqueous KI_3 solution for 48 hours.

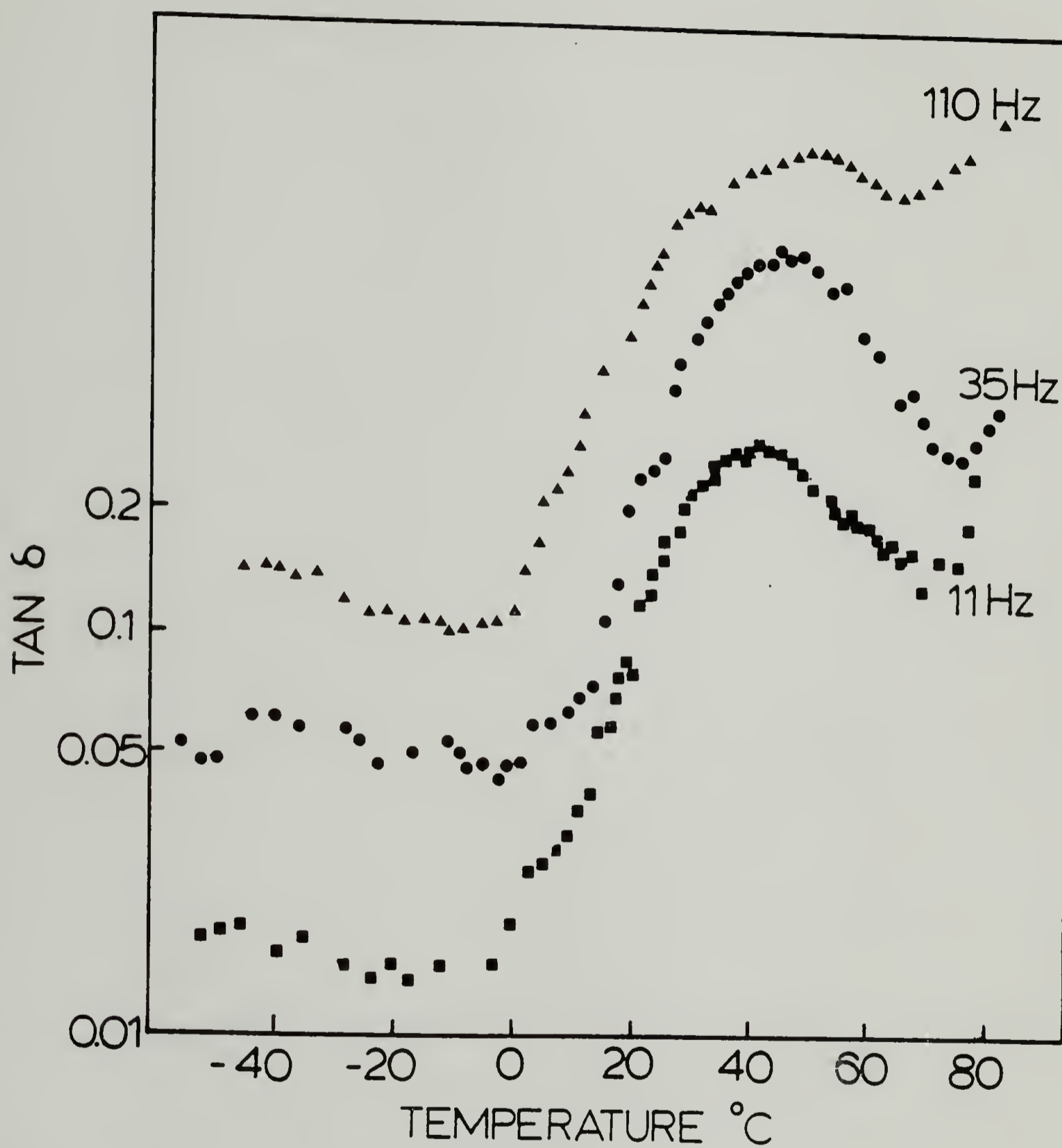


Figure 6.6. Loss factor $\tan \delta$ for undrawn Nylon 6-I complexes at frequencies 11, 35 and 110 Hz.

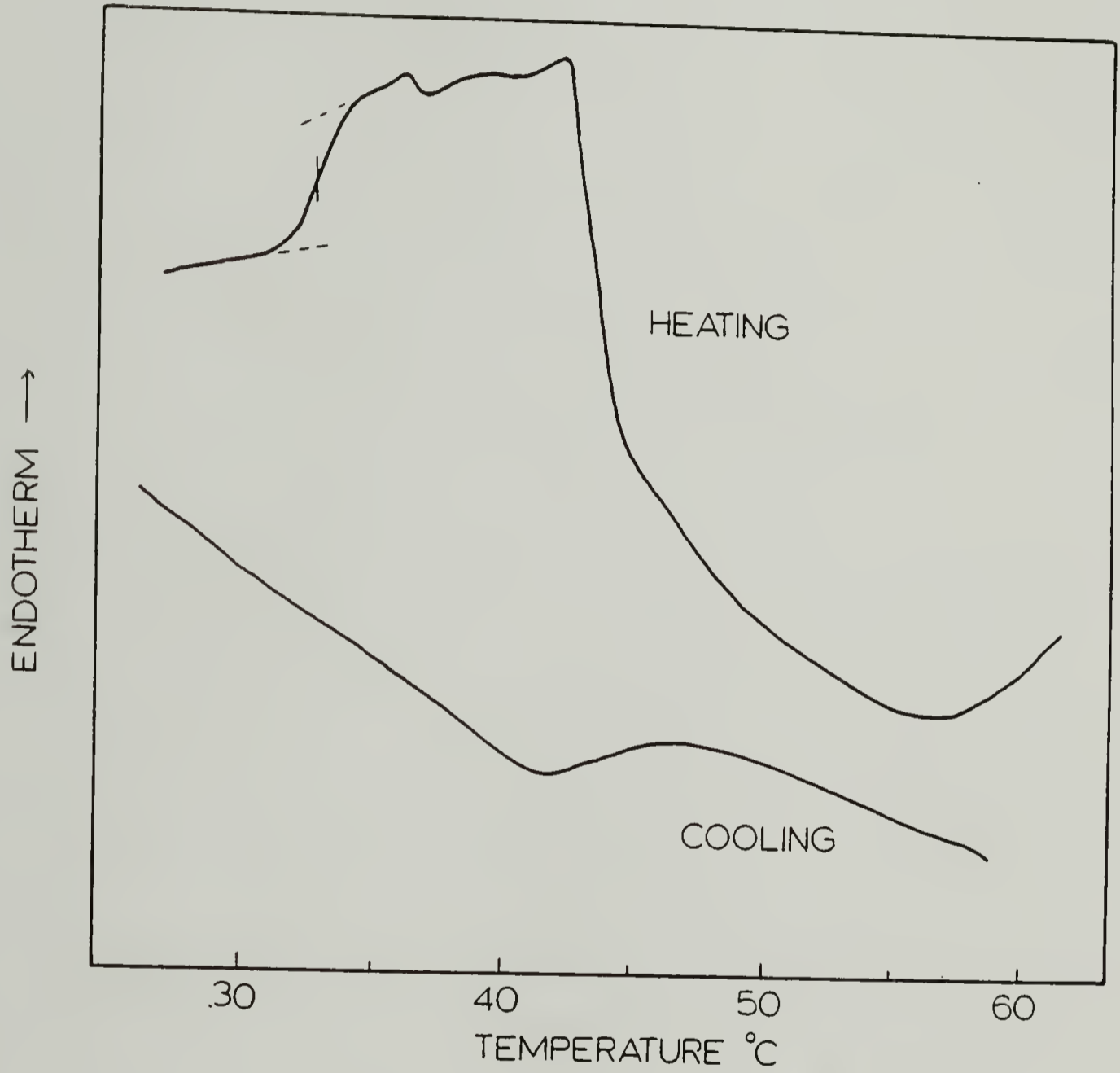


Figure 6.7. DSC scans on heating and cooling the Nylon 6-I complex at 20° C/min.

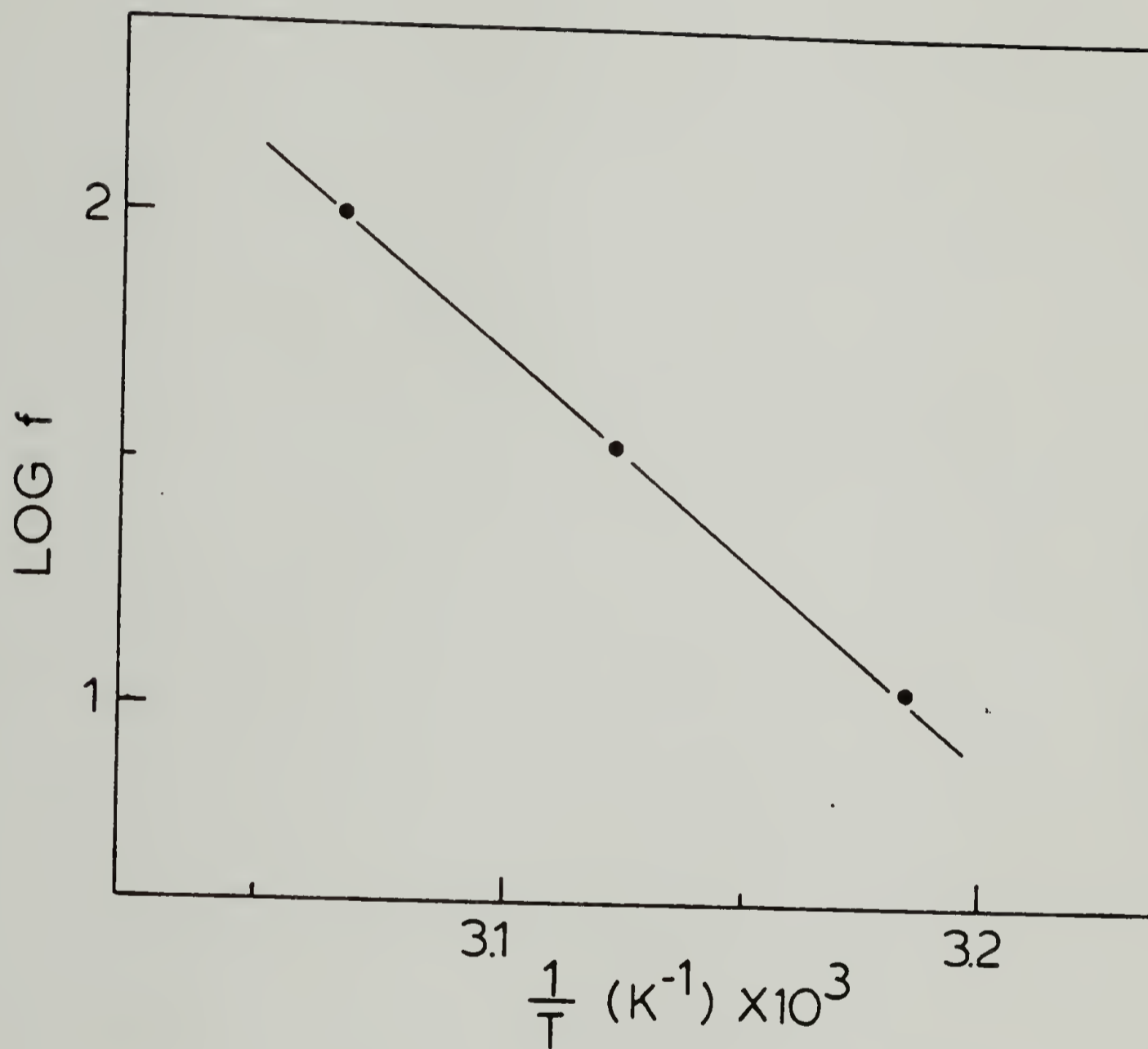


Figure 6.8. Arrhenius plot of Log f (frequency) vs. $1/T$ for undrawn Nylon 6-I complex.

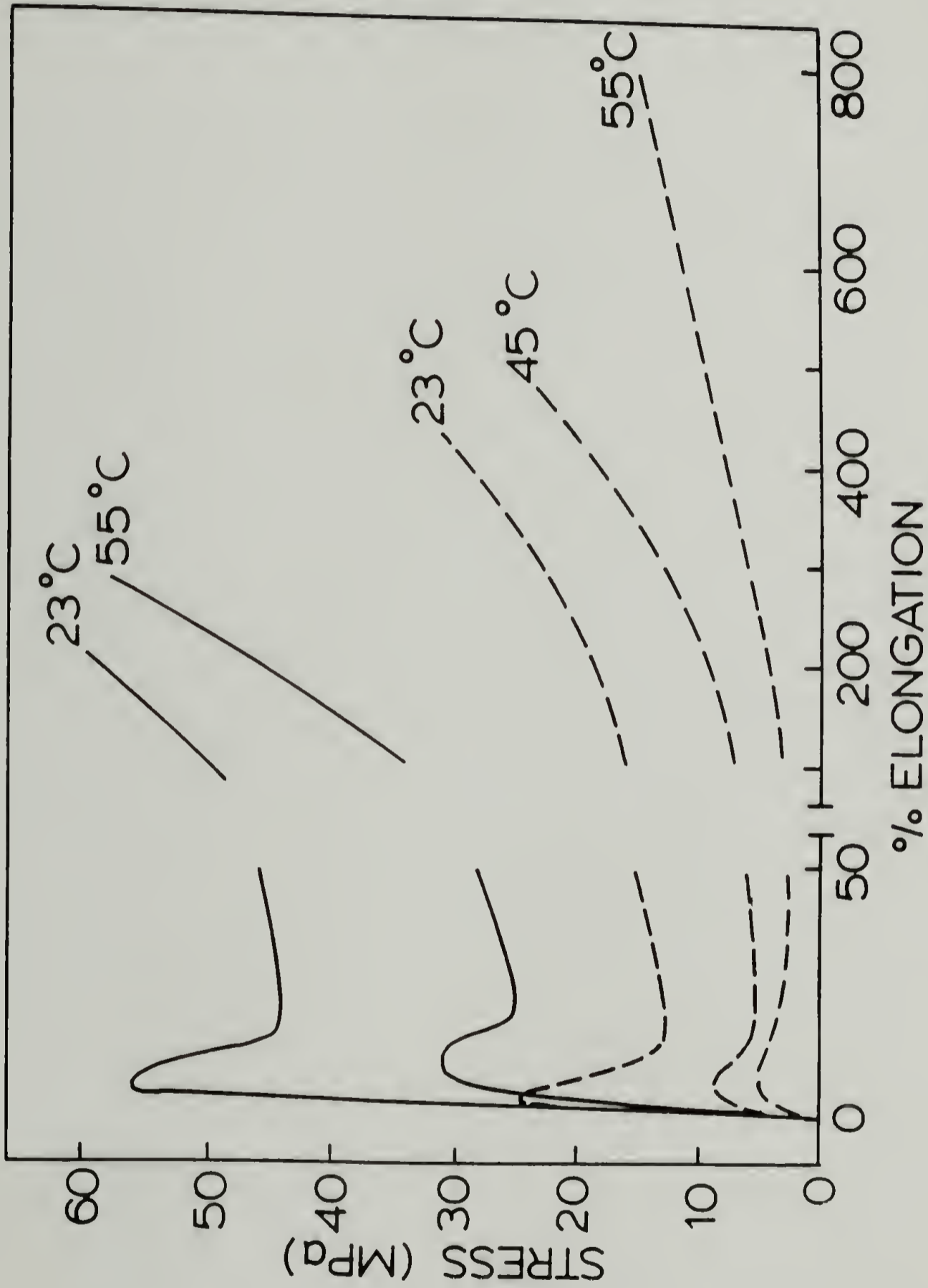


Figure 6.9. Stress-strain curves for γ -Nylon 6 (solid lines) and Nylon 6-I complex (broken lines) at temperatures below and above the α -relaxation of the complex.

Table 6.4

Properties of Drawn δ -Nylon 6 After Removal of Iodine
with Sodium Thiosulfate Solution at Room Temperature

Draw Temperature	Draw Ratio	Tensile Modulus (GPa)	% Crystallinity	Orientation Function, f_c
23	3.5	3.4	42.2	-
23	4.0	3.9	44.9	0.978
23	4.5	4.1	43.3	0.984
23	5.3	4.5	44.3	0.987
55	7.5	6.0	53.9	0.985

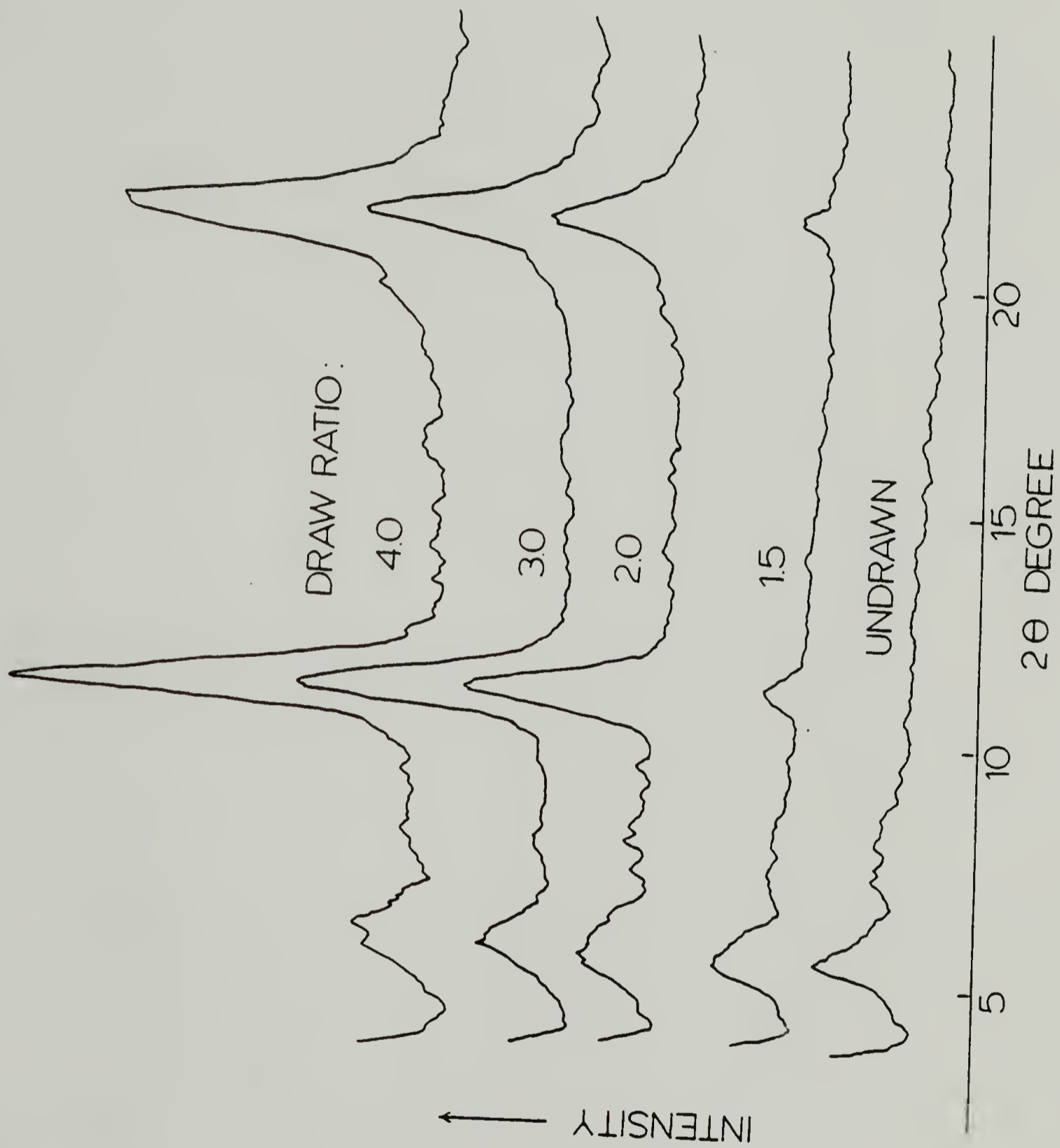
for an untreated Nylon 6. Drawing behavior at 55°C is very similar to drawing of the wet complex at room temperature (Fig. 6.5) except in the higher elongation at break. Thus the presence of water provides an additional plasticizing effect. Above 80°C, the complex exhibits viscous flow, although it could be easily stretched up to 14X, drawing does not produce significant orientation.

Table 6.4 lists the modulus, % crystallinity from DSC and crystal orientation function, f_c obtained from complex drawn and washed under fixed length with sodium thiosulfate solution at room temperature. Removal of iodine under this condition gives γ -crystal. The orientation function was obtained from the aximuthal scan of the (020) reflection in a wide-angle X-ray diffractometer. Orientation produced is high with $f_c > 0.978$. For a perfect orientation, $f_c = 1$. For drawing at room temperature, draw ratio and modulus obtained are comparable to reported values from drawing at elevated temperature. Drawing at 55°C gives higher draw of 7.5 X with relatively high modulus of 6.0 GPa. % crystallinity in all cases increases by 15-27% from the 27% crystallinity of initial untreated Nylon 6.

6.4.4 X-Ray Diffraction Studies

Wide-angle X-ray diffractometer scan of the undrawn complex is shown in Fig. 6.10. A single weak, broad new

Figure 6.10. WAXD scans of an undrawn Nylon 6-1 complex and at increasing draw ratio at room temperature.



peak at $2\theta = 5.3^\circ$ (d-spacing = 1.67 nm) is obtained. This new peak is observed for the complex regardless of the starting Nylon 6 being α - or γ -form. In α -Nylon 6, strong (200) and (002 +202) diffraction occurs at $2\theta = 20.2$ and 24.0° respectively, and γ -Nylon 6 has (200) and (002) diffractions at $2\theta = 21.8$ and 22.7° respectively. All these crystalline peaks are absent in the complex and is proof for the disruption of crystallinity by iodine or I_3^- ion which seems to enter into both the amorphous and crystalline phases, likely due to the ability to complex with the amide groups as a driving force.

On drawing the complex, weak diffraction peaks appear at $2\theta = 11.43^\circ$ and 22.93° . Neither of these two new peaks are related to the crystalline peaks of the parent Nylon 6. Their intensities increase with drawing, becoming very strong at draw ratio 4. The low angle peak at $2\theta = 5.3^\circ$ also shifts slightly to a higher angle of 5.6° . The appearance of these new diffraction peaks is unique for the Nylon 6-I complex, whether an initially α - or γ -Nylon 6 is used. Thus the complex has a unique structure of its own. From the d-spacings, the 22.93° peak is a second order diffraction of the 11.43° peak. This diffraction has also been observed for both iodine-doped cis- or trans-polyacethylene and is characteristic of iodination [180]. The spacing was found to be reasonably close to the sum of the spacings of the

most intense diffractions in the precursor polyacetylene and the van der Waals diameter of iodine, and was suggested to be the interplanar spacing between iodine layer separated by a close-packed plane of polyacetylene. However, we observe more diffractions for the drawn Nylon 6-I complex to index differently.

The appearance of the low angle peak in the undrawn complex at $2\theta = 5.3^\circ$ is significant. It has a d-spacing of 1.67 nm and provides intermolecular chain information without going into a more detailed radial distribution function. Taking the van der Waal radii of the methylene groups in the Nylon 6 chain as 0.20 nm, and the van der Waals radius of iodine or ionic radius of I_3^- as 0.215 nm [183], the packing of iodine between Nylon 6 chains give a dimension of 0.84 nm. If this is repeated at the next adjacent chain, the total dimension would be 1.66 nm, close to the observed d-spacing. An alternating arrangement of iodine or I_3^- and Nylon 6 chains can be surmised.

Intercalation of iodine or I_3^- ion between chains would most likely have occurred between the hydrogen bond planes. For a α -Nylon 6, this is the (001) plane with c-axis 0.801 nm, for γ -Nylon 6, this plane is (100) and a-axis is 0.933 nm. When iodine or I_3^- ions are intercalated between the hydrogen bond planes, the c-axis of α -Nylon 6 will expand to 1.661 nm and the a-axis of the

δ -Nylon 6 will expand to 1.793 nm. The first dimension is close to the observed d-spacing while the latter is greater by 0.123 nm. The γ -Nylon 6 structure is not as closely packed, with packing density of 0.707 compared to 0.75 for the α -crystal [42]. Since the same d-spacings are observed for both their complexes and therefore possibly same complex structure, the complexing of iodine or I_3^- ion with the γ -Nylon 6 amide groups could cause closer packing and a slight reduction in the van der Waal radii, and therefore a smaller dimension for the expanded a-axis as would be expected from simple addition. Therefore intercalation between the hydrogen bond planes is very likely in the complex formation. Since there is only one weak reflection indicating lateral packing of iodine alternating between Nylon 6 chains, the undrawn complex has a mesomorphic structure.

Fig. 6.11 shows the rotation photograph of a complex drawn 4X. Three layer lines are found with a fiber identity period of 0.833 nm. This is almost half the repeat distance in the unit cell chain axis and therefore equivalent to one monomer unit. Using standard bond angles and distances, a fully extended planar ziz-zag Nylon 6 monomer unit is 0.87 nm. Rotation of the amide group about the C'-C bond in -C'-CO-NH- out-of-plane by 69° gives this observed identity period. This rotation is 2° more than that reported for a δ -Nylon 6 [168]. The

Figure 6.11. (a) Rotation photograph of a Nylon 6-I complex drawn 4X and (b) schematic showing details of observed reflections.

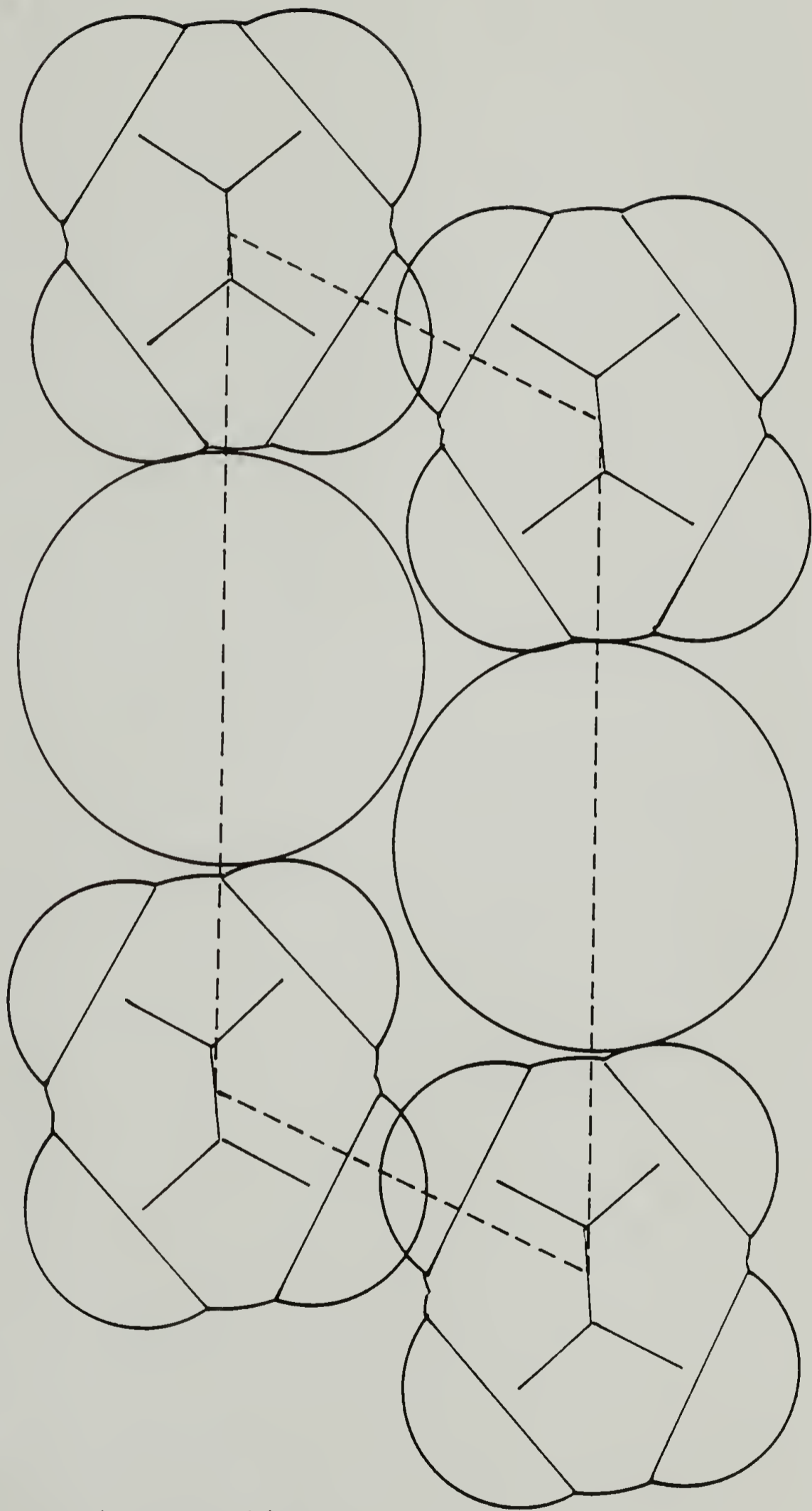
Table 6.5

Comparison of Observed and Calculated d-Spacings
for a Nylon 6-I Complex Drawn 4X

(hkl)	d-Spacing (nm)		Intensity*
	Observed	Calculated	
100	1.556	1.557	m
300	.520	.520	w
001	.773	.773	vs
002	.388	.387	s
003	.258	.258	w
004	.194	.193	vw
110	.743	.735	m
210]	.569	.569	w
011]		.567	
310	.441	.440	w
120	.409	.402	w
021	.366	.366	vw

* vs=very strong, s=strong, m=medium, w=weal
vw=very weak

Figure 6.12. Space filling model of one quarter of the proposed structure for Nylon 6-I complex in the a-c plane, showing iodine intercalated between Nylon 6 chains.



$\frac{1}{2}c$

$\frac{1}{2}a$

observed reflection can be indexed with a monoclinic unit cell with axes $a=1.72$ nm, $b=0.833$ nm, $c=0.852$ nm and $\beta=115^\circ$ (Table 6.5). The a -axis of the original γ -Nylon 6 expands to accommodate the intercalation of iodine or I_3^- ion. Because of complexing between amide groups with iodine or I_3^- , the amide group is twisted out-of-plane, shortening the chain axis and changing the interaxial angle. Fig. 6.12 shows a space filling model of one quarter of the unit cell viewed in the a - c plane. When the setting angle of the Nylon 6 chain is 5° , iodine with van der Waal radius of 0.215 nm can be accommodated easily between the chains.

The undrawn complex shows lateral order with mesomorphic structure. On drawing, the complexed chains are forced to align giving a more clearly defined structure with definite fiber identity period. Iodine, being a heavy atom, is a very strong scatterer and dominates the observed intensities. Higher order reflections are observed indicating a high degree of regularity in the intercalated iodine. Here we do not observe the 0.3 nm periodicity of polyiodide ion as reported for poly(vinyl alcohol)-iodine complex [174] and iodine-doped polyacethylene [184]. The intercalated structure proposed here can be found in many complexes. An example is the detailed structural study of benzamide-iodine complex [185] which has I_3^- ion inserted

between the benzamide dimers. The rigid-rod poly(phenylene terephthalamide) [186] which also has hydrogen bond sheets similar to Nylon 6, forms crystal solvates with sulfuric acid molecules intercalated between the hydrogen bond planes. The present proposed structure, though without in-depth study such as exploiting the possibility of the heavy iodine atom to do Patterson mapping to locate its exact position, does depict the structure developed during strain-induced crystallization of the complex.

6.4.5 Application to Other Nylons

The reversible plasticization technique proposed here can also be potentially applied to other Nylons. Arimoto [187], Matsubara and Magill [169] had extensively studied complex formation of several series of Nylons. They found that crystal transformation occurs only for even-odd, odd-even and some ω -amino acid type of Nylons (Table 6.6). These Nylons thus have potential application of the reversible plasticization drawing technique. Even though crystal transformation may not have occurred for some of the Nylons, as long as iodine or I_3^- are capable of complexing with the amide groups, interrupting hydrogen bond, this technique may then be applicable.

Table 6.6

Crystal-Crystal Transformation of Other Aliphatic
Nylons by Treatment in a KI_3 Solution

	Polyamides*	Before	After
even-even	210, 66, 68, 610, 86, 88 106, 1010	α	α
even-odd	29, 49, 67, 69, 109 65	α δ	γ γ
odd-even	56, 76, 78, 710, 96	α	γ
odd-odd	7, 59, 77, 79, 97, 99	γ	γ
ω -amino acid type	4, 7, 9, 11 10, 12 6, 8	α γ α	α γ γ

* Results compiled from references 169 and 187.

6.5 Conclusions

A new drawing technique for Nylon 6 by reversible plasticization with iodine is proposed. A 130 μ m thick Nylon 6 film was immersed in a 1N aqueous KI_3 solution for 48 hours. TGA and UV-visible spectroscopy studies show that the main complexing species is likely to be I_3^- ion with a stoichiometry of $(Nylon\ 6)(I_3^-)_{0.24}(I_2)_{0.35}$. The complexed film was drawn at temperatures between 23 and 55°C, corresponding to temperatures below and above the α -relaxation temperature as determined from Rheovibron. At 55°C, the complexed film showed rubbery behavior with low yield stress and high elongation at break of 790%, therefore, a much higher draw is possible for Nylon 6. The draw film was washed with sodium thiosulfate solution at room temperature to remove the absorbed iodine, giving a highly oriented γ -Nylon 6 with $f_c > 0.978$. Wide-angle X-ray showed crystallinity of original Nylon 6 was destroyed with the development of new diffraction peaks, an evidence of plasticization of both the amorphous and crystalline phases. The complex showed strain-induced crystallization giving new diffraction peaks corresponding to a monoclinic structure. The a-axis expanded to 1.72 nm, a dimension big enough for iodine or I_3^- to intercalate between the Nylon 6 chains.

FUTURE WORK

The problem on melting and recrystallization during deformation of semi-crystalline polymers remains unsolved. The present study shows that CEPE does not melt during deformation. It can be argued that this morphology has too few entanglements and therefore does not represent the profusely interconnected chain-folded lamellae during deformation. It is suggested here as a future work, that an ultra-high molecular weight PE of $>10^6$, with the $<10^4$ fraction, removed by fractionation, be crystallized into chain-extended lamellae to give an average of 20 to 30 folds per chain, duplicating the fold surfaces of a low molecular weight HDPE, Alathon 7050, lamellae with 20 to 30 nm long period. Comparing their SAXS will give a more definitive conclusion.

Plasticization of Nylon 6 with iodine gives an interesting and relatively unexplored new complex. Iodine itself is antiseptic and is free to migrate out from the complex as observed from its staining property. One possible future study is to explore the practical application of the slowly releasing antiseptic property of

iodine. An example of such a complex being used medically is poly(vinyl pyrrolidone)-I complex, which has a similar functional group to Nylon 6. The new drawing technique also has potential applications to others in the series of aliphatic Nylons, as discussed in Section 6.4.5. An advantage would be to use in the drawing of Nylon 4, which degrades during melt spinning.

More important in this study is that it shows how simple polar compounds can be used to interrupt hydrogen bonds in Nylon crystals, changing its properties to the advantage of processing. This provides a new area of study of drawing through reversible chemical modification of the polymer. Phenol is another potential compound for such study in Nylons [181]. Another interesting modification of both aliphatic and aromatic polyamides is the adducts formed with perfluoro diacids, as reported by Aharoni and Wasserman [188]. Further research into the chemical interactions of polyamides will probably provide new ways of drawing through reversible chemical modifications.

REFERENCES

1. T. Shimanouchi, M. Asahina and S. Enomoto, "Elastic Moduli of Oriented Polymers. I. The Simple Helix, Polyethylene, Polytetrafluoroethylene, and a General Formula", *J. Polym. Sci.*, 59, 93 (1962).
2. T.R. Manley and C.G. Martin, "The Elastic Modulus of Nylons", *Polymer*, 14, 632 (1973).
3. T. Kanamoto, A. Tsurata, K. Tanaka, M. Takeda and R.S. Porter, "On Ultra-High Tensile Modulus by Drawing Single Crystal Mats of High Molecular Weight Polyethylene", *Polym. J.*, 15, 327 (1983).
4. A.J. Pennings, J.M.A.A. van Der Mark and H.C. Booij, "Hydrodynamically Induced Crystallization of Polymers from Solution. II. The Effect of Secondary Flow", *Coll. Polym. Sci.*, 236, 99 (1970).
5. D.C. Prevorsek, Private Communication.
Chemical and Engineering News, Feb. 25, 1985, p.7.
6. D. Acierno, F.P. La Mantia, G. Polizzotti, C.G. Alfonso and A. Ciferri, "Increasing the Elastic Modulus of Polyamide", *J. Polym. Sci., Polym. Lett. Ed.*, 15, 323 (1977).
7. S. Gogolewski and A.J. Pennings, "Crystallization of Polyamides Under Elevated Pressure: 4. Annealing of Nylon 6 (Polycapramide) Under Pressure", *Polymer*, 18, 654 (1977).
8. R.A.C. Slater, Engineering Plasticity: Theory and Application to Metal Forming Processes, Halsted Press, 1977.
9. J.H. Southern and R.S. Porter, "The Properties of Polyethylene Crystallized Under the Orientation and Pressure Effects of a Pressure Capillary Viscometer", *J. Appl. Polym. Sci.*, 14, 2305 (1970).
10. A.E. Zachariades, W.T. Mead and R.S. Porter, "Recent Advances in Ultraorientation of Polyethylene by Solid State Extrusion", *Chem. Rev.* 80, 351 (1980).
11. P.I. Vincent "The Necking and Cold-Drawing of Rigid Plastics", *Polymer*, 1, 7 (1960).

12. A.G. Gibson, I.M. Ward, B.N. Cole and B. Parsons, "Hydrostatic Extrusion of Linear Polyethylene", *J. Mater. Sci.*, 9, 1193 (1974).
13. K. Imada and M. Takayanagi, "Plastic Deformation of High Density Polyethylene in Solid State Extrusion", *Intern. J. Polymeric Mater.*, 2, 89 (1973).
14. K. Nakayama and H. Kanetsuna, "Critical Extrusion Pressure and Rate of Extrusion in Hydrostatic Extrusion of Solid Polyethylene", *Kobunshi Ronbunshu*, 31, 256 (1974).
15. A.E. Zachariades, P.D. Griswold and R.S. Porter, "Solid State Coextrusion: A New Technique for Ultradrawing Thermoplastics Illustrated with High Density Polyethylene", *Polym. Eng. Sci.*, 18, 861 (1978).
16. T. Kunugi, A. Suzuki and M. Hashimoto, "Preparation of High-Modulus and High-Strength Poly(ethylene terephthalate) Fiber by Zone Annealing", *J. Appl. Polym. Sci.*, 26, (1981).
17. T. Kanamoto, S. Fujimatsu, M. Ito, K. Tanaka and R.S. Porter, "Morphological Changes During Solid-State Extrusion of Polyethylene Single Crystal", *Proc. IUPAC 28th Macromol. Symp.*, Amherst, July 1982.
18. A.J. Pennings, C.J.H. Schouteten and A.M. Kiel, "Hydrodynamically Induced Crystallization of Polymers from Solution. V. Tensile Properties of Fibrillar Polyethylene Crystals", *J. Polym. Sci.*, C38, 167 (1972).
19. P. Smith and P.J. Lemstra, "Ultra-drawing of High Molecular Weight Polyethylene Cast from Solution", *Coll. Polym. Sci.*, 258, 891, (1980).
20. P.J. Barham "Gelation and the Production of Stiff Polyethylene Fibers", *Polymer*, 23, 1112 (1982).
21. G. Cannon, "Orientation Process in the Drawing of Dry Gel Films of Polyethylene and Propylene", *Polymer*, 23, 1123 (1982).
22. M.R. Mackley and A. Keller, "Flow Induced Crystallization of Polyethylene Melts", *Polymer*, 14, 16 (1973).
23. P.D. Griswold and J.A. Cuculo, "Flow-Induced Crystallization of Poly(ethylene terephthalate) Melts

- in a Capillary Die: Formation and Properties of the Crystalline Toroid", *J. Polym. Sci.*, 15, 1291 (1977).
24. R.S. Porter, Private Communication.
 25. A.G. Gibson, G.R. Davies and I.M. Ward, "Dynamic Mechanical Behaviors and Longitudinal Crystal Thickness Measurements on Ultra-High Modulus Linear Polyethylene: A Quantitative Model for the Elastic Modulus", *Polymer*, 19, 683 (1978).
 26. A. Peterlin, "Molecular Model of Drawing Polyethylene and Polypropylene", *J. Mater. Sci.*, 6, 490 (1971).
 27. G.E. Attenburrow and D.C. Bassett, "On the Plastic Deformation of Chain-Extended Polyethylene" *J. Mater. Sci.*, 12, 192 (1977).
 28. B. Appelt and R.S. Porter, "The Multistage Ultradrawing of Atactic Polystyrene by Solid-State Coextrusion", *J. Macromol. Sci.*, B20, 21 (1981).
 29. A.E. Zachariades, M.P.C. Watts, T. Kanamoto and R.S. Porter, "Solid-State Extrusion of Polymer Powders Illustrated with Ultrahigh Molecular Weight Polyethylene", *J. Polym. Sci., Polym. Lett. Ed.*, 17, 485 (1979).
 30. F.A. Bovey and F.H. Winslow, editors, Macromolecules An Introduction to Polymer Science, Academic Press, New York, 1979.
 31. F.W. Billmeyer Jr., Textbook of Polymer Science, 2nd ed., Wiley, 1971.
 32. C.W. Bunn, A.J. Cobbold and R.P. Palmer, "The Fine Structure of Polytetrafluoroethylene", *J. Polym. Sci.*, 28, 365 (1958).
 33. B. Fitton and C.H. Griffiths, "Morphology of Spherulites and Single Crystals of Trigonal Selenium", *J. Appl. Phys.*, 39, 3663 (1968).
 34. L. Mandelkern, J.M. Price, M. Gopalan and J.G. Fatou, "Sizes and Interfacial Free Energies of Crystallites Formed from Fractionated Linear Polyethylene", *J. Polym. Sci., Polym. Phys. Ed.*, 4, 385 (1966).
 35. B. Wunderlich and T. Arakawa, "Polyethylene Crystallized from Melt Under Elevated Pressure", *J. Polym. Sci.*, Pt.A 2, 3697 (1964).

36. P.H. Geil, F.R. Anderson, B. Wunderlich and T. Arakawa, "Morphology of Polyethylene from the Melt Under Pressure", *J. Polym. Sci., Pt.A 2*, 3707 (1964).
37. Y. Miyamoto, C. Nakafuku and T. Takemura, "Crystallization of Polychlorotrifluoroethylene", *Polym. J.*, 3, 120 (1972).
38. S. Gogolewski and A.J. Pennings, "Crystallization of Polyamide Under Elevated Pressure: 2. Pressure-Induced Crystallization of Nylon 6 (Polycapramide) from the Melt", *Polymer*, 16, 673 (1975).
39. D.C. Bassett, Principles of Polymer Morphology, Cambridge University Press, 1981.
40. N. Toyota and S. Machi, "Morphology of Polyethylene Crystal as Polymerized by γ -radiation", *J. Polym. Sci., Polym. Phys. Ed.*, 7, 153 (1963).
41. A.J. Pennings and A.M. Kiel, "Fractionation of Polymers by Crystallization from Solution. III. On the Morphology of Fibrillar Polyethylene Crystals Grown in Solution", *Kolloid Z.Z.*, 205, 160
42. B. Wunderlich, Macromolecular Physics, Volume 1, Crystal Structure, Morphology, Defects, Academic Press, 1973.
43. D.C. Bassett, editor, Developments in Crystalline Polymers I, Applied Science Pub., 1983.
44. Y. Maeda and H. Kanetsuna, "Crystallization and Melting of Polyethylene Under High Pressure. II. Effect of Pressure on Melting Behavior of Various Types of Crystals", *J. Polym. Sci., Polym. Phys. Ed.*, 13, 637 (1975).
45. M. Yasuniwa and T. Takemura, "Microscopic Observations of the Crystallization Process of Polyethylene Under High Pressure", *Polymer*, 15, 661 (1974).
46. D.C. Bassett, "Chain-Extended Polyethylene in Context: a Review", *Polymer*, 17, 460 (1976).
47. B. Wunderlich and T. Davidson, "Extended-Chain Crystals. I. General Crystallization Conditions and Review of Pressure Crystallization of Polyethylene", *J. Polym. Sci., Polym. Phys. Ed.*, 7, 2043 (1969).
48. Y. Maeda and H. Kanetsuna, "Crystallization and Melting of Polyethylene Under High Pressure. I.

- Crystallization by Slow Cooling from the Melt",
J. Polym. Sci., Polym. Phys. Ed., 12, 2551 (1974).
49. D.C. Bassetts and B. Turner, "New High-Pressure Phase in Chain-Extended Crystallization of Polythene", Nature (Phys. Sci.), 240, 146 (1972).
 50. M. Yasuniwa, C. Nakafuku and T. Takemura, "Melting and Crystallization Process of Polyethylene Under High Pressure", Polym. J., 4, 526 (1973).
 51. Y. Maeda, H. Kanetsuna, K. Tagashira and T. Takemura, "DTA and X-Ray Studies of Extended-Chain Crystals of Polyethylene Under High Pressure", J. Polym. Sci., Polym. Phys. Ed., 19, 1325 (1981).
 52. D.C. Bassetts and D. Turner, "On Chain-Extended and Chain-Folded Crystallization of Polyethylene", Phi. Mag., 29, 285 (1974).
 53. D.C. Bassetts, S. Block and G.J. Piermarini, "A High-Pressure Phase of Polyethylene and Chain-Extended Growth", J. Appl. Phys., 45, 4146 (1974).
 54. D.V. Rees and D.C. Bassett, "Crystallization of Polyethylene at Elevated Pressure", J. Polym. Sci., Polym. Phys. Ed., 9, 385 (1971).
 55. B. Wunderlich and L. Melillo, "Morphology and Growth of Extended Chain Crystals of Polyethylene", Makromol. Chem., 118, 250 (1968).
 56. H.H. Hoehn, R.C. Ferguson and R.R. Hebert, "Effect of Molecular Weight of High Pressure Crystallization of Linear Polyethylene. I. Kinetics and Gross Morphology", Polym. Eng. Sci., 18, 250 (1978).
 57. W.T. Mead and R.S. Porter "The Influence of Initial Morphology on the Physical and Mechanical Properties of Extruded High Density Polyethylene Fibers", Intern. J. Polymeric Mater., 7, 29 (1979).
 58. J.M. Lupton and J.W. Register, "Physical Properties of Extended-Chain High Density Polyethylene", J. Appl. Polym. Sci., 18, 2407 (1974).
 59. N. Capiati, S. Kojima, W. Perkins and R.S. Porter, "Preparation of an Ultra-Oriented Polyethylene Morphology", J. Mater. Sci., 12, 334 (1977).
 60. R.G.C. Arridge and M.J. Folkes, "Effect of Sample Geometry on the Measurement of Mechanical Properties

- of Anisotropic Materials", *Polymer*, 17, 495 (1976).
61. M.P.C. Watts, A.E. Zachariades and R.S. Porter, "Shrinkage as a Measure of the Deformation Efficiency of Ultra-Oriented High Density Polyethylene", *J. Mater. Sci.*, 15, 426 (1980).
 62. M. Daniels, M.P.C. Watts, J.R.C. Pereira, S.J. DeTeresa and A.E. Zachariades and R.S. Porter, "Shrinkage as a Measure of the Deformation Efficiency of Ultra-Oriented High Density Polyethylene: Authors' Addition", *J. Mater. Sci.*, 16, 1134 (1981).
 63. M.M. Daniels, The Effect of Processing Conditions on the Solid-State Deformation and Consequent Properties of High Density Polyethylene, M.S. Thesis, University of Massachusetts, 1982.
 64. G.L. Wilke and R.S. Stein, in Structure and Properties of Oriented Polymers, I.M. Ward, editor, Wiley, 1975.
 65. Z.W. Wilchinsky, "Determination of Orientation of the Crystalline and Amorphous Phases in Polyethylene by X-Ray Diffraction", *J. Polym. Sci., Polym. Phys. Ed.*, 6, 281 (1968).
 66. C.R. Desper, J.H. Southern, R.D. Ulrich and R.S. Porter, "Orientation and Structure of Polyethylene Crystallized Under the Orientation and Pressure Effects of a Pressure Capillary Viscometer", *J. Appl. Phys.*, 41, 4284 (1970).
 67. L.E. Alexander, X-Ray Diffraction Methods in Polymer Science, Krieger, 1979.
 68. R. Hosemann and S.N. Bagchi, Direct Analysis of Diffraction by Matter, North Holland, Amsterdam, 1962.
 69. B.E. Warren, X-Ray Diffraction, Addison-Wesley, 1969.
 70. A.R. Stokes, "A Numerical Fourier-Analysis Method for the Correction of Widths and Shapes of Lines on X-Ray Powder Photographs", *Proc. Phys. Soc. (London)*, A61, 382 (1948).
 71. P.H. Geil, Polymer Single Crystals, Interscience Pub., New York, 1963.
 72. J. Minter, Structural Investigations of Fibers and Films of Poly(p-phenylene benzobisthiazole), Ph. D. Dissertation, University of Massachusetts, 1982.

73. E.L. Thomas, Private Communication.
74. R.B. Prime and B. Wunderlich, "Extended-Chain Crystals. III. Size Distribution fo Polyethylene Crystals Grown Under Elevated Pressure", J. Polym. Sci., Polym. Phys. Ed., 7, 2061 (1969).
75. D.C. Bassetts, B.A. Khalifa and R.H. Olley, "Morphological Study of Chain-Extended Growth in Polyethylene: 2. Annealed Bulk Polymer", Polymer, 17, 284 (1976).
76. Y. Maeda and H. Kanetsuna, "Crystallite Size Analysis of Pressure-Crystallized Polyethylene by Nitri Acid Etching and Gel-Permeation Chromatography. I. Extended Chain Crystals", Polym. J., 13, 357 (1981).
77. D.C. Bassetts, B.A. Khalifa and R.H. Olley, "Measurement of High Chain Extension in Polyethylene by Gel Permeation Chromatography", J. Polym. Sci., Polym. Phys. Ed., 15, 995 (1977).
78. R.C. Ferguson and H.H. Hoehn, "Effect of Molecular Weight on High Pressure Crystallization of Linear Polyethylene. II. Physical and Chemical Characterization of Crystallinity and Morphology", Polym. Eng. Sci., 18, 466 (1978).
79. K.H. Illers, "Untersuchugen zum Schmelzverhalten von verstrecktern Polyäthylen", Angew. Makromol. Chem., 12, 89 (1970).
80. T. Kanamoto, S. Fujimatsu, A. Tsurata, K. Tanaka and R.S. Porter, "X-Ray Diffraction Study of Solid-State Extrusion of Melt-Crystallized High Density Polyethylene", Rep. Prog. Polym. Phys. Jpn., 24, 185 (1981).
81. G. Hadziioannou, L.H. Wang, R.S. Stein and R.S. Porter, "Small Angle Neutron Scattering Studies on Amorphous Polystyrene Oriented by Solid-State Coextrusion", Macromolecules, 15, 880 (1982).
82. P. Smith and P.J. Lemstra, "Ultra-High-Strength Polyethylene Filaments by Solution Spinning/Drawing", J. Mater. Sci., 15, 505 (1980).
83. J. de Boer and A.J. Pennings, "Crosslinking of Ultra-High Strength Polyethylene Fibers by Means of γ -Radiation. 2. Entanglements in Ultra-High Strength Polyethylene Fibers", Polym. Bull., 7, 309 (1982).

84. L. Fischer, Ph. D. Thesis, University of Marburg, 1982.
- L. Fischer and W. Ruland, "The Effect of Pressure Crystallization on Structure and Properties of Hot-Drawn Polyethylene", *Colloid. Polym. Sci.*, 261, 717 (1983).
85. R.J. Samuel, Structured Polymer Properties, Wiley, 1974.
86. G. Capaccio and I.M. Ward, "Effect of Molecular Weight on the Morphology and Drawing Behavior of Melt Crystallized Linear Polyethylene", *Polymer*, 16, 239 (1975).
87. S. Kojima and R.S. Porter, "Influence of Extrusion Ratio on the Tensile Properties of Ultradrawn Polyethylene", *J. Polym. Sci., Polym. Phys. Ed.*, 16, 1729 (1978).
88. P.D. Griswold, R.S. Porter, C.R. Desper and R.J. Farris, "Preparation of Ultradrawn Polyethylene by a Novel Radial-Compression Method", *Polym. Eng. Sci.*, 18, 537 (1978).
89. D.T. Grubb, "A Structural Model for High-Modulus Polyethylene Derived from Entanglement Concept", *J. Polym. Sci., Polym. Phys. Ed.*, 21, 165 (1983).
90. L. Fischer, R. Haschberger, A. Ziegeldorf and W. Ruland, 27th Int. Symp. on Macromol., Strasbourg, 1981.
91. P.R. Bevington, Data Reduction and Error Analysis for the Physical Sciences, McGraw-Hill, Inc. 1969.
92. A. Schonfeld and W. Wilke, "Determination of Crystallite Size and Lattice Distortions in Extended Chain Polyethylene and Their Change after Oxidative Degradation", *Kolloid Z.Z. Polymere*, 250, 496 (1972).
93. W. Wilke and K.W. Martis, "Crystallite Size and Lattice Distortions in Stretched Polyethylene", *Colloid Polym. Sci.*, 252, 718 (1974).
94. A. Peterlin, "Plastic Deformation of Crystalline Polymers", *J. Mater. Sci.*, 6, 490 (1971).
95. P.M. Tarin and E.L. Thomas, "An Electron Microscopy Study of the Microfibrillar structure of Deformed Polyethylene Spherulites", *Polym. Eng. Sci.*, 18, 472

- (1978).
96. I.G. Voight-Martin and L. Mandelkern, "A Quantitative Electron-Microscope Study of a Linear Polyethylene Fraction Crystallized at Different Temperatures", *J. Polym. Sci., Polym. Phys. Ed.*, 19, 1769 (1981).
 97. A. Peterlin and G. Meinel, "Small-Angle X-Ray Diffraction Studies of Plastically Deformed Polyethylene. III. Small Draw Ratio", *Makromol. Chem.*, 142, 227 (1971).
 98. R.A. Duckett, in Plastic Deformation of Amorphous and Semi-Crystalline Meaterial, B. Escaig and C. G'Sell, editors, Les Ullis, 1982.
 99. T. Juska and I.R. Harrison, "A Proposed Plastic Deformation Mechanism for Semi-Crystalline Polymers", *Polym. Engr. Rev.*, 2, 13 (1982).
 100. A. Peterlin, "Annealing of Drawn Crystalline Polymers", *Polym. Eng. Sci.*, 18, 488 (1978).
 101. R. Corneliussen and A. Peterlin, "The Influence of Temperature on the Plastic Deformation of Polyethylene", *Makromol. Chem.*, 105, 193 (1967).
 102. B. Wunderlich, Macromolecular Physics Volume 2, Crystal Nucleation, Growth, Annealing, Academic Press, 1976.
 103. T.J. Bessel and R.J. Young, "The Long Period of Compression-Oriented HDPE", *J. Polym. Sci., Polym. Lett. Ed.*, 12, 629 (1974).
 104. P.J. Flory and D.Y. Yoon, "Molecular Morphology in Semicrystalline Polymers", *Nature*, 272, 226 (1978).
 105. G. Meinel and A. Peterlin, "Plastic Deformation of Polyethylene II. Change of Mechanical Properties During Drawing", *J. Polym. Sci., Polym. Phys. Ed.*, 9, 67 (1971).
 106. G.D. Wignall and W. Wu, "A SANS Investigation into the Role of Melting and Recrystallization During Solid State Deformation of Polyethylene", *Polymer Comm.*, 24, 354 (1983).
 107. W. Wu, H.G. Zachmann and C. Rickel, "The Role of Melting-Recrystallization Mechanism in Deformation of Crystalline Polymers", *Polymer Comm.*, 25, 76 (1984).

108. W. Adams, E.L. Thomas and J.S. Lin, "SAXS Invariant Analysis of Solid State Extruded Polyethylene", ACS Polymer Preprints, 24, No.2, 372 (1983).
109. W.W. Adams, R.M. Briber, E.S. Sherman, R.S. Porter and E.L. Thomas, "Microstructure of High Modulus Solid State Extruded Polyethylene: 2. X-Ray Scattering Studies of 12, 24 and 36 Extrusion Draw Ratio", Polymer, 26, 17 (1985).
110. D.S. Trifan and J.F. Terenzi, "Extents of Hydrogen Bonding in Polyamides and Polyurethanes", J. Polym. Sci., 28, 443 (1958).
111. D.R. Holms, C.W. Bunn and D.j. Smith, "The Crystal Structure of Polycapromamide: Nylon 6", J. Polym. Sci., 17, 159 (1955).
112. R. Brill, Z. Physik Chem., B53, 61 (1943).
113. E. Kordes, F. Gunther, L. Buchs and W. Goltner, "Optische und Röntgenographische Untersuchungen an der vollsynthetischen Perlon-Faser", Kolloid Z.Z., 119, 23 (1950).
114. L.G. Wallner, "Über den Einfluß der Kristallitlänge auf die Röntgen-Interferenzen der Polyamide", Monatsh. Chem., 79, 279 (1948).
115. A. Ziabicki, "Über die Mesomorphe β -Form von Polycapronamid und ihre Umwandlung in die Kristalline Form α ", Kolloid Z.Z. Polymere, 167, 132 (1959).
116. N. Avramova and S. Fakirov, "The β -structure of Nylon-6 Determined by Reflection High Energy Electron Diffraction", Polymer Comm., 25, 27 (1948).
117. A. Reichle and A. Prietzch, "Spinnpuze β und Kristallstrukturen von Perlon-Fäden", Angew. Chem., 74, 562 (1962).
118. G. Roldan and H.S. Kaufman, "Crystallization of Nylon 6", J. Polym. Sci., Polym. Lett. Ed., 1, 603 (1963).
119. H.K. Iller, H. Haberkorn and P. Simak, "Untersuchungen über die γ -Struktur von unverstreckten und verstreckten 6-Polyamid", Makromol. Chem., 158, 285 (1972).
120. R.F. Stepaniak, A. Garton, D.J. Carlson and D.M. Wiles, "An Examination of the Crystal Structures Present in Nylon-6 Fibers", J. Polym. Sci.,

- Polym. Phys. Ed., 17, 987 (1979).
121. Y. Kinoshita, "An Investigation of the Structures of Polyamide Series", Makromol. Chem., 33, 1 (1959).
 122. S. Ueda and T. Kimura, "Studies on the Sorption of Iodine by Polyamide Fibers. I. On the Sorption of Iodine by Nylon-6 Fiber", Kobunshi Kagaku, 15, 243 (1958).
 123. K. Miyasaka and K. Makishima, "Transition of Nylon 6 γ -Phase Crystals by Stretching in the Chain Direction", J. Polym. Sci., Pt.A-1, 5, 3017 (1967).
 124. D.C. Vogelsong, "Crystal Structure Studies on the Polymorphic Forms of Nylon 6 and 8 and Other Even Nylons", J. Polym. Sci., Pt.A, 1, 1055 (1963).
 125. H. Arimoto, M. Ishihashi and M. Hirai, "Crystal Structure of the γ -form of Nylon 6", J. Polym. Sci., Pt.A, 3, 317 (1965).
 126. T. Ota, O. Yoshizaki and E. Nagai, "Studies on the Crystal Modification of Nylon 6. I. The X-Ray Investigation of the Nylon 6 Film Made from the Formic Acid Aqueous Solution", Kobunshi Kagaku, 20, 225 (1963).
 127. E.M. Bradbury and A. Elliot, "Infra-red Spectra and Chain Arrangement in some Polyamids, Polypeptides and Fibrous Proteins", Polymer, 4, 47 (1963).
- E.M. Bradbury, L. Brown, A. Elliot and D.A.D. Parry, "The Structure of the Gamma Form of Polycaproamide (Nylon 6)", Polymer, 6, 465 (1965).
129. J.P. Parker and P.H. Lindenmeyer, "On the Crystal Structure of Nylon 6", J. Appl. Polym. Sci., 21, 821 (1977).
 130. A.J. Pennings and K.E. Meihuizen, in A. Ciferri and I.M. Ward, editors, Ultra-High Modulus Polymers, Applied Science Pub., 1979.
 131. P. Smith, P.J. Lemstra and H.C. Booij, "Ultradrawing of High-Molecular-Weight Polyethylene Cast from Solution. II. Influence of Initial Polymer Concentration", J. Polym. Sci., Polym. Phys. Ed., 19, 877 (1981).
 132. M.R. Mackley and G.S. Sapsford, in Developments in Oriented Polymers-I, I.M. Ward, editor, Applied

Science, 1982

133. P. Smith and P.J. Lemstra, "Tensile Strength of Highly Oriented Polyethylene", *J. Polym. Sci., Polym. Phys. Ed.*, 19, 1007 (1981).
134. M. Matsuo and R. St. John Manley, "Ultradrawing at Room Temperature of High Molecular Weight Polyethylene", *Macromolecules*, 15, 985 (1982).
135. C.G. Cannon, "Orientation Process in the Drawing of Dry Gel Films of Polyethylene and Polypropylene", *Polymer*, 23, 1123 (1982).
136. A. Peguy and R. St. John Manley, "Ultra-Drawing of High Molecular Weight Polypropylene", *Polymer Comm.*, 25, 39 (1984).
137. D.T. Grubb, 4th Cleveland Macromolecule Symposium, June 1983.
138. D.J. Loyd, in Colloid Chemistry, Vol. I, J. Alexander, editor, New York, 1926.
139. R.J. Hartman, Colloid Chemistry, Houghton Mifflin Co., 1947.
140. A. Tager, Physical Chemistry of Polymers, MIR Publications, 1978.
141. A. Keller, Structure-Property Relationships of Polymeric Solids, A. Hiltner, editor, Plenum Press, 1983.
142. A. Rinke and E. Istel, Methoden der Organische Chemie, 4e Aufl. (Houben-Weyl), Band XIV/2, Geor. Thieme Verlag, Stuttgart, 1963.
143. J.E. Stamhuis and A.J. Pennings, "Gelation and Crystallization of Nylon-6 from Dilute Solution", *British Polym. J.*, 10, 221 (1978).
144. R.S. Stein, "Measurement of Birefringence of Biaxially Oriented Films", *J. Polym. Sci.*, 24, 383 (1957).
145. C.R. Desper, A Study of Crystallization and Orientation Mechanisms in Polyethylene, Ph.D. Dissertation, University of Massachusetts, 1966.
146. B.F. Decker, E.T. Asp and D. Harker, "Preferred Orientation Determination Using a Geiger Counter

- X-Ray Diffraction Goniometer", J. Appl. Phys., 19, 388 (1948).
147. L.G. Schulz, "A Direct Method of Determining Preferred Orientation of a Flat Reflection Sample Using a Geiger Counter X-Ray Spectrometer", J. Appl. Phys., 20, 1030 (1949).
 148. Y.C. Yang and P.H. Geil, "Morphology and Properties of PVC/Solvent Gels", J. Macromol. Sci., B22, 463 (1983).
 149. S.J. Guerrero, A. Keller, P.L. Soni and P.H. Geil, "Study of Crystal Texture of PVC Gels by X-Ray Diffraction and Infra-red Dichroism", J. Polym. Sci., Polym. Phys. Ed., 18, 1533 (1980).
 150. T. Shimada and R.S. Porter, "Crystalline State Extrusion of Melt-Crystallized and Solution-Grown Crystals of Nylon 6 and 6,6", Polymer, 22, 1124 (1981).
 151. M. Kyotani, "Stirring-Induced Crystallization of Nylon 6", J. Macromol. Sci., B21, 275 (1981).
 152. M. Tadoki and T. Kawaguchi, "Melting of Constrained Drawn Nylon 6 Yarns", J. Polym. Sci., Polym. Phys. Ed., 15, 1507 (1977).
 153. J.R.C. Pereira and R.S. Porter, "Solid-State Coextrusion of Poly(ethylene Terephthalate). II. Drawing of Semicrystalline PET.", J. Polym. Sci., Polym. Phys. Ed., 21, 1147 (1983).
 154. F. Fujimoto, T. Shiroguchi, H. Kishida and I. Akeyama, "Drawing Behavior of Nylon 6 Filaments - Drawing Conditions and Tensile Properties of Drawn Filaments", Nippon Sen'i Kikai Gakkai, 19, 1 (1973).
 155. H. Berghman, F. Govaerts and N. Overbergh, "Gelation and Crystallization of Poly(ethylene terephthalate-co-Isophthalate)", J. Polym. Sci., Polym. Phys. Ed., 18, 1533 (1980).
 156. E.D.T. Atkins, "Structure Studies on Gels from Isotactic Polystyrene", Colloid Polym. Sci., 262, 22 (1984).
 157. R. Bonart and K. Hoffmann, "Orientierungsverhalten von segmentierten Polyurethanen in Abhängigkeit von der Folienpräparation und dem Zeitpunkt der Orientierungsbestimmung", Colloid Polym. Sci., 260,

- 268 (1982).
158. A.E. Zachariades and R.S. Porter, "Deformation of Plasticized Nylon 6 with Ammonia by Solid-State Extrusion", *J. Polym. Sci., Polym. Lett. Ed.*, 17, 277 (1979).
159. M.I. Kohan, editor, Nylon Plastics, J. Wiley, New York 1973.
160. A.E. Zachariades and R.S. Porter, "Deformation of Plasticized Nylon 6 with Ammonia by Solid-State Extrusion", *J. Polym. Sci., Polym. Lett. Ed.*, 17, 277 (1979).
161. T. Kanamoto, A.E. Zachariades and R.S. Porter, "The Effect of Anhydrous Ammonia on the Crystalline-State Deformation of Nylon 6 and 6,6", *J. Polym. Sci., Polym. Phys. Ed.*, 20, 1485 (1982).
162. W. Wu and W.B. Black, "Stretching of Nylon 66 Yarn Saturated with Dry HCl", *ACS Polymer Preprints*, 22, 248 (1981).
163. A. Siegmann and Z. Baraam, "Nylon 6 Containing Metal Halids I: Melting and Crystallization", *Intern. J. Polymeric Mater.*, 8, 243 (1980).
164. B. Valenti, E. Bianchi, A. Tealdi, S. Russo and A. Ciferri, "Bulk Properties of Synthetic Polymer-Inorganic Salt Systems. IV. Role of the Polymeric Substrate", *Macromolecules*, 9, 117 (1976).
165. D. Acierno, S. Castrovicizenna and F.P. LaMantia, "Optimization of Spinning, Drawing, and Annealing Conditions in the Production of Highly Oriented Fibers from the Polycaprolactam/3.7% LiCl System", *J. Polym. Sci., Polym. Phys. Ed.*, 27, 1335 (1982).
166. M. Tsuruta, H. Arimoto and M. Ishibashi, "The Appearance of the New Crystal Structure in Nylon 6", *Kobunshi Kagaku*, 15, 619 (1958).
167. P.D. Frayer, J.L. Koenig and J.B. Lando, "Infrared Studies of Chain Folding in Polymers. X. Polycaprolactam", *J. Macromol. Sci., Phys.*, B6, 129 (1972).
168. H. Arimoto, " $\alpha \rightarrow \gamma$ Transition of Nylon 6", *J. Polym. Sci., Pt. A*, 2, 2283 (1964).
169. J. Matsubara and J.H. Magill, "An Infra-red Study of

- the Interaction of Polyamides with Iodine-Potassium Iodide Solution", *Polymer*, 7, 199 (1966).
170. D. Doskocilova and B. Schneider, "On the Structure and Properties of Polyamides. III. Infrared Spectra of Complexes of N-Alkylamides with KJ_3 ", *Coll. Czech. Chem. Commun. (English Ed.)*, 27, 2605 (1962).
171. I. Abu-Isa, " α - γ Transition in Nylon 6", *J. Polym. Sci., A-1*, 9, 199 (1971).
172. H. Arimoto, "Iodine Treatment of Nylon 6", *Kobunshi Kagaku*, 19, 101 (1962).
173. M.C. Sneed, J.L. Maynard and R.C. Brasted, *Comprehensive Inorganic Chemistry, Vol. 3, The Halogens*, Van Nostrand, 1954.
174. C.D. West, "Structure-Optical Studies, I. X-Ray Diffraction by Addition Compounds of Halogens with Hydrophilic Organic Polymers", *J. Chem. Phys.*, 15, 689 (1947).
175. R. Rundle J. Forster and R. Baldwin, "On the Nature of Starch-Iodine Complex", *J. Am. Chem. Soc.*, 66, 2116 (1944).
176. R.F. Cournoyer, *Chemical and Microscopic Investigation of the Polyvinylpyrrolidone- Iodine Interaction*, Ph. D. Dissertation, University of Massachusetts, 1974.
177. T.C. Clarke and G.B. Street, "The Chemical Nature of Polyacethylene Doping", *Synthetic Metals*, 1, 119 (1979).
178. R.S. Stein and R.E. Rundle, "On the Nature of the Interaction between Starch and Iodine", *J. Chem. Phys.*, 16, 195 (1948).
179. L.I. Katzin, "Regularities in the Absorption Spectra of Halides", *J. Chem. Phys.*, 23, 2055 (1955).
180. S.L. Hsu, A.J. Signorelli, G.P. Pez and R.H. Baughman, "Highly Conducting Iodine Derivatives of Polyacetylene: Raman, XPS and X-Ray Diffraction Studies", *J. Chem. Phys.*, 69, 106 (1979).
181. K. Hoashi and R.D. Andrew, "Morphological Changes in Nylon 6 and Effect of Mechanical Properties. II. Dynamic Mechanical Properties", *J. Polym. Sci.*, C38,

- 387 (1972).
182. T. Kunugi, "Stress Relaxation of Oriented Nylon 6 Fibers", *J. Appl. Polym. Sci.*, 24, 923 (1979).
 183. L. Pauling, The Nature of the Chemical Bond, 3rd ed., Cornell University, 1966.
 184. T. Danno, K. Miyasaka and K. Ishikawa, "Dynamic and Mechanism of Iodine Sorption by Polyacetylene", *J. Polym. Sci., Polym. Phys. Ed.*, 21, 1527 (1982).
 185. J.M. Reddy, K. Knox and M.B. Robin, "Crystal Structure of $HI_{3.2}C_6H_5CONH_2$: A Model of the Starch-Iodine Complex", *J. Chem. Phys.*, 40, 1082 (1964).
 186. K.H. Gardner, "The Structure of Two Aramid/Sulfuric Acid Solvates", *ACS Proc. Polym. Mater. Sci. Engr.*, 51, 192 (1984).
 187. H. Arimoto, "Iodine Treatment of Polyamides", *Kobunshi Kagaku*, 19, 461 (1962).
 188. S.M. Aharoni and E. Wasserman, "Adducts of Polyamides in Perfluoric Diacids", *Macromolecules*, 15, 20 (1982).
 189. T. Kunugi, T. Ikuta, M. Hashimoto and K. Matsuzaki, "Preparation of Ultra-High Strength Nylon 6 Fiber by Multi-Step Zone-Annealing Method", *Polymer*, 23, 1983 (1982).
 190. J.E. Stamhuis, S.D. Sjoerdsma and A.J. Pennings, "Crystallization of Polyamides Under Elevated Pressure. 7. Effect of Reequilibration on the Annealing of Nylon 6 Under Elevated Pressure", *J. Macromol. Sci.*, B22, 383 (1983).

